Combining Models of Coronal Mass Ejections and Solar Dynamos

Jörn Warnecke

Cover image: Convectively driven dynamo in a spherical shell with realistic differential rotation shedding a coronal ejection of current helicity. The radial velocities at the surface and at the bottom of the convection zone are shown in shades of red on two spherical shells. The meridional cut shows the mean differential rotation profile and the colored ejection on the right contains the two polarities of the current helicity density. This illustration is a composite of two simulations of spherical wedges with coronal envelopes, one with self-consistent convection and the other, with forced turbulence. These simulations has been developed and performed in this thesis. The background image of the Sun was observed by AIA 171 on SDO on the 18th of April 2013.

ISBN 978-91-7447-675-0

Printed in Sweden by Universitetsservice, US-AB, Stockholm 2013
Distributor: Department of Astronomy, Stockholm University

Abstract

Observations show that Coronal Mass Ejections (CMEs) are associated with twisted magnetic flux configurations. Conventionally, CMEs are modeled by shearing and twisting the footpoints of a certain distribution of magnetic flux at the solar surface and letting it evolve at the surface. Of course, the surface velocities and magnetic field patterns should ultimately be obtained from realistic simulations of the solar convection zone where the field is generated by dynamo action. Therefore, a unified treatment of the convection zone and the CMEs is needed. Numerical simulations of turbulent dynamos show that the amplification of magnetic fields can be catastrophically quenched at magnetic Reynolds numbers typical of the interior of the Sun. A strong flux of magnetic helicity leaving the dynamo domain can alleviate this quenching. In this sense, a realistic (magnetic) boundary condition is an important ingredient of a successful solar dynamo model.

Using a two-layer model developed in this thesis, we combine a dynamo-active region with a magnetically inert but highly conducting upper layer which models the solar corona. In four steps we improve this setup from a forced turbulent to a convectively driven dynamo and from an isothermal to a polytropic stratified corona. The simulations show magnetic fields that emerge at the surface of the dynamo region and are ejected into the coronal part of the domain. Their morphological form allows us to associate these events with CMEs. Magnetic helicity is found to change sign in the corona to become consistent with recent helicity measurements in the solar wind. Our convection-driven dynamo model with a coronal envelope has a solar-like differential rotation with radial (spoke-like) contours of constant rotation rate, together with a solar-like meridional circulation and a near-surface shear layer. The spoke-like rotation profile is due to latitudinal entropy gradient which violates the Taylor–Proudman balance through the baroclinic term. We find mean magnetic fields that migrate equatorward in models both with and without the coronal layer. One remarkable result is that the dynamo action benefits substantially from the presence of a corona becoming stronger and more realistic.

The two-layer model represents a new approach to describe the generation of coronal mass ejections in a self-consistent manner. On the other hand, it has important implications for solar dynamo models as it admits many magnetic features observed in the Sun.

List of Papers

The following papers are included in this thesis. They are referred to in the text by their Roman numerals,

I **Warnecke, J.**, & Brandenburg, A.: 2010, "Surface appearance of dynamo-generated large-scale fields", *Astron. Astrophys.*, **523**, A19

II **Warnecke, J.**, Brandenburg, A., & Mitra, D.: 2011, "Dynamo-driven plasmoid ejections above a spherical surface", *Astron. Astrophys.*, **534**, A11

III **Warnecke, J.**, Brandenburg, A., & Mitra, D.: 2012, "Magnetic twist: a source and property of space weather", *J. Spa. Weather Spa. Clim.*, **2**, A11

IV **Warnecke, J.**, Käpylä, P. J., Mantere, M. J., & Brandenburg, A.: 2012, "Emergence of magnetic structures driven by a convective dynamo with differential rotation above a spherical wedge", *Solar Phys.*, **280**, 299-319

V **Warnecke, J.**, Käpylä, P. J., Mantere, M. J., & Brandenburg, A.: 2013, "Solar-like differential rotation in a convective dynamo with a coronal envelope", *Astrophys. J.*, submitted, arXiv: 1301.2248

VI Käpylä, P. J., Mantere, M. J., Cole, E., **Warnecke, J.**, & Brandenburg, A.: 2013, "Effects of strong stratification on equatorward dynamo wave propagation", *Astrophys. J.*, submitted, arXiv: 1301.2595

My Contribution to the Papers

I Work on this paper started a few weeks after I began my PhD in August 2009. The main idea was developed by my supervisor and myself. I ran all the simulations, did most of the analysis and produced all the plots for the paper. I also did limited work on the implementation of the setup and developed some analysis tools using the PENCIL CODE[1] and IDL. I wrote the major part of the paper.

II In the beginning of the project, I spent time together with one of the co-authors transforming the equations and the setup of the Cartesian model to spherical geometry and implementing this in the PENCIL CODE. I performed the parameter study to identify a regime with stable simulations and performed all of the runs used in the paper. In addition, I coded analysis tools applied in IDL and the PENCIL CODE. I did the analysis and made all the plots used in the paper. The actual writing was done in collaboration with the co-authors, where I contributed a large fraction.

III This paper is based on work presented in **Papers I** and **III**. I performed a deeper analysis of the runs with respect to magnetic helicity and I made most of the analysis and plots in the paper. The writing and discussion was done mainly by myself.

IV On my initiative, I started a collaboration with co-authors Petri J. Käpylä and Maarit J. Mantere, using convective motions to generate magnetic fields in my setup. I developed the new setup involving the implementation of additional physics into the PENCIL CODE. I made a full parameter study to find a stable and efficient setup. I added new diagnostic tools in the PENCIL CODE, as well as in IDL. For the paper, I did all the runs, all the analysis, all the plots and wrote the first complete version of the text. The co-authors contributed to the discussion of the analysis and the text.

V I did all the improvements of a new setup including implementations in the PENCIL CODE. I made a large number of runs to find a stable and sufficient setup. I wrote new diagnostics in the PENCIL CODE and with IDL. I did all the runs related to the paper, all the analysis and plots and I

[1] `http://pencil-code.googlecode.com`

wrote all the text except some suggested additions and comments by the co-authors.

VI I contributed to the discussion of the setup, the analysis and the writing of the text.

To Atefeh,
The Star in my Universe

Contents

1. The Sun

Eins, Hier kommt die Sonne
Zwei, Hier kommt die Sonne
Drei, Sie ist der hellste Stern von allen
Vier, Hier kommt die Sonne

Rammstein

Its vicinity to the Earth makes the Sun an object that can be studied in such a precision and resolution than no other star. It reveals a multitude of complex processes and features, where we only know as much as the tip of an iceberg. Although there have been major advances in observing techniques and modeling of solar phenomena in the recent times, fundamental processes as the activity cycle of Sun are ill understood.

Let me start with an introduction to the structure of the Sun. In solar physics, we distinguish the solar interior, containing everything below the visible solar surface, from the solar atmosphere as everything above the solar surface. The solar surface is defined as the layer, where the optical depth at a continuum wavelength is unity. The density stratification from the center of the Sun to its surface varies by about nine orders of magnitudes. The temperature spans from 15 million Kelvin to around 6 thousand Kelvin. The solar interior can be divided into three main parts as shown in Fig. 1.1. In the inner part, the core, nuclear fusion supplies the main source of energy for this star. This energy is outwards transported through the radiative zone by radiation. The radiative zone extends from 0.3 to 0.7 solar radii and rotates as a solid body according to helioseismology. Above the radiative zone, the energy is predominantly transported via convection.

The definition of the solar atmosphere is somewhat ambiguous in the literature. Stix (2002), for example, defines the atmosphere as the photosphere and the chromosphere above. In other work, even the interplanetary space of the heliosphere is included. However, in this work I will define the solar atmosphere as the combination of the photosphere, chromosphere, transition region and solar corona. Near the surface of the Sun, heat is mainly transported as radiation and can leave the Sun freely. The thin surface layer is the lowest part of the solar atmosphere and is called photosphere, because it emits the largest amount of visible light of the total solar luminosity. The lower boundary of the chromosphere is usually defined by the temperature minimum on the

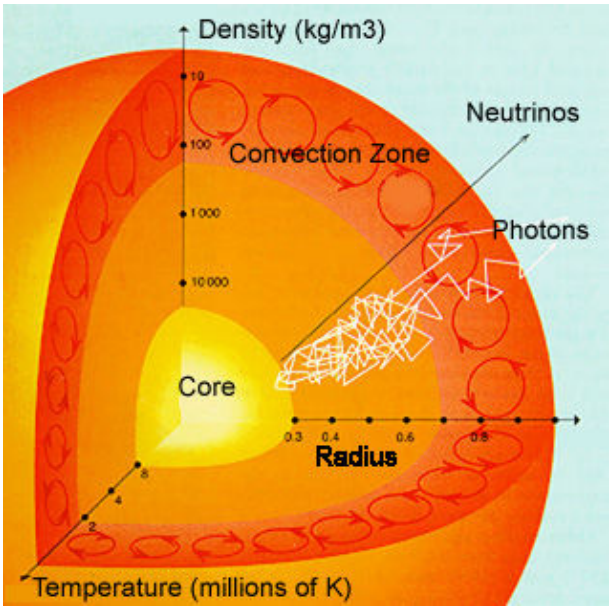

Figure 1.1: A cut-away schematic view of the solar interior, showing the main three parts: core, radiative zone, convection zone. Courtesy of the Center for Science Education of Berkeley, University of California, US.

Sun. The temperature structure of the chromosphere is heavily influenced by complex radiation processes which can only be described by non–equilibrium radiative transfer models. The temperature increases in the chromosphere is caused by one or several of the following heating mechanism; Joule heating, sonic and Alfvén waves. The structure and dynamics of the chromosphere are strongly dependent on the magnetic field and radiative energy transport. The intensity of chromospheric lines, e.g. the cores of Ca H & K, can be used to determine the magnetic activity of other stars than the Sun (see e.g. Noyes et al., 1984; Baliunas et al., 1995; Brandenburg et al., 1998; Saar and Brandenburg, 1999). At a height of around two megameters (Mm), the chromosphere ends and turns into the transition region. There, temperature rises sharply and the density drops by several orders of magnitude. This region represents the transition to solar corona. The corona extends to two to three solar radii, from which the solar wind takes over reaching far out into the interplanetary space.

In the following three sections, I describe these three layers of the Sun in more detail, because they are directly relevant to my work. In the last two sections, I give an overview about the cyclic behavior of magnetic activity of the Sun and the Sun-Earth relation.

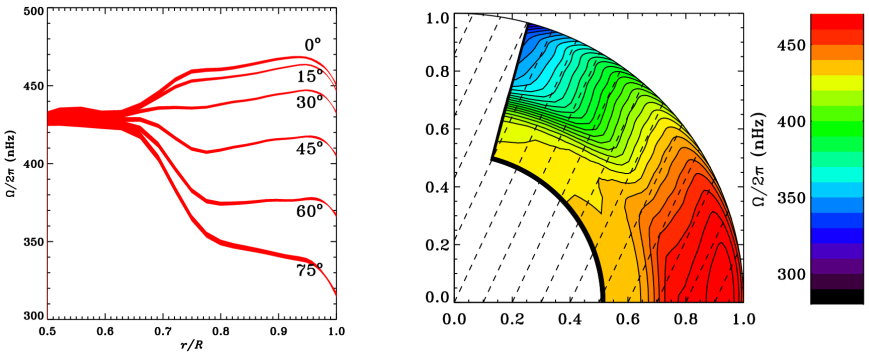

Figure 1.2: The internal differential rotation of the Sun as obtained from helioseismology. The bottom of the convection zone lies at $r = 0.713$ solar radii ($R_\odot$). Image courtesy of GONG.

1.1 The convection zone

In the convection zone, most of the energy is transported to the surface in convection cells, where hotter plasma rises, cools and sinks again; see § 2 for details. Typically, the size of the convection cells depends strongly on the depth due to strong ranging pressure scale height. At the bottom of the convection zone the cells are large, several tens of Mm. At the surface the cells have sizes of about one Mm and are called granules. In the convection zone these motions are highly turbulent. Additionally, the rotation of the Sun acts on the plasma motions as well and causes a differential rotation inside the convection zone. The equator of Sun rotates faster (25 days rotation period) than the poles (30 days). But the exact radial rotation was unknown until the advent of helioseismology. This technique, where one identifies discrete wave modes occurring on the surface of the Sun and invert their properties, allows to measure the velocity and temperature distribution inside the convection zone with a high precision. In Fig. 1.2 the rotation profile obtained by the Global Oscillation Network Group (GONG: Harvey et al., 1996) is shown. It matches the surface observation, where the equator rotates faster than the poles. But the differential rotation has also a radial dependence (see e.g. Thompson et al., 2003). Below the convection zone the radiative zone rotates with constant speed. However, the overlying convection zone has latitudinally dependent rotation and this leads to a region of strong velocity gradients (shear) at the bottom of the convection zone. This region is known as the tachocline (Spiegel and Weiss, 1980). A similar, but thinner region exists close to the surface, which is the Near Surface Shear Layer (NSSL), (see e.g. Thompson et al., 1996; Schou

et al., 1998). The overall rotation is clearly not a profile of cylindrical rotation, but the contours of constant rotation are parallel to the rotation axis. In the Sun the contours are *spoke-like*, i.e. they are pointing radially outward. Sunspot proper motions indicate a meridional circulation in the solar convection zone; first found by Tuominen (1941). The flow direction is poleward near the surface and equatorward inside the convection zone. Helioseismology measurements confirm the poleward flow near the surface, but where the equatorward return flow is located is not clear at the moment. There could even exist more than one cell of circulation (Hathaway, 2011).

The dynamics and the structure of the convection zone is an important field of research, because the turbulent motions of the convection together with the differential rotation are able to generate a large-scale magnetic field. The existence of a large-scale magnetic field inside the convection zone is not disputed and can be observed at the surface on the Sun. That there is a mechanism of creating a magnetic field, called solar dynamo is not disputed either. But the location, of the dynamo and how the dynamo works is still under discussion. It is commonly believed that the magnetic field itself back reacts on the turbulent motion and differential rotation as well. At the moment, there is no way to observe magnetic fields below the solar surface. Therefore, we have to rely on simulations of solar dynamo models and constraints from surface observations. In § 4, I present a selection of different solar dynamo models as well as their results.

1.2 The surface of the Sun

The surface of Sun is a region which gives us the most information about the solar interior. We can measure the velocity and the magnetic field with high precision and use the solar oscillations for helioseismology. The convection cells at the surface form a pattern, which is called granulation. The hot plasma flows up in the center of each cell and flows down at its boundaries. The magnetic field occurs at the surface at different scales. The small-scale field is located between the granules in the intergranular lanes. Plage regions, where the magnetic field is stronger than in the quite Sun can cover a region larger than several granules. Hence, the magnetic field is not strong enough to quench the fluid motions, but the granulation is small-scale and obviously disturbed by the magnetic field. The situation is even more extreme in a sunspot. The dark spots on the solar surface, of which the biggest ones can be seen with the naked (protected) eye from the Earth, have strong magnetic field of up to 4000 gauss. The magnetic field is so strong that it suppresses the convective heat transport. This makes the sunspot become 1000 Kelvin cooler than the surface around it, resulting in a dark spot. A beautiful image of a sunspot observed with the

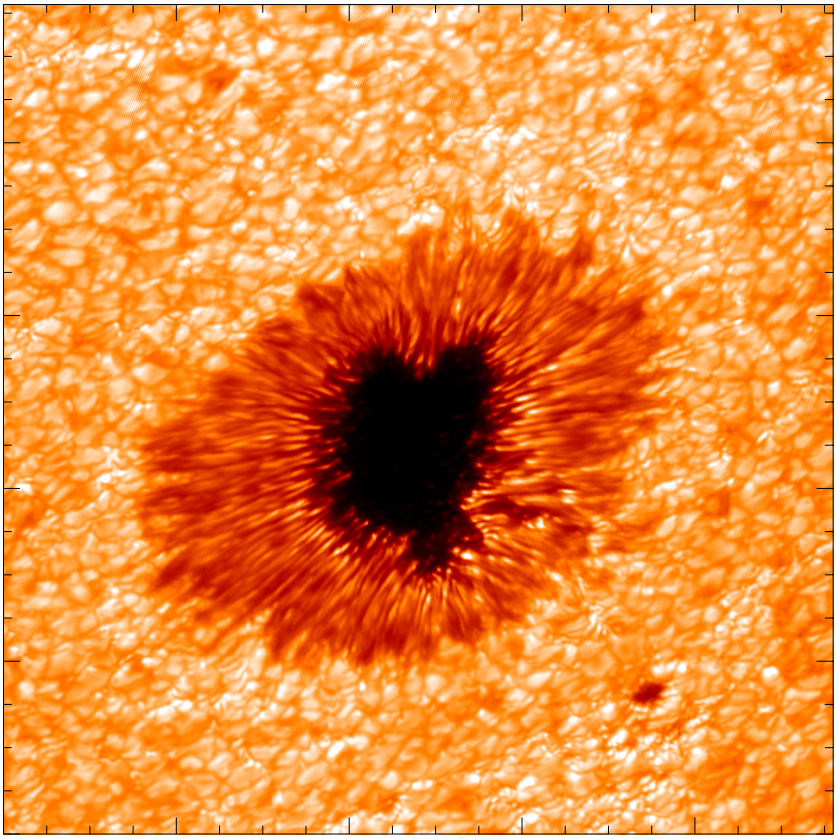

Figure 1.3: Image of a sunspot (AR1591). Observed with CRISP at the Solar Swedish Telescope (SST) on La Palma, Spain at a wavelength of 557.6 nm on 14th of October 2012. Observation and data reduction by Mats Löfdahl, Atefeh Barekat, and Jörn Warnecke.

Swedish 1-meter Solar Telescope can be seen in Fig. 1.3. Sunspots mostly occur as bipolar magnetic concentration with a leading (in terms of rotation) spot and a following spot or plage.

The dynamics and properties at the surface are determined by the radiative cooling of the hot plasma coming from the interior toward the surface. The surface of the Sun is called the photosphere and corresponds to the layer, where the optical depth of the continuum is unity. The strong radiative cooling leads to a strong temperature and therefore density gradient close to the surface.

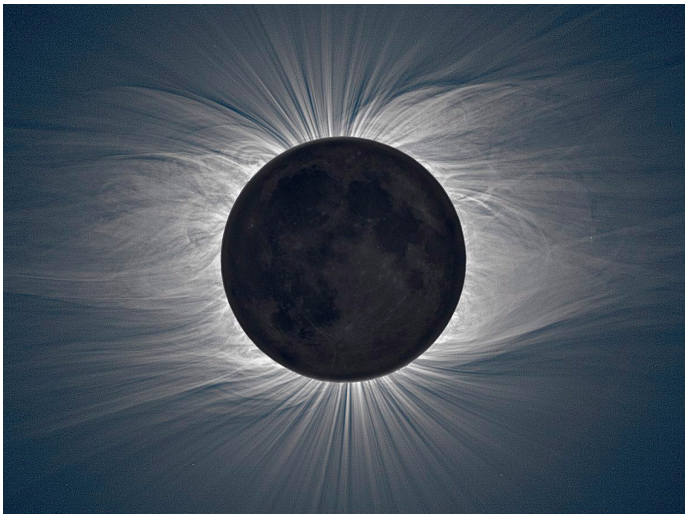

Figure 1.4: White light image of the solar corona during a solar eclipse 2009, observed at Enewetak Atoll, Marshal Islands. Composition of 38 eclipse images. Image processing by Miloslav Druckmüller. Courtesy: Miloslav Druckmüller, Peter Aniol, Vojtech Rusin, Lubomir Klocok, Karel Martisek, Martin Dietzel. `www.zam.fme.vutbr.cz/~druck/Eclipse/index.htm`

1.3 The solar corona

The solar corona is the outer part of the solar atmosphere and reaches out to several solar radii. The temperature in the corona is up to two—in coronal loops even ten—million of Kelvin, which leads to emission lines of highly ionized atoms. But because of the smaller density, which is nine orders of magnitude lower than in the photosphere, it is difficult to observed these lines. They are only observable from Earth during a solar eclipse (as shown in Fig. 1.4) or using a coronagraph, where the photospheric light is covered by an occluding disk. From space, one is able to measure the corona in ultraviolet and X-rays. Due to the low density, the magnetic pressure is stronger than the gas pressure (plasma $\beta = \frac{2\mu_0 p}{B^2} \ll 1$). This means that the resulting Lorentz force dominates inside the corona, and plasma flows along the field lines. Most of the emission comes from the hot plasma moving along magnetic field lines. Therefore the observed plasma structure corresponds directly to the magnetic field structure, as shown in Fig. 1.4. One of the unsolved problems in solar physics is the heating of the corona. The corona is several hundred times hotter than the solar surface and need therefore an additional heating source to sustain this high temperature. Numerical simulations have shown that braid-

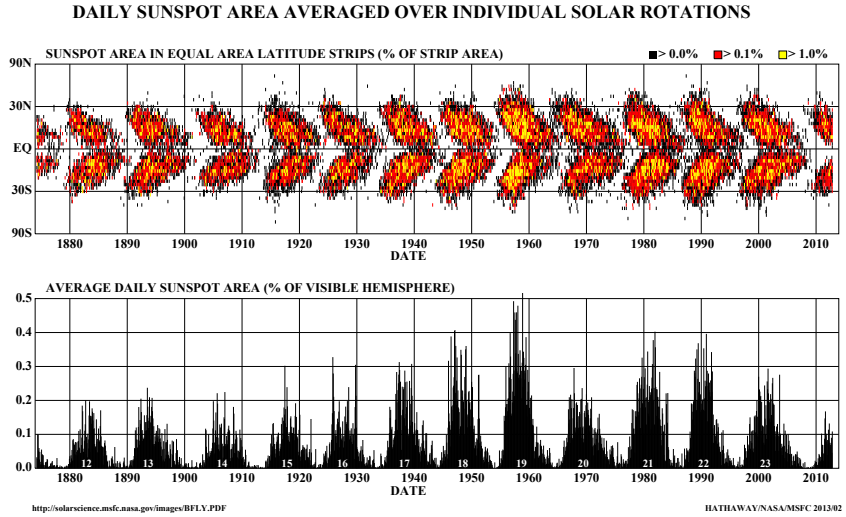

Figure 1.5: Time evolution of the sunspots area. The *upper panel* show the sunspots area in the dependence to the latitude over time. In the *lower panel* the average daily sunspots area is given over time. Graphics and Data courtesy of David Hathaway, NASA Marshall Space Flight center for Solar Physics.

ing of field lines at their footpoints in the photosphere can dissipate enough energy via Ohmic heating to produce coronal temperatures (see e.g. Gudiksen and Nordlund, 2005a; Bingert and Peter, 2011). However, there are other proposed mechanisms which also can lead to such high temperatures: Ohmic heating, sonic and Alfvén waves (see e.g. Aschwanden et al., 2007).

1.4 The solar cycle

Already Galileo Galilei observed sunspots as dark spots on the solar surface, although he thought they were clouds. He counted them and noted their numbers. But only in the 19th century, Schwabe (1844) discovered a cyclic variation with a period of around 10 years. Today we have data of sunspot numbers reaching all the way back to the days Galilei. These data led to an averaged cycle period of the sunspot numbers to be around 11 years (Schwabe's cycle). At solar maximum we can observe several hundred sunspots each month, while

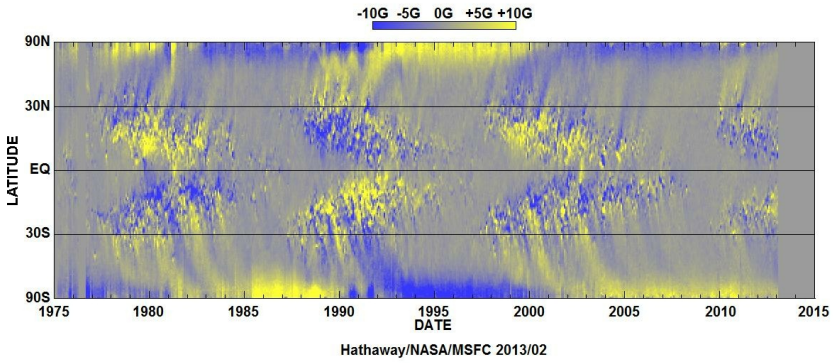

Figure 1.6: Synoptic magnetogram of three and a half solar cycles. Color coded is the radial magnetic field, which is plotted as the averaged magnetograms during the cycles. Graphics and Data courtesy of David Hathaway, NASA Marshall Space Flight center for Solar Physics.

at minimum there may be just a few, or none. In the recent history of the Sun, there have been cycles with just a few sunspots even for a several month during maximum. One prominent example is the Maunder Minimum (1650–1750), where only a few spots even during the maxima were observed. This was the time of the little ice age in Europe. If the Maunder Minimum and the ice age are correlated is highly debated at the moment.

More detailed observations revealed a spatial distribution of the sunspots' occurrence. As shown in Fig. 1.5, at the beginning of each cycle, sunspots emerge preferably at higher latitudes, while at the end of each cycle they emerge at lower latitudes (near the equator). This is often called a *butterfly diagram*, because variation of the latitude of sunspots occurrence with time is reminiscent of the wings of a butterfly. The overall preferred latitudes are between $\pm 30^\circ$. The number of sunspots of each maximum changes with every cycle. Data of hundreds of years of sunspot observation suggest a secondary overlying cycle with a period of around 100 years, which is called the Gleissberg cycle (Gleissberg, 1976). The current cycle is in the decaying phase a Gleissberg cycle, which had its maximum in the middle of last century (see e.g. Feynman and Ruzmaikin, 2011).

Since Hale (1908) and Hale et al. (1919) we know that sunspots correspond to magnetic field concentrations. The cyclic occurrence of the sunspots must be strongly correlated to the magnetic field inside the Sun. Every eleven years the sunspot pairs at the solar surface reverse their magnetic polarity. If observed sunspot pairs on the northern hemisphere have leading positive po-

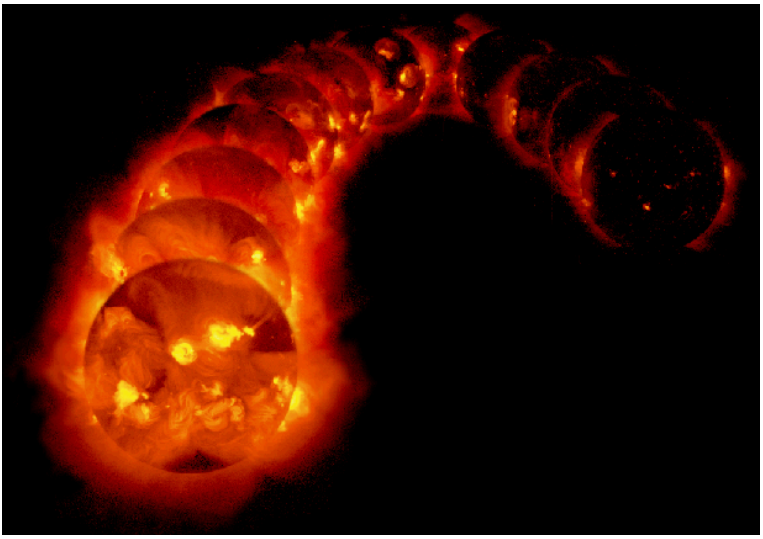

Figure 1.7: Evolution of solar activity in X-rays. The photographs were taken every 90 days by the satellite Yohkoh, a cooperative mission of Japan, the USA, and the UK, in the years 1991–1995.

larity, spot pairs on the southern hemisphere have leading spots with negative polarity. During the next sunspot cycle the leading spots on the northern hemisphere have negative polarity and positive polarity on the southern hemisphere (Hale et al., 1919). This behavior is a manifestation of the 22-year magnetic cycle (Hale's cycle). Synoptic magnetograms such as Fig. 1.6, where magnetograms are averaged in the time-latitude-plane, clearly show the magnetic cycle: the polarity reverses every eleven years. The oscillation and the equatorward migration of the magnetic field is an important observational evidence for a solar dynamo operating below the surface. With a primordial field, which has been amplified in the formation process of the solar system, such a behavior cannot be explained (see e.g. Dicke, 1978; Rosner and Weiss, 1992).

The solar cycle is seen not only at the visible surface. X-ray observation of the solar corona show a strong cyclic dependence, as illustrated in Fig. 1.7. The corona is hotter and more structured during solar maximum (see e.g. Wang and Sheeley, 2003). These variations are manifestations of a close relation between the solar cycle and strong variations in solar activity related to magnetic fields. This includes eruptive events like solar flares and coronal mass ejections, where huge amounts of energy are released. The overall solar irradiation is also cycle dependent (first reported by Willson and Hudson, 1988). Even though sunspots are dark and their coverage of the solar surface is higher at

solar maximum (see Fig. 1.5), the solar irradiance is higher, because of the increased amount of bright points, associated with small-scale strong magnetic fields. Also the solar wind changes its structure during the cycle. At solar maximum coronal holes occur more frequently. These holes are often the source of the fast solar wind, which has speeds up to $800\,\mathrm{kms}^{-1}$ (see e.g. Cliver et al., 1996). With a stronger solar wind and higher magnetic field strengths, the solar magnetosphere can shield more effectively cosmic ray particles entering our solar system. This might be related to a modulation of the cloud production in the Earth atmosphere and so influence the climate on Earth (Svensmark and Friis-Christensen, 1997; Lübken et al., 2009).

1.5 Space weather

Space Weather describes the momentary condition of the Sun-Earth interaction, see the right panel of Fig. 1.8 for an artist illustration. A huge amount of energy can be stored in the magnetic field generated by the dynamo in the Sun. This energy can be partially released in violent eruptions. One of the prominent examples are solar flares, where magnetic reconnection releases energy directly via radiation mostly in Hα and the X-ray spectrum. These events are most visible in the solar chromosphere and the corona. The other prominent events are coronal mass ejections (CMEs), where plasma of the solar corona is ejected into the interstellar space. The plasma clouds cause shocks, which can accelerate particles to high velocities. An observed CME is shown in the left panel of Fig. 1.8, where a typical three-part structure (Low, 1999) is clearly visible. It comprises an outer arc-like structure of compressed coronal plasma, which piles up in front of its core. The inner bright core is the original ejected prominence. The third part is the cavity between the two bright structures. For details on solar eruption models see § 5.

These eruptive events can have strong impacts on our daily life. Beside the cultural and touristic influence of aurorae in arctic latitudes, these accelerating particles can endanger human technology and life. The Earth's magnetosphere prevents the main contribution of the particles and from the vicinity of the Earth. Outside the magnetosphere, where for example the solar satellite SOHO is operating, the radiation can be very strong. Microelectronics can be damaged and the particle radiation can endanger the life of astronauts. Flight to the Moon or to Mars is therefore very risky also from this perspective. As an example, between the missions of Apollo 16 and 17 a strong flare erupted in August 1972. It was energetic enough to endanger the life of the astronauts during the Apollo missions, had they been on the way to or on the moon (near-earth orbit doses from the solar flare on August 4, 1972 can be found in Savun and Sladkova, 1976, and estimates of a hypothetical interplanetary crew

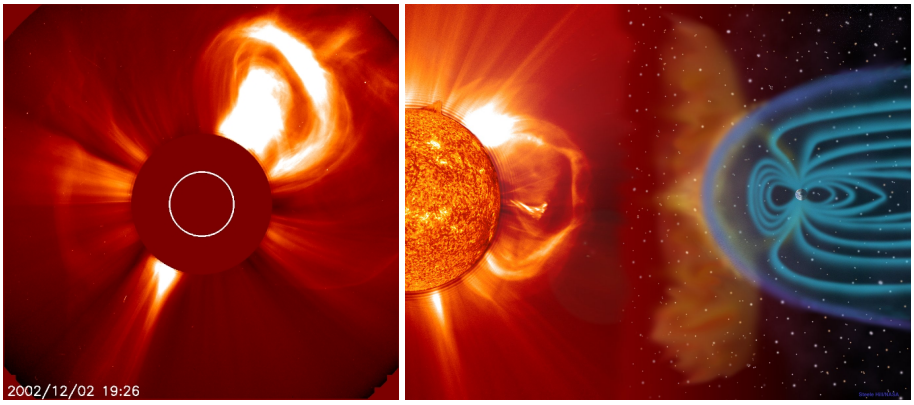

Figure 1.8: *Left panel*: This SOHO LASCO C2 image shows a very large coronal mass ejection (CME) blasting off into space on 2 December 2002. It presents the standard shape of a CME: a large bulbous front with a second, more compact, inner core of hot plasma. This material erupts away from the Sun at speeds of one to two million kilometers per hour. *Right panel*: Artist illustration of Sun-Earth interactions using a disk and a coronal image from SOHO. Image credit NASA.

dose during a strong solar flare in Stephens et al., 2005). Inside the Earth's magnetosphere the damage to microelectronics on satellites on typical near-Earth orbits is small. Strong impacts are caused by the interaction of accelerated particles and magnetic fields of CMEs and the Earth's magnetosphere. Depending on the field polarity, the magnetic field can trigger reconnection event in the Earth's magnetic fields. These events then can cause geomagnetic storms inside the Earth's magnetotail. Geomagnetic storms consist of accelerated energetic particles, which follow the field lines of the Earth's magnetic field toward the polar regions, where they are visible as aurorae. If the energy of the CME is strong enough, the geomagnetic storms can penetrate to lower latitudes, which leads to aurorae also there. The magnetic north pole—which is actually a south pole in the magnetic sense—does not have the same location as the geographical north pole, it is shifted by around 5° toward Alaska. This led to aurorae being visible at lower latitudes on the American continent than in Asia or Europe. Besides the aurorae, the impact of geomagnetic storms can be much more dramatic on the American continent than elsewhere at the same latitudes. There are two main risks to humans, one is primary, the other one is secondary. The primary risk is to be exposed to high radiation doses, for example on polar flights, which can easily exceed the annual safe limit (see e.g. Lantos, 2003). The secondary risk basically is the damage to infrastructure. Due to large geomagnetic induced currents, generators and transformer stations can be destroyed and lead to large power grid failures. In recent history

there were several events of such power grid failures. One prominent example is the Quebec blackout in March 1989, where the city was without any power for 9 hours. This geomagnetic storm was so strong that aurorae were seen in Florida and Texas. However, much stronger storms are possible and can cause even larger damages. It is not unrealistic to think of power grid failures that last for several days in a large high populated region. Even in the summer time this would cause a lot of problems. Additionally, telecommunication and navigation systems are disturbed and can stop functioning. Nowadays, our society depends more and more on technologies that are highly vulnerable by solar eruptions.

The name *space weather* also indicates that the time scales of these events are rather short and comparable to those of weather on Earth. A CME needs one to five days to reach the Earth. Because of the strong impact on the Earth, several countries have installed early warning systems to be prepared. Today, we are monitoring the Sun with numerous space and ground based telescopes everyday—even looking with STEREO on the far-side of the Sun—to know, when the next CME will hit the Earth. However, to forecast and predict solar space weather, one should understand two important ingredient in more detail. One is the solar activity cycle. Observations show that solar eruptions happen preferably during solar maximum, i.e. when the magnetic field is relative strong (Schwenn, 2006). Modeling the solar activity cycle with a solar dynamo model will be part of my thesis and involves mostly **Papers V** and **VI**. The other ingredient is the emergence and eruption of magnetic fields from the solar convection zone through the solar atmosphere into the interplanetary space. The generation of magnetic field configurations, which then eventually trigger reconnection and liberation of magnetic energy and plasma, seems to be crucial for CME modeling. My contribution to modeling coronal ejections using an alternative approach also is part of my thesis and is described in **Papers I, II, III** and **IV**.

2. Solar Convection, Turbulence and Rotation

You can check-out any time you like,
But you can never leave!

Eagles

2.1 Convective motions

Convection is an important mechanism to transform thermal energy into kinetic energy. This is of particular interest in astrophysics, because large gradients of temperature together with gravity are often found in astrophysical environment, like in Galaxies, in accretion disks or in the interior of stars. Motions caused by convection are in most astrophysical environment turbulent and can lead to interesting physical phenomena, for instance, enhanced mixing of metals, generation of magnetic fields via a dynamo instability (see § 3.2 and § 4) or the footpoint motion of magnetic fields on the solar surface, leading to coronal heating (see e.g.Gudiksen and Nordlund, 2005a; Bingert and Peter, 2011).

2.1.1 The convective instability

Let us assume a simple explanatory case: We have a very large container of a perfect gas in hydrostatic equilibrium, with the vertical coordinate z. Gravitational acceleration is locally uniform pointing in the negative z direction $\boldsymbol{g} = -g\hat{\boldsymbol{z}}$, which leads to a decrease of density $\rho(z)$ and pressure $p(z)$ with height z. Now, we consider a blob of radius r, which has the same values of density ρ and pressure p as its surrounding medium. We displace the blob a small distance upwards against gravity; in Fig. 2.1 a sketch of the blob is shown. The density ρ' and pressure p' of the surrounding medium have decreased, so that $\rho' < \rho$ and $p' < p$. If the adiabatic time scale is much larger than the diffusion time scale, we can assume that the difference in pressure between the blob and the surrounding will reach a new balance rather quickly and will cause an adiabatic expansion of the blob $r \to r + \delta r$. But the exchange of heat is comparably slow, which can lead to a difference in temperature and

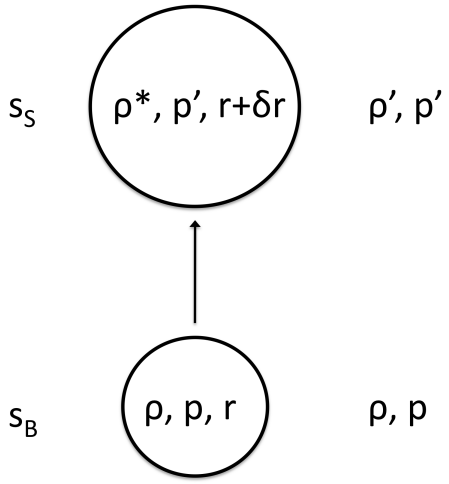

Figure 2.1: Moving a blob of gas upwards in a stratified surrounding.

therefore to a density ρ^* inside the blob which is different from ρ'. If the density inside the blob ρ^* is higher than in its surroundings, it is heavier and moves back downwards; the gas is stable. If the density inside the blob ρ^* is lower than in the surroundings, it moves upwards due to the buoyancy force; the gas is convectively unstable. This can be expressed by looking at the difference in the specific entropy s (i.e entropy per unit mass) of the blob and its surrounding medium. In a perfect gas this change of entropy is given by

$$\Delta s = c_{\mathrm{V}} \Delta \ln p - c_{\mathrm{P}} \Delta \ln \rho, \tag{2.1}$$

where c_{V} is the specific heat at constant volume and c_{P} is the specific heat at constant pressure. Let us now calculate the density difference $\Delta \ln \rho = \ln \rho^* - \ln \rho'$

$$\Delta \ln \rho = -\frac{1}{c_{\mathrm{P}}} \Delta s + \frac{1}{\gamma} \Delta \ln p \tag{2.2}$$

where $\gamma = c_{\mathrm{P}}/c_{\mathrm{V}}$ is the adiabatic index. The pressure difference balances to zero ($\Delta \ln p = 0$) leading to the expansion of the blob. Because the blob has been displaced adiabatically, its entropy stayed constant and we can express the entropy difference as a gradient over height. We can calculate the density difference as

$$\rho^* - \rho' = \frac{\rho'}{c_{\mathrm{P}}} \frac{\mathrm{d}s}{\mathrm{d}z} z. \tag{2.3}$$

This equality expresses directly the relation between the dynamics of the blob and the entropy gradient. If the entropy gradient is positive, the blob becomes

heavier as it rises and is pulled downward by gravity. If the entropy gradient is negative, the blob becomes lighter as it rises and continues to rise. Solving a simplified momentum equation of the blob, we can express this behavior in terms of a frequency. This frequency N is called *Brunt–Väisälä frequency* and can be deduced from Eq. (2.3) to

$$N = \sqrt{\frac{g}{c_\mathrm{P}} \frac{\mathrm{d}s}{\mathrm{d}z}}, \tag{2.4}$$

where g enters because gravity is the restoring force. If N is a real number, the gas is convectively stable, and the blob will oscillate with the frequency N. If N is imaginary, the gas is convectively unstable, and the blob moves further upward and causes an instability. This is equivalent to the *Schwarzschild instability criterion*

$$\frac{\mathrm{d}\ln T}{\mathrm{d}\ln P} = \nabla > \nabla_\mathrm{ad} = \left(\frac{\mathrm{d}\ln T}{\mathrm{d}\ln P}\right)_s, \tag{2.5}$$

where ∇_ad is the double-logarithmic isentropic temperature gradient. The double-logarithmic temperature gradient ∇ is not to be confused with *nabla operator* $\boldsymbol{\nabla}$ in div, grad, and curl.

For cases, where the adiabatic time scale is comparable or smaller than the typical diffusive one, we need to define a more general criterion. In general, a fluid with a negative entropy gradient can be convectively unstable, if the diffusivities are small enough. There, the instability criterion can be expressed by the non-dimensional *Rayleigh number* (Jeffrey, 1926)

$$\mathrm{Ra} = \frac{g d^4}{\nu\chi} \left(-\frac{1}{c_\mathrm{P}} \frac{\mathrm{d}s}{\mathrm{d}z}\right)_0, \tag{2.6}$$

where d is the height of the domain, ν the kinematic viscosity and χ the heat diffusivity, which is related to the heat conductivity $K = c_\mathrm{P}\chi\rho$. The entropy gradient $\mathrm{d}s/\mathrm{d}z$ is either taken as an average or at a certain location. A meaningful Rayleigh number can only be calculated from the hydrostatic reference solution, which is indicated by the 0. For every system, there exists a critical positive Rayleigh number $\mathrm{Ra}_\mathrm{crit}$, above which the gas is (linearly) convectively unstable.

$$\mathrm{Ra} > \mathrm{Ra}_\mathrm{crit} \Rightarrow \text{unstable} \tag{2.7}$$

For a non-rotating fluid without magnetic field the relation above corresponds to Eq. (2.5). To determine this number analytically is nearly impossible and depends on the boundary conditions. If the Rayleigh number in a system is very large, the gas would likely be convectively unstable.

A more detailed discussion of the derivation and the calculation of the instability criteria can be found in Choudhuri (1998) and Stix (2002).

2.1.2 Fluid dynamics

In many astrophysical systems the mean-free path of particles, like ions and electrons in a plasma, is much smaller than the typical physical length scale. This allows us to use the continuum mechanics for fluid dynamics. For example in the solar convection zone the typical mean-free path of the ions and electrons is of the order of $\lambda = 10^{-8}\,\mathrm{cm}$ and the typical length scale is the pressure scale height $H_P = 10^{10}\,\mathrm{cm}$, which satisfies the fluid dynamic approach. For describing changes and evolutions of fluid quantities, we use typically the Lagrangian or convective derivative, which moves along with the fluid motions

$$\frac{\mathrm{D}}{\mathrm{D}t} = \frac{\partial}{\partial t} + \boldsymbol{u}\cdot\boldsymbol{\nabla}, \tag{2.8}$$

where $\boldsymbol{u}$ is the fluid velocity. The conservation of mass leads to the continuity equation

$$\frac{\mathrm{D}\rho}{\mathrm{D}t} = -\rho\boldsymbol{\nabla}\cdot\boldsymbol{u}, \tag{2.9}$$

which is often rewritten with the logarithmic derivative as

$$\frac{\mathrm{D}\ln\rho}{\mathrm{D}t} = -\boldsymbol{\nabla}\cdot\boldsymbol{u}. \tag{2.10}$$

The conservation of momentum is given by the Navier–Stokes equation

$$\rho\frac{\mathrm{D}\boldsymbol{u}}{\mathrm{D}t} = \rho\boldsymbol{g} - \boldsymbol{\nabla}p + \boldsymbol{\nabla}\cdot 2\nu\rho\mathsf{S} + \boldsymbol{F}, \tag{2.11}$$

which is often also written in terms of the velocity evolution equation

$$\frac{\partial\boldsymbol{u}}{\partial t} = -\left(\boldsymbol{u}\cdot\boldsymbol{\nabla}\right)\boldsymbol{u} + \boldsymbol{g} + \frac{1}{\rho}\left(-\boldsymbol{\nabla}p + \boldsymbol{\nabla}\cdot 2\nu\rho\mathsf{S} + \boldsymbol{F}\right), \tag{2.12}$$

where the traceless rate-of-strain tensor S is given by

$$\mathsf{S}_{ij} = \tfrac{1}{2}(u_{i,j} + u_{j,i}) - \tfrac{1}{3}\delta_{ij}\boldsymbol{\nabla}\cdot\boldsymbol{u}, \tag{2.13}$$

and $\boldsymbol{F}$ includes additional forces originating, for example, from the magnetic field or rotation of the frame; ν is the microphysical kinematic viscosity. The contributions in the momentum equation can be categorized in three parts. There are the terms of forces which are set by the environment or the state of the fluid; the gravitational acceleration $\boldsymbol{g}$ and the pressure gradient $\boldsymbol{\nabla}p$ count to this category. Then there is the diffusion term $\frac{1}{\rho}\boldsymbol{\nabla}\cdot 2\nu\rho\mathsf{S}$, which includes second derivatives and will—as suggested by the name—smooth out strong velocity gradients. The third term $(\boldsymbol{u}\cdot\boldsymbol{\nabla})\boldsymbol{u}$ is the advection term and it is non-linear in the velocity $\boldsymbol{u}$. The last one is the most interesting term. Because

of its non-linearity it makes analytic descriptions of the fluid difficult. One of the consequences of non-linearity is turbulence, which will be discussed in § 2.2. We can define a meaningful dimensionless number called the Reynolds number by comparing advection and diffusion terms

$$\mathrm{Re} \equiv \frac{\|(\boldsymbol{u}\cdot\boldsymbol{\nabla})\,\boldsymbol{u}\|}{\left\|\frac{1}{\rho}\boldsymbol{\nabla}\cdot 2\nu\rho\mathsf{S}\right\|} \approx \frac{UL}{\nu}. \tag{2.14}$$

U is the typical velocity of the system, L its typical length scale and $\|\cdot\|$ defines a norm, which has to be chosen specifically for the setup. The first term, which represents the exact definition is often called *term-based* Reynolds number. For Reynolds numbers of the order of unity or smaller, diffusion dominates and the flow is laminar; for Reynolds numbers much larger than unity, non-linearities dominate and the flow becomes turbulent. Typical values of the Reynolds number for the solar interior are $\mathrm{Re} \approx 10^{12}...\ 10^{13}$. Note that the Reynolds number depends on the length scale under consideration; choosing the relevant length scale for a specific setup can be difficult. In **Papers I-VI**, we define the Reynolds number as $\mathrm{Re} = u_{\mathrm{rms}}/k_{\mathrm{f}}\nu$, where k_{f} is the wavenumber of the energy carrying scale and u_{rms} the root-mean-square velocity, see Eq. (2.24). As an example, in one of the simulation setups of **Paper V** $\mathrm{Re} = 50$, but the *term-based* Reynolds number is ≈ 5. The difference of one order of magnitude might be related to our choice of L, which we set to correspond to the depth of the convection zone. Using the pressure scale height near the surface as a more appropriate choice of L leads to an equality of the *term-based* Reynolds number and $\mathrm{Re} = u_{\mathrm{rms}}/k_{\mathrm{f}}\nu$. However, the norm used to determine the *term-based* Reynolds number plays a crucial role.

2.2 Turbulence

Turbulence is often present in astrophysics, but it is actually difficult to define accurately. We can call a flow turbulent, if the Reynolds number is very high and therefore fluid flows non-laminar. Turbulence can be also defined as a flow, in which the correlation length and correlation time become finite. The flow generates structures such as eddies and becomes in general more complex. It is easier to illustrate this with a simple example. Consider a fluid with a certain velocity and viscosity ν that flows around a cylinder; similar to a bridge pillar in a river. Assuming that the viscosity remains constant, we increase slowly the velocity and therefore the Reynolds number. In Fig. 2.2, we show an illustration of this behavior. For Reynolds numbers $\mathrm{Re} < 5$ the flow around the cylinder is fully laminar and without any disturbance, e.g. the flow patter in the front of the cylinder is the same as that behind the cylinder. For Reynolds

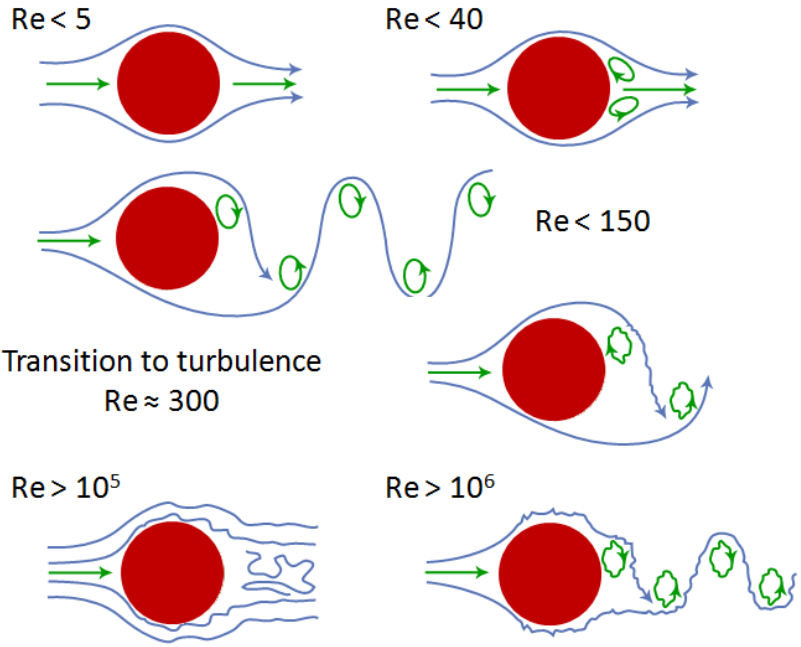

Figure 2.2: Flow past a cylinder for different values of the Reynolds number, from laminar to fully turbulent (Lienhard, 1966). Image courtesy of Koen Kemel.

numbers $\mathrm{Re} < 40$, we find a weak return flow associated with two eddies at the back of the cylinder. When the Reynolds number is increased to $\mathrm{Re} \lesssim 150$, then the eddies are ejected into the flow, which leads to an oscillatory flow pattern behind the cylinder. For even higher Reynolds numbers $\mathrm{Re} \approx 300$, transition to turbulence takes place and the flow pattern becomes very complex. Higher Reynolds numbers make the flow even more distorted and give rise to eddies at a range of different scales.

2.2.1 Kolmogorov turbulence

For isotropic homogeneous turbulence, we can describe some properties with the Kolmogorov theory (see e.g. Frisch, 1995). If we have a fluid in a statistically stationary state and we inject energy at a certain scale to sustain the turbulence, for example by stirring, we can apply this theory. Assuming the energy injection scale is large, then the corresponding wavenumber k is small. The energy spectrum will have a peak at this scale. Kolmogorov's theory predicts that the energy cascades toward smaller length scales with a constant slope as $k^{-5/3}$. At a certain scale for which $\mathrm{Re} = u_{\mathrm{rms}}/k\nu \approx 1$, depending on

the viscosity ν, this power law changes to an exponential decrease. This scale is called the dissipative scale. At this scale the kinetic energy of the motions is dissipated to thermal energy via viscous heating.

2.2.2 Mean-field theory

Turbulence is a small-scale phenomenon but can contribute to large scales significantly (see e.g Frisch, 1995). For example, at every airport in the winter time, the wings of the airplanes are cleaned from ice before take-off. Otherwise *icing* can give a rougher wing surface causing turbulent motions along the wing. This leads to a change of the aerodynamic lift of the plane.

Describing the small scales of a fluid as well as its large scales in one consistent theory is very challenging. In addition, in numerical experiments of high Reynolds number turbulent flows, the grid resolution often is too small to resolve sufficiently a large range of scales. Mean-field theory is one way to approach this problem. There, the small-scale physics is modeled or parametrized in terms of mean-field quantities (see e.g. Rüdiger, 1989). A field $\boldsymbol{f}$ can be decomposed into a mean or averaged part $\overline{\boldsymbol{f}}$ and a fluctuation part $\boldsymbol{f}'$

$$\boldsymbol{f} = \overline{\boldsymbol{f}} + \boldsymbol{f}'. \tag{2.15}$$

The definition of the averaging procedure is arbitrary and only needs to satisfy the Reynolds rules,

$$\overline{\boldsymbol{f}'} = 0 \tag{2.16}$$

$$\overline{\boldsymbol{f}+\boldsymbol{h}} = \overline{\boldsymbol{f}}+\overline{\boldsymbol{h}} \tag{2.17}$$

$$\overline{\left(\frac{\partial \boldsymbol{f}}{\partial x_i}\right)} = \frac{\partial \overline{\boldsymbol{f}}}{\partial x_i} \tag{2.18}$$

$$\overline{\overline{\boldsymbol{f}}\boldsymbol{h}} = \overline{\boldsymbol{f}}\,\overline{\boldsymbol{h}} = \overline{\boldsymbol{f}}\,\overline{\boldsymbol{h}}, \tag{2.19}$$

$$\overline{\overline{\boldsymbol{f}}\boldsymbol{h}'} = 0 \tag{2.20}$$

where $\boldsymbol{h}$ is an arbitrary field and x_i an arbitrary direction including time. Typically the average is over time and/or one spatial direction. We can now rewrite the Navier–Stokes equation (2.12) in terms of mean quantities.

$$\frac{\partial \overline{\boldsymbol{u}}}{\partial t} = -\left(\overline{\boldsymbol{u}}\cdot\boldsymbol{\nabla}\right)\overline{\boldsymbol{u}} + \boldsymbol{g} + \frac{1}{\overline{\rho}}\left(-\boldsymbol{\nabla}\overline{p} + \boldsymbol{\nabla}\overline{\rho}\mathfrak{Q} + \boldsymbol{\nabla}\cdot 2\nu\overline{\rho}\overline{\mathbf{S}} + \overline{\boldsymbol{F}}\right), \tag{2.21}$$

where we neglect additional terms involving correlation with fluctuating density ρ'. $\overline{\boldsymbol{F}}$ includes additional forces coming for example from the large-scale and small-scale magnetic field. $\mathfrak{Q}$ is the Reynolds stress tensor representing

stress contributions due to the small-scale velocities as a second order correlation tensor and can be parametrized in terms of the mean flow. The components of this tensor are given for isotropic turbulence by

$$Q_{ij} = \overline{u_i' u_j'} = -\nu_\mathrm{t} \left(\frac{\partial \overline{u}_i}{\partial x_j} + \frac{\partial \overline{u}_j}{\partial x_i} \right) - \zeta_t \delta_{ij} \frac{\partial \overline{u}_k}{\partial x_k}, \tag{2.22}$$

where ν_t and ζ_t are the turbulent shear and bulk viscosities. They are parameters, which have to be calculated from the small-scale physics in the system. The Reynolds stresses (2.22) are clearly dissipative and can be interpreted as a representation of energy transfer to smaller non-resolved scales. The term of the Reynolds stresses in the mean Navier–Stokes equation can be combined with its mean diffusive term by adding the turbulent viscosity ν_t to the microphysical viscosity ν to give a total viscosity $\nu_\mathrm{T} = \nu + \nu_\mathrm{t}$. In most astrophysical objects the turbulent viscosity is much higher than the molecular one, therefore $\nu_\mathrm{T} \approx \nu_\mathrm{t}$.

2.2.3 Mixing length theory

Solving the turbulent hydrodynamic equations for stellar structure models is a complex problem, in particular, because the turbulent aspects of stellar convection are not fully understood. One way to estimate the turbulent viscosity ν_t in the solar interior is by using mixing length theory (see e.g. Stix, 2002). To simplify the equations, we can define a specific length scale, the mean-free-path of a convective blob. This length gives the distance, which a convective blob travels before it is completely mixed with the surroundings. This *mixing length* l is related to the typical length scale of the system, the pressure scale height H_P (Vitense, 1953) by,

$$l = \alpha_\mathrm{MLT} H_P \quad \text{with} \quad H_P = -\left(\frac{1}{p} \frac{\partial p}{\partial r} \right)^{-1}, \tag{2.23}$$

where α_MLT is a free parameter of $\mathcal{O}(1)$. A good estimate of the typical turbulent velocity of a system is given by the root-mean-squared velocity u_rms, defined as

$$u_\mathrm{rms} = \sqrt{\overline{(\boldsymbol{u}')^2}}. \tag{2.24}$$

The turbulent viscosity ν_t is related to the mixing length via (Prandtl, 1926)

$$\nu_\mathrm{t} = \tfrac{1}{3} u_\mathrm{rms} l = \tfrac{1}{3} \alpha_\mathrm{MLT} u_\mathrm{rms} H_P. \tag{2.25}$$

Clearly, the rms velocity u_rms as well as the pressure scale height H_P are depth dependent. In Table 2.1 the temperature, density, scale height, rms velocity and the turbulent viscosity are shown for different heights z in a solar mixing length model of Spruit (1974).

Table 2.1. The solar mixing length model of Spruit (1974).

z [Mm]	T [K]	ρ [g cm^{-3}]	H_P [Mm]	$u_{\rm rms}$ [m/s]	τ [d]	$\nu_{\rm t}$ [cm^2/s]
24	1.8×10^5	0.004	8	70	1.3	1.5×10^{12}
39	3.0×10^5	0.010	13	56	2.8	2.0×10^{12}
155	1.6×10^6	0.12	48	25	22	3.2×10^{12}
198	2.2×10^6	0.20	56	4	157	0.6×10^{12}

Note. — z is the distance to the solar surface, T the temperature, ρ the density, H_P the pressure scale height and τ is the typical turnover time of a convective cell. $\nu_{\rm t}$ is the calculated turbulent viscosity according to (2.25).

2.2.4 Turbulent heat transport

The heat transport in the convection zone is very complex, because the turbulent convective motions carry a significant amount of the total heat flux. This can be modeled also here by expressing the small-scale correlation properties with mean-field quantities (see e.g. Rüdiger, 1989). The mean convective heat flux reads

$$\mathcal{F}_{\rm conv} = \overline{(\rho \boldsymbol{u})' c_{\rm P} T'}, \tag{2.26}$$

where $(\rho \boldsymbol{u})'$ is fluctuating mass flux and T' the fluctuating temperature. With the help of mean-field calculations, one can derive the convective heat flux in terms of the mean entropy gradient, see Rüdiger (1989),

$$\mathcal{F}_{\rm conv} = -\chi_{\rm t} \overline{\rho}\,\overline{T} \boldsymbol{\nabla} \overline{s}, \tag{2.27}$$

where $\chi_{\rm t}$ is the turbulent heat diffusivity, which can be expressed in terms of the mixing length l

$$\chi_{\rm t} = \tfrac{1}{3} u_{\rm rms} l \tag{2.28}$$

or using the pressure scale height H_P

$$\chi_{\rm t} = \tfrac{1}{3} \alpha_{\rm MLT} u_{\rm rms} H_P. \tag{2.29}$$

The turbulent heat diffusivity is generally speaking not a scalar as in Eq. (2.27), but a tensor

$$\mathcal{F}_i = -\chi_{ij} \overline{\rho}\,\overline{T} \partial_j \overline{s}. \tag{2.30}$$

If the heat fluxes and the entropy gradients are known, we can calculate the turbulent heat diffusivities accordingly. A good approximation for the convective heat flux is $|\mathcal{F}_{\rm conv}| \approx \rho u_{\rm rms}^3$, which was already pointed out by Vitense (1953).

2.3 Rotation

The Sun has a mean rotation period of around $T_{\rm rot} = 27.3\,\text{days}$. Compared with other stars, the Sun is considered a slow rotator. The solar rotation can be quantified in terms of the non-dimensional Coriolis number,

$$\mathrm{Co} = \frac{\|2\boldsymbol{\Omega}_0 \times \boldsymbol{u}\|}{\|(\boldsymbol{u}\cdot\boldsymbol{\nabla})\,\boldsymbol{u}\|} \approx \frac{2\Omega_0}{u_{\rm rms} k_{\rm f}}, \tag{2.31}$$

where $k_{\rm f}$ is the wavenumber of the inverse length scale of the system and $\boldsymbol{\Omega}_0 = \Omega_0(\cos\theta, -\sin\theta, 0)$ is the rotations vector with Ω_0 the rotation rate of the solar interior (without the convection zone), for which we can assume a solid body rotation. For the case of the Sun, the rotation frequency is $f = 1/T_{\rm rot} = \Omega_0/2\pi \approx 425\,\text{nHz}$. The Coriolis number gives the strength of rotation compared with the turbulent motions. For the solar convection zone we often choose (as in e.g. Käpylä et al., 2010, as well as **Papers IV–VI**)

$$k_{\rm f} = \frac{21}{R_\odot} \approx \frac{2\pi}{d}, \tag{2.32}$$

where $d = 0.3\,R_\odot$ is the thickness of the convection zone and $R_\odot \approx 700\,\text{Mm}$ the solar radius. In the literature the Rossby number Ro is often used instead of the Coriolis number (following Stix, 2002)

$$\mathrm{Ro} = \frac{u_{\rm rms}}{2\Omega_0 l} \quad \Rightarrow \quad \mathrm{Co} = \frac{2\pi}{\mathrm{Ro}}, \tag{2.33}$$

where $l = 2\pi/k_{\rm f}$. Hence, the Rossby number is the same as the inverse Coriolis number except a factor of 2π. The Coriolis number of the Sun is around 6, when averaged over the convection zone. If we instead take a height dependent rotation profile and a height dependent rms velocity, the Coriolis number shows also a strong height dependence. At the bottom of the convection zone the Coriolis number is around $\mathrm{Co} \approx 60$, while near the surface $\mathrm{Co} \approx 0.06$ (Stix, 2002).

As shown in Fig. 1.2, the Sun rotates in the convection zone non-cylindrically, which is unexpected. Let us consider the simplest case. We have a sphere of fluid rotating about an axis. If there is no turbulence or other forces, the sphere rotates as a solid body. This means, Ω is constant and the rotation speed $u_\phi = \Omega\varpi = \Omega r\sin\theta$ increases linearly with distance from the rotation axis $\varpi = r\sin\theta$. The situation changes, if we consider pressure gradient and gravity acting on the fluid. When the turbulent motions are weak compared with rotation speed ($\mathrm{Co} \gg 1$), the Coriolis force balances with the pressure and the gravity. Then, the *Taylor-Proudman theorem* states, that the contours of constant rotation rate are parallel to the rotation axis; i.e. the local velocity of

the fluid is constant along cylindrical surfaces, if the density is constant. In **Paper IV** and **VI**, the differential rotation is constant along cylindrical surfaces, because of the strong rotation rate as implied by the Taylor-Proudman theorem. The Sun is slightly above this limit (Co ≈ 6), and the additional forces acting on the plasma are more important in the convection zone (Kippenhahn, 1963). There, anisotropic turbulent motions and turbulent heat fluxes generated by the convection resulting in a non-zero latitudinal temperature gradients break the Taylor-Proudman balance via the baroclinic term, see Eq. (2.37). In addition the magnetic field also influences the motion of the flow inside the convection zone, but we will introduce this in § 3. These forces are able to transform the rotation of a solid body to a differential rotation with radial contours of constant rotation. In **Paper V** we found a similar differential rotation profile, although the rotation rate is slightly higher (Co ≈ 8), but also there the turbulent stresses and the turbulent heat transport form this rotation profile via the baroclinic term. On the other hand the rotation will influence the convective motions due to the Coriolis and centrifugal forces. The rotation has yet another effect on the fluid motions. It generates a mean flow in the meridional plane, which points polewards at the surface and equatorwards below the surface. This flow is called the *meridional circulation*. It is known since long time, that a slow rotating body as the Sun should have a so-called *Eddington–Sweet circulation* to fulfill conservation of energy (see e.g. Kippenhahn and Weigert, 1990). The meridional circulation can be interpreted as a type of Eddington–Sweet circulation, and it is caused by the inclination of the isobaric relative to the isopycnic surfaces. Isobaric and isopycnic surfaces are the surfaces, where the pressure and the density are constant, respectively. But for the Sun, the time-scale of the Eddington–Sweet circulation is longer than its lifetime.

2.4 Mean-field models of solar differential rotation

The main mechanism causing the differential rotation is the anisotropy of the convective motions (see e.g. Kippenhahn, 1963; Tuominen and Rüdiger, 1989). The Sun is approximately axially symmetric. Therefore we can define mean quantities by averaging over the azimuthal direction ϕ. To investigate this, we look at the conservation of mean angular momentum in spherical coordinates.

$$\frac{\partial \left(\overline{\rho}\,\overline{\Omega} r^2 \sin^2\theta\right)}{\partial t} + \boldsymbol{\nabla}\cdot\left[\overline{\rho} r \sin\theta \left(\overline{\boldsymbol{u}}\,\overline{u}_\phi + \overline{\boldsymbol{u}' u'_\phi}\right)\right] = 0, \tag{2.34}$$

where $\overline{\Omega} = \overline{u}_\phi / r\sin\theta$ is the local rotation rate, $\overline{\boldsymbol{u}' u'_\phi}$ is part of the Reynolds stress tensor $\mathbf{Q}$ introduced in Eq. (2.22). Note that we neglect here the magnetic parametrization of the angular momentum transport. First order smoothing

calculations reveal an extra term in the components of the Reynolds stress tensor, which is related to the mean rotation

$$Q_{ij} = \Lambda_{ijk}\overline{\Omega}_k - \mathfrak{N}_{ijkl}\overline{u}_{k;l}, \tag{2.35}$$

where the semicolons denote the co-variant derivatives. Comparing Eq. (2.35) with Eq. (2.22), we find that the isotropic part of the turbulent viscosity tensor $\mathfrak{N}_{ijkl}$ can be associated with the turbulent viscosity ν_t. The Λ_{ijk} describes the so-called Λ-effect. Using the right parameter for Λ_{ijk} and $\mathfrak{N}_{ijkl}$, it is possible to model the differential rotation of the Sun (see e.g. Tuominen and Rüdiger, 1989; Brandenburg et al., 1992; Kitchatinov and Rüdiger, 1995; Kitchatinov and Rüdiger, 2005).

Differential rotation can be obtained by solving Eq. (2.34) alone while ignoring the meridional circulation. But it will be insufficient, if the rotation period becomes shorter than the time scale of the turbulent viscosity. This is expressed with the Taylor number

$$\mathrm{Ta} = \left(2\Omega_0 R_\odot^2/\nu_\mathrm{t}\right)^2. \tag{2.36}$$

For the Sun the Taylor number is around $\mathrm{Ta} \approx 3\times10^7$ (Rüdiger, 1989). The meridional circulation depends on the rotation rate. For low Ta the meridional flow increases with increasing Ta, until it reaches $\mathrm{Ta} \approx 3\times10^5$, then it decreases with increasing Ta; for a rotation rate equal or larger than that of the Sun, the meridional circulation is suppressed by the rotation (Köhler, 1970). This can also be seen from the evolution equation of the mean azimuthal vorticity, which can be derived by taking the curl of ($\boldsymbol{\nabla}\times$) Eq. (2.21) (e.g. Küker and Stix, 2001)

$$\frac{\partial\overline{\omega}_\phi}{\partial t} = r\sin\theta\frac{\partial\overline{\Omega}^2}{\partial z} - \left[\boldsymbol{\nabla}\times\frac{1}{\overline{\rho}}\boldsymbol{\nabla}\left(\overline{\rho}\mathfrak{Q}\right)\right]_\phi + \left(\overline{\boldsymbol{\nabla}T\times\boldsymbol{\nabla}s}\right)_\phi, \tag{2.37}$$

where $\frac{\partial}{\partial z} = \cos\theta\,\frac{\partial}{\partial r} - \frac{1}{r}\sin\theta\,\frac{\partial}{\partial\theta}$ is the derivative along the rotation axis. We neglect here again the Maxwell stresses $\mathfrak{M}$, which can be added by replacing $\overline{\rho}\mathfrak{Q} \Rightarrow \overline{\rho}\mathfrak{Q} + \mathfrak{M}$. The three terms on the right hand side give rise to three different mechanisms to produce meridional circulation. The first is due to the differential rotation, the second due to Reynolds stresses. The third term is the baroclinic term and is probably the most important one for the meridional circulations (Rüdiger, 1989; Kitchatinov and Rüdiger, 2005). As can be seen from Eq. (2.37), baroclinicity is defined as the misalignment of the gradient of temperature and entropy, which gives a contribution to the vorticity evolution. The baroclinic term has two contributions: $\left(\overline{\boldsymbol{\nabla}T\times\boldsymbol{\nabla}s}\right)_\phi = \overline{\partial_r T\,\partial_\theta s} - \overline{\partial_\theta T\,\partial_r s}$.

Radial and latitudinal entropy gradients are comparable, but because the latitudinal temperature gradient is usually much smaller than the radial temperature gradient, the baroclinic term is a manifestation of the result of a latitudinal entropy difference. This implies that the poles are hotter than the equator. Mean-fields models show that just a few Kelvin difference between poles and equator can cause a solar-like meridional circulation (Rüdiger, 1989). In simulations, it frequently turns out that the influence of the Reynolds stresses can be neglected. Assuming now a constant meridional flow, the left hand side of Eq. (2.37) is zero and the two remaining terms on the right hand side must balance. The term $r\sin\theta\frac{\partial\overline{\Omega}^2}{\partial z}$ indicates, to which degree the differential rotation is cylindrical or non-cylindrical. For a cylindrical rotation the term is zero, for differential non-zero. This means that a dominant baroclinic term can reshape the cylindrical differential rotation caused by anisotropic Reynolds stresses to a non-cylindrical one. In **Paper VI** we have used this equation to conclude that the solar-like radial contours of constant rotation are shaped by the a non-zero latitudinal entropy gradient.

3. Magnetohydrodynamics

From a long view of history—seen from, say,
ten thousand years from now—there can be little doubt
that the most significant event of the 19th century will be judged
as Maxwell's discovery of the laws of electrodynamics.

Richard Feynman

For many astrophysical objects magnetic fields are essential. Magnetic fields have a strong influence in the star formation processes occurring in a collapsing nebula. Magnetic fields cause a planetary disk to become turbulent without which planet formation may be impossible. Magnetic fields give stars as our Sun an activity cycle that has a strong impact on the surrounding planets via eruptive events.

3.1 Magnetohydrodynamical equations

In general, the evolution of magnetic fields $\boldsymbol{B}$ and electric fields $\boldsymbol{E}$ are described by the Maxwell equations (Maxwell, 1865)

$$\boldsymbol{\nabla} \cdot \boldsymbol{E} = \frac{\rho_e}{\varepsilon_0} \qquad \text{[Gauss' law]}, \tag{3.1}$$

$$\boldsymbol{\nabla} \cdot \boldsymbol{B} = 0 \qquad \text{[no magnetic monopoles]}, \tag{3.2}$$

$$\boldsymbol{\nabla} \times \boldsymbol{E} = -\frac{\partial \boldsymbol{B}}{\partial t} \qquad \text{[Faraday's law]}, \tag{3.3}$$

$$\boldsymbol{\nabla} \times \boldsymbol{B} = \mu_o \boldsymbol{J} + \mu_o \varepsilon_o \frac{\partial \boldsymbol{E}}{\partial t} \qquad \text{[Ampere's and Maxwell's law]}, \tag{3.4}$$

where ρ_e is the charge density, ε_0 the vacuum permittivity and μ_0 the vacuum permeability. The speed of light is defined via $c = 1/\sqrt{\varepsilon_0 \mu_0}$. To describe magnetic fields in astrophysical objects, we combine the Maxwell equations with the equations of the fluid dynamics introduced in § 2.1.2. To simplify we assume non-relativistic velocities, no electromagnetic waves and high conductivity. Additionally we use Ohm's law and in doing so transform the magnetic and electric fields into the co-moving frame of the fluid. With these conditions, we can derive the evolution equation for the magnetic field, the **induction equation**

$$\frac{\partial \boldsymbol{B}}{\partial t} = \boldsymbol{\nabla} \times (\boldsymbol{u} \times \boldsymbol{B}) - \boldsymbol{\nabla} \times (\eta \boldsymbol{\nabla} \times \boldsymbol{B}), \tag{3.5}$$

where $\eta = 1/\mu_0\sigma$ is the magnetic diffusivity and σ the conductivity. The current density is given by

$$\boldsymbol{J} = \frac{1}{\mu_0}\boldsymbol{\nabla}\times\boldsymbol{B}. \tag{3.6}$$

To form a complete set of equations in magnetohydrodynamics (MHD), we combine the equation above with the **Navier–Stokes equation** (2.12) including the Lorentz force $\boldsymbol{F}_{\rm L} = \boldsymbol{J}\times\boldsymbol{B}$,

$$\frac{\partial \boldsymbol{u}}{\partial t} = -(\boldsymbol{u}\cdot\boldsymbol{\nabla})\boldsymbol{u} + \boldsymbol{g} + \frac{1}{\rho}(\boldsymbol{J}\times\boldsymbol{B} - \boldsymbol{\nabla}p + \boldsymbol{\nabla}\cdot 2\nu\rho\mathsf{S} + \boldsymbol{F}) \tag{3.7}$$

and the **continuity equation** as in Eq. (2.10)

$$\frac{{\rm D}\ln\rho}{{\rm D}t} = -\boldsymbol{\nabla}\cdot\boldsymbol{u}. \tag{3.8}$$

Usually we also include an **energy equation**. Here we take one in the form of the evolution equation of the specific entropy

$$T\frac{{\rm D}s}{{\rm D}t} = \frac{1}{\rho}\boldsymbol{\nabla}\cdot K\boldsymbol{\nabla}T + 2\nu\mathsf{S}^2 + \frac{\mu_0\eta}{\rho}\boldsymbol{J}^2, \tag{3.9}$$

where K is the heat conductivity, $2\nu\mathsf{S}^2$ is the viscous heating and $\frac{\mu_0\eta}{\rho}\boldsymbol{J}^2$ is the Joule or Ohmic heating. We use these equations with the assumption of a perfect gas obeying the **equation of state**

$$p = \frac{1}{\gamma}c_{\rm s}^2\rho, \quad \text{with} \quad c_{\rm s}^2 = \frac{1}{c_{\rm P}}(\gamma-1)T, \tag{3.10}$$

where $c_{\rm s}$ is the speed of sound. The Eqs. (3.5)–(3.10) form a complete set of MHD equations.

In the induction equation, we have, similar to Eq. (2.12), an advection and a diffusion term. Here, we can also define a non-dimensional number to describe the relation of these two terms. Because of the similarity to the Reynolds number, we call it the magnetic Reynolds number, which is defined as

$${\rm Re}_{\rm M} \equiv \frac{\|\boldsymbol{\nabla}\times(\boldsymbol{u}\times\boldsymbol{B})\|}{\|\boldsymbol{\nabla}\times(\eta\boldsymbol{\nabla}\times\boldsymbol{B})\|} \approx \frac{UL}{\eta}, \tag{3.11}$$

where we used dimensional arguments. U is the typical velocity of the system, and L the typical length scale. For magnetic Reynolds numbers in the order of unity or smaller the diffusion dominates and the magnetic field decays via Ohmic heating, for magnetic Reynolds numbers much higher than the unity magnetic field can be amplified. In the simulations of **Papers I–VI**, we use for the magnetic Reynolds number the definition ${\rm Re}_{\rm M} = u_{\rm rms}k_{\rm f}/\eta$. Also here, the ratio of the two terms might give a different value than the ${\rm Re}_{\rm M}$ defined above. Before discussing the mechanism of amplifying magnetic fields, we discuss briefly two important applications of the MHD equations.

3.1.1 Alfvén's theorem

When the conductivity σ is high enough, the field is frozen into the fluid. If we consider a bundle of parallel magnetic field lines in a fluid, there exists a well defined magnetic flux through the cross section of the bundle. During the motions of the fluid, the magnetic flux can change in two different ways. A change in the magnetic field can change the magnetic flux and a change in the cross section can change the flux as well. Adding now these two contributions, one can show that the total change of the flux $\mathrm{d}\Phi/\mathrm{d}t$ only depends on the current density $\boldsymbol{J}$ and the conductivity σ (see e.g. Stix, 2002, for a more detailed calculation)

$$\frac{\mathrm{d}\Phi}{\mathrm{d}t} = -\oint_C \frac{\boldsymbol{J}}{\sigma} \cdot \mathrm{d}\boldsymbol{l}, \tag{3.12}$$

where C is boundary of the cross section, $\mathrm{d}\boldsymbol{l}$ is the line element along the boundary. In the limit of $\sigma \to \infty$, the magnetic flux is constant. This theorem can be successfully applied in the solar convection zone and solar corona, where the high temperatures lead to high conductivities. There the flow and the magnetic fields are strongly tied to each other. The plasma-β parameter ($\beta = \frac{2\mu_0 p}{B^2}$) describes, whether the magnetic field or the fluid motion are dominating the other. In the convection zone, the plasma-β is mostly larger than unity and the fluid motion can generate magnetic fields due to this effect. In the corona, the plasma-β is mostly smaller than unity and plasma flows along the magnetic field lines forming coronal loops and prominences. In sunspots, magnetic fields are strong and plasma-β is smaller than unity. This suppresses the fluid motion inside the umbral region and quench the convective heat transport, leading to a dark spot.

3.1.2 Force-free fields

For the solar corona it is common to approximate the magnetic fields by force-free fields. In general, this means that the Lorentz force is zero, which can be achieved by (except the trivial solution $\boldsymbol{B} = \boldsymbol{0}$)

$$\frac{1}{\mu_0} \boldsymbol{\nabla} \times \boldsymbol{B} = \boldsymbol{J} = \alpha_{\mathrm{ff}} \boldsymbol{B}, \tag{3.13}$$

where α_{ff} is a force-free parameter. When $\alpha_{\mathrm{ff}} = 0$, then $\boldsymbol{J} = 0$ and the magnetic field is a potential field $\boldsymbol{B} = \boldsymbol{\nabla}\Phi_{\mathrm{m}}$ with no currents (Schmidt, 1964; Semel and Rayrole, 1968). It can be calculated by solving the Poisson equation for the magnetic potential $\Delta\Phi_{\mathrm{m}} = 0$. A more advanced method consist in using a non-zero α_{ff}. There, the currents $\boldsymbol{J}$ are (anti-)parallel to the magnetic fields $\boldsymbol{B}$. In **Paper I** we have calculated the angle between $\boldsymbol{J}$ and $\boldsymbol{B}$ for one of the simulations, which can give insights about α_{ff}, and we find that in the outer layers

of our domain, which correspond to solar corona, the magnetic field is indeed force-free. Similar calculations have been done for more realistic models of the solar corona (Gudiksen and Nordlund, 2005a,b; Bingert and Peter, 2011), where the authors found also force-free fields in their simulated coronae. For describing the magnetic fields inside the corona, force-free extrapolation techniques are commonly used. One possibility is to use magnetograms obtained from high resolution observations of the photosphere and to extrapolate the magnetic field into upper atmospheric regions. There are two extrapolation methods, one is the linear force-free extrapolation, where $\alpha_{\rm ff} = \text{const}$ (Nakagawa and Raadu, 1972; Alissandrakis, 1981; Gary, 1989), the other one is the non-linear force-free extrapolation, where $\alpha_{\rm ff}$ is constant along a field line (Woltjer, 1958; Sakurai, 1981; Wiegelmann, 2004). A more detailed discussion of different methods of force-free extrapolation can be found in Wiegelmann (2008). Neither of these methods work very well. One reason is the chromosphere, which the field has to pass through.

3.1.3 Magnetic buoyancy

In § 2 we have already discussed the buoyancy of fluid elements due to different temperature gradients. Magnetic fields can also lead to buoyancy of fluid elements, this is called magnetic buoyancy. The Lorentz force in Eq. (3.7) can be decomposed into two contributions:

$$\boldsymbol{J} \times \boldsymbol{B} = \frac{1}{\mu_0} (\boldsymbol{B} \cdot \boldsymbol{\nabla}) \boldsymbol{B} - \frac{\boldsymbol{\nabla} \left(\boldsymbol{B}^2 \right)}{2\mu_0}, \tag{3.14}$$

where the first term is the magnetic tension along field lines and the second term is the gradient of the magnetic pressure or magnetic energy density $\frac{\boldsymbol{B}^2}{2\mu_0}$. In Eq. (3.7) the magnetic pressure can then be combined with the gas pressure forming a total pressure

$$p_{\rm tot} = p + \frac{\boldsymbol{B}^2}{2\mu_0}. \tag{3.15}$$

If we consider a magnetic flux tube structure in non-magnetic surroundings. In magnetic flux tubes, magnetic field lines are confined to the tube. Then the magnetic field inside the tube leads to enhanced pressure. The pressure will balance in a short time compared to the diffusion time and causes an expansion of the tube. Because the mass inside the tube will not change, the expansion is accompanied by a decrease of density. A density difference with the surrounding medium leads to the buoyancy of the tube. Magnetic buoyancy is believed to be one of the key mechanism that makes magnetic flux tubes rise from the bottom of convection zone to the surface and form bipolar regions.

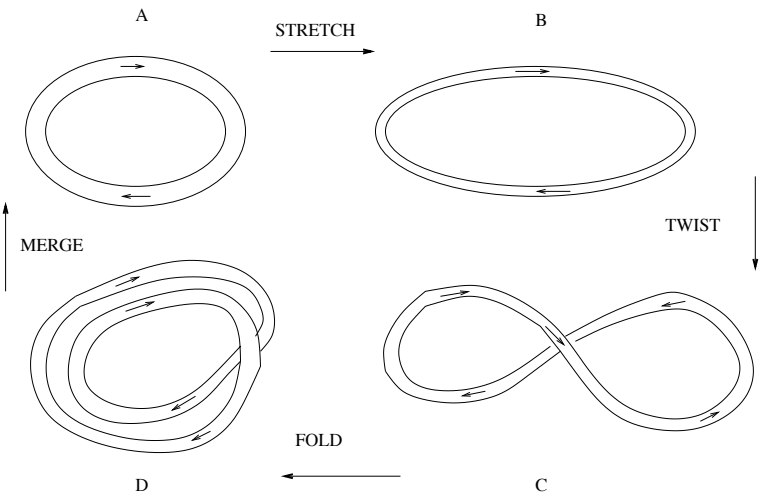

Figure 3.1: A schematic illustration of the stretch-twist-fold-merge dynamo mechanism. Taken from Brandenburg and Subramanian (2005).

3.2 Generation of magnetic fields

We know that the Earth, other planets, the Sun and other stars have magnetic fields. But where do they come from? We could imagine that weak magnetic fields already existed in the interstellar clouds, out of which stars and planets have been formed. In the phase of contraction, also the magnetic fields were concentrated inside the star and this leads to the existence of strong magnetic fields. This is certainly true, but this mechanism alone is not enough to explain the behavior of magnetic fields we observe today. The magnetic field for example of the Earth would have decayed by diffusion away already, if there would not have been a mechanism to regenerate magnetic fields. The fields of the Earth and of the Sun show also another crucial behavior. They reverse and, in the case of the Sun, oscillate. The reversal interval of the Earth's magnetic field is random and shows a range of 0.1 to 50 million years. The magnetic field of the Sun has an averaged period of 22 years. Oscillatory and reversal magnetic field are unexplained by primordial field models; it can only be explained by a dynamo mechanism (Ossendrijver, 2003; Brandenburg and Subramanian, 2005; Charbonneau, 2010).

The dynamo mechanism is a type of instability, which transfers kinetic energy into magnetic energy. But a dynamo mechanism as an instability can never create magnetic fields, it can only amplify small magnetic fields to larger ones. The basic idea can be illustrated by the *stretch-twist-fold-merge-mechanism*, see Vainshtein and Zel'dovich (1972) and Fig. 3.1. Taking a closed flux

rope in a incompressible medium and expand it to twice its length (A⇒B). The volume of the rope will be preserved because of the incompressible surroundings. The magnetic field lines are frozen in, see § 3.1.1, and the cross section halves, therefore the magnetic field strength doubles. Now we twist the rope so that we get a figure as an eight (B⇒C). Then we fold the two loops on top of each other (C⇒D). We have now two loops, where the magnetic field points in the same direction and each of them has a magnetic field strength as strong as the original rope. With the help of reconnection, we can merge the two ropes into one rope with the same volume as before, but with twice the magnetic field (D⇒A). To generate a larger magnetic field we use kinetic energy to stretch, twist and fold the rope and a small amount of diffusivity to merge the loops This mechanism illustrates quite well the basic idea of a dynamo operating in the Sun or inside the Earth. In reality it would be hard to imagine a flow, which can reproduce the same deformations as described above. We will discuss now two of the important dynamo mechanisms generating magnetic fields; the first one is the so-called α^2-dynamo and the second one the so-called α-Ω-dynamo.

3.2.1 α^2-dynamo

From direct numerical simulations, we know that turbulence can amplify magnetic fields (see e.g. Brandenburg and Subramanian, 2005). We saw in § 2.2 that mean-field models are a powerful tool to describing turbulence and its influence on physical quantities. To describe turbulent dynamos, we use a mean-field approach. As a first step, we write the mean induction equation, (compare with Eq. (3.5) and see Krause and Rädler, 1980)

$$\frac{\partial \overline{\boldsymbol{B}}}{\partial t} = \boldsymbol{\nabla} \times \left(\overline{\boldsymbol{u}} \times \overline{\boldsymbol{B}}\right) + \boldsymbol{\nabla} \times \left(\overline{\boldsymbol{u}' \times \boldsymbol{B}'}\right) - \boldsymbol{\nabla} \times \left(\eta \boldsymbol{\nabla} \times \overline{\boldsymbol{B}}\right), \tag{3.16}$$

where primes indicate fluctuating quantities and bars mean quantities. The averaging reveals a new term $\boldsymbol{\nabla} \times \left(\overline{\boldsymbol{u}' \times \boldsymbol{B}'}\right)$, which is the correlation of the fluctuating velocity field and the fluctuating magnetic field. This term can be responsible for generating a magnetic field and is called mean electromotive force $\overline{\boldsymbol{\mathcal{E}}} = \overline{\boldsymbol{u}' \times \boldsymbol{B}'}$. Following the mean-field approach, we can express this quantity which rise from the fluctuations, in terms of mean quantities

$$\overline{\boldsymbol{\mathcal{E}}} = \overline{\boldsymbol{u}' \times \boldsymbol{B}'} = \alpha \overline{\boldsymbol{B}} - \eta_\mathrm{t} \boldsymbol{\nabla} \times \overline{\boldsymbol{B}}, \tag{3.17}$$

where α and the turbulent diffusivity η_t are in general tensors. Inserting it into Eq. (3.16) and assuming a turbulent flow without any mean velocity ($\overline{\boldsymbol{u}} = \boldsymbol{0}$), we obtain

$$\frac{\partial \overline{\boldsymbol{B}}}{\partial t} = \boldsymbol{\nabla} \times \left(\alpha \overline{\boldsymbol{B}}\right) - \boldsymbol{\nabla} \times \left(\eta_\mathrm{T} \boldsymbol{\nabla} \times \overline{\boldsymbol{B}}\right), \tag{3.18}$$

where we add the two diffusivities to a total diffusivity $\eta_\mathrm{T} = \eta_\mathrm{t} + \eta$. The turbulent diffusivity η_t in general increases the diffusion of the magnetic field and hence cannot contribute to a dynamo effect, but there can also be exceptions (see e.g. Devlen et al., 2012, where a case with $\eta_\mathrm{T} < 0$ was found). With a zero mean velocity field, the term $\boldsymbol{\nabla} \times \left(\alpha \overline{\boldsymbol{B}}\right)$, called the α-effect, is the only effect capable of amplifying a magnetic field (Steenbeck et al., 1966). For homogeneous and isotropic turbulence, α can be expressed by (see e.g. Pouquet et al., 1976)

$$\alpha = -\frac{1}{3}\tau_\mathrm{c}\overline{\boldsymbol{\omega}' \cdot \boldsymbol{u}'} + \frac{1}{3}\frac{\tau_\mathrm{c}}{\overline{\rho}}\overline{\boldsymbol{J}' \cdot \boldsymbol{B}'} = \alpha_\mathrm{K} + \alpha_\mathrm{M}, \tag{3.19}$$

where τ_c is the turbulent correlation time, $\boldsymbol{\omega}' = \boldsymbol{\nabla} \times \boldsymbol{u}'$ is the fluctuating vorticity. α_K is the kinetic, and α_M the magnetic part of α, which can provide an important feedback of the mean magnetic field on α. If α and η_T are constant in space, we can move them in front of the derivatives. If we additionally assume axisymmetry in spherical coordinates along the ϖ-axis ($\varpi = r\sin\theta$, $\frac{\partial}{\partial\phi} = 0$), we can divide the mean magnetic field in a poloidal and toroidal part $\overline{\boldsymbol{B}} = \overline{\boldsymbol{B}}_\mathrm{pol} + \overline{\boldsymbol{B}}_\mathrm{tor}$ with $\overline{\boldsymbol{B}}_\mathrm{pol} = \left(\overline{B}_r, \overline{B}_\theta, 0\right)$ and $\overline{\boldsymbol{B}}_\mathrm{tor} = \left(0, 0, \overline{B}_\phi\right)$. Then we can decompose the mean-field induction equation in two separate equations:

$$\frac{\partial \overline{\boldsymbol{B}}_\mathrm{pol}}{\partial t} = \alpha \boldsymbol{\nabla} \times \overline{\boldsymbol{B}}_\mathrm{tor} + \eta_\mathrm{T} \Delta \overline{\boldsymbol{B}}_\mathrm{pol} \tag{3.20}$$

$$\frac{\partial \overline{\boldsymbol{B}}_\mathrm{tor}}{\partial t} = \alpha \boldsymbol{\nabla} \times \overline{\boldsymbol{B}}_\mathrm{pol} + \eta_\mathrm{T} \Delta \overline{\boldsymbol{B}}_\mathrm{tor}, \tag{3.21}$$

where we have used Eq. (3.3). Here we can see, why this dynamo is called α^2-dynamo. The toroidal field gets amplified by the α-effect from the poloidal field and the poloidal field gets amplified by the α-effect from the toroidal field.

3.2.2 α–Ω-dynamo

Now we consider an additional mean flow, and Eq. (3.18) will change to

$$\frac{\partial \overline{\boldsymbol{B}}}{\partial t} = \boldsymbol{\nabla} \times \left(\overline{\boldsymbol{u}} \times \overline{\boldsymbol{B}}\right) + \boldsymbol{\nabla} \times \left(\alpha \overline{\boldsymbol{B}}\right) - \boldsymbol{\nabla} \times \left(\eta_\mathrm{T} \boldsymbol{\nabla} \times \overline{\boldsymbol{B}}\right). \tag{3.22}$$

Applying now a mean flow $\overline{\boldsymbol{u}} = \overline{\boldsymbol{u}}_\mathrm{tor} = (0, 0, \Omega\varpi)$, which corresponds to a rotation with angular velocity Ω and using similar assumptions as above, we can also write two separate equations

$$\frac{\partial \overline{\boldsymbol{B}}_\mathrm{pol}}{\partial t} = \alpha \boldsymbol{\nabla} \times \overline{\boldsymbol{B}}_\mathrm{tor} + \eta_\mathrm{T} \Delta \overline{\boldsymbol{B}}_\mathrm{pol} \tag{3.23}$$

$$\frac{\partial \overline{\boldsymbol{B}}_\mathrm{tor}}{\partial t} = \boldsymbol{\nabla} \times \left(\overline{\boldsymbol{u}}_\mathrm{tor} \times \overline{\boldsymbol{B}}_\mathrm{pol}\right) + \alpha \boldsymbol{\nabla} \times \overline{\boldsymbol{B}}_\mathrm{pol} + \eta_\mathrm{T} \Delta \overline{\boldsymbol{B}}_\mathrm{tor}, \tag{3.24}$$

Now, we see that, because of the mean flow in terms of a rotation, the toroidal field gets amplified additionally by a term related to the mean velocity. This kind of dynamo is called α–Ω-dynamo, because the mean velocity is related to the differential rotation. Precisely speaking, this dynamo is called α^2–Ω-dynamo, but since the α-effect generating the toroidal field is typically weaker than the Ω-effect, it can be neglected.

3.3 Magnetic helicity

Magnetic helicity is an important quantity in astrophysics. Not only does it indicate the twist of magnetic fields, it is conserved on a resistive timescale. Magnetic helicity is defined as

$$H = \int_V \boldsymbol{A} \cdot \boldsymbol{B} \, \mathrm{d}V, \tag{3.25}$$

where $\boldsymbol{A}$ is the magnetic vector potential and related via $\boldsymbol{B} = \boldsymbol{\nabla} \times \boldsymbol{A}$ with the magnetic field. The magnetic helicity is in general gauge dependent, but choosing a infinite volume V one can make it independent. Normally, we are using the magnetic helicity density $h = \boldsymbol{A} \cdot \boldsymbol{B}$, which is always gauge dependent. In the following we will apply the Weyl gauge, which satisfies

$$\frac{\partial \boldsymbol{A}}{\partial t} = \boldsymbol{u} \times \boldsymbol{B} - \mu_0 \eta \boldsymbol{J} \tag{3.26}$$

The evolution equation for the magnetic helicity is then given by

$$\frac{\partial}{\partial t} \int_V \boldsymbol{A} \cdot \boldsymbol{B} \, \mathrm{d}V = -2 \int_V \mu_0 \eta \boldsymbol{J} \cdot \boldsymbol{B} \, \mathrm{d}V - \int_V \boldsymbol{\nabla} \cdot \boldsymbol{\mathcal{F}}_h \, \mathrm{d}V, \tag{3.27}$$

where $\boldsymbol{\mathcal{F}}_h$ are the helicity fluxes and we have used Eqs. (3.5) and (3.26). If we assume zero fluxes and look at the limit, when the conductivity is going to infinity ($\eta \Rightarrow 0$), then the right hand side of Eq. (3.27) vanishes and magnetic helicity is conserved. With the exception of the flux term $\boldsymbol{\nabla} \cdot \boldsymbol{\mathcal{F}}_h$, the velocity does not enter, so magnetic helicity is not affected by turbulence diffusion. In the convection zone and the solar corona, the conductivity is high enough to conserve magnetic helicity to a first order, but there, also magnetic helicity fluxes will play an important role.

3.3.1 Catastrophic quenching of the α–effect and magnetic helicity fluxes

One might ask, why does the magnetic helicity have some relation with the α–effect? First of all, α consist of two parts: α_K and α_M (Pouquet et al.,

1976). $\alpha_{\rm K}$ describes the magnetic field amplification in the kinematic regime, i.e. when the magnetic field is weak and does not react back on the flow. In this stage, $\alpha_{\rm M}$ is much smaller than $\alpha_{\rm K}$ and can be neglected. For larger magnetic fields, $\alpha_{\rm M}$ becomes much stronger and contributes with an opposite sign to α. We know from numerical simulations of homogeneous and isotropic turbulence (see e.g. Brandenburg and Subramanian, 2005) that the magnetic field grows first exponentially, which is consistent with linear stability analysis, and then saturates, when the field has become sufficiently strong. Usually, $\overline{\boldsymbol{\omega}'\cdot\boldsymbol{u}'}$ and $\overline{\boldsymbol{J}'\cdot\boldsymbol{B}'}$ have the same sign, let us assume the positive. As we see from Eq. (3.19), $\alpha_{\rm M}$ enters with a plus sign and can balance with the negative $\alpha_{\rm K}$, if the field is strong enough. For helical magnetic fields, $\alpha_{\rm M}$ can be related to the mean magnetic helicity of the fluctuating fields

$$\alpha_{\rm M} = \frac{1}{3}\frac{\tau_{\rm c}}{\overline{\rho}}\overline{\boldsymbol{J}'\cdot\boldsymbol{B}'} \approx \frac{k_f^2}{3}\frac{\tau_{\rm c}}{\overline{\rho}}\overline{\boldsymbol{A}'\cdot\boldsymbol{B}'}, \tag{3.28}$$

where k_f is the typical wavenumber of the fluctuations. Now let us look at the evolution of the mean magnetic helicity. We first consider the mean magnetic helicity of the total field $\overline{h} = \overline{\boldsymbol{A}\cdot\boldsymbol{B}}$, where the evolution equation is given by taking the mean of every term of Eq. (3.27)

$$\frac{\partial}{\partial t}\overline{h} = \frac{\partial}{\partial t}\overline{\boldsymbol{A}\cdot\boldsymbol{B}} = -2\mu_0\eta\overline{\boldsymbol{J}\cdot\boldsymbol{B}} - \boldsymbol{\nabla}\cdot\overline{\boldsymbol{\mathcal{F}}}_h. \tag{3.29}$$

The mean magnetic helicity $\overline{h}$ has two contributions: one from the mean-fields $\overline{h}_m = \overline{\boldsymbol{A}}\cdot\overline{\boldsymbol{B}}$ and one from the fluctuating fields $\overline{h}_f = \overline{\boldsymbol{A}'\cdot\boldsymbol{B}'}$. In their evolution equations, an additional term appears arising from the electromotive force $\overline{\boldsymbol{\mathcal{E}}} = \overline{\boldsymbol{u}'\times\boldsymbol{B}'}$, see Eq. (3.17),

$$\frac{\partial}{\partial t}\overline{h}_m = \frac{\partial}{\partial t}\overline{\boldsymbol{A}}\cdot\overline{\boldsymbol{B}} = \quad 2\overline{\boldsymbol{u}'\times\boldsymbol{B}'}\cdot\overline{\boldsymbol{B}} - 2\mu_0\eta\overline{\boldsymbol{J}}\cdot\overline{\boldsymbol{B}} \; - \boldsymbol{\nabla}\cdot\overline{\boldsymbol{\mathcal{F}}}_h^m, \tag{3.30}$$

$$\frac{\partial}{\partial t}\overline{h}_f = \frac{\partial}{\partial t}\overline{\boldsymbol{A}'\cdot\boldsymbol{B}'} = -2\overline{\boldsymbol{u}'\times\boldsymbol{B}'}\cdot\overline{\boldsymbol{B}} - 2\mu_0\eta\overline{\boldsymbol{J}'\cdot\boldsymbol{B}'} - \boldsymbol{\nabla}\cdot\overline{\boldsymbol{\mathcal{F}}}_h^f, \tag{3.31}$$

where $\overline{h} = \overline{h}_m + \overline{h}_f$ and $\overline{\boldsymbol{\mathcal{F}}}_h = \overline{\boldsymbol{\mathcal{F}}}_h^m + \overline{\boldsymbol{\mathcal{F}}}_h^f$. Using Eq. (3.28) together with the evolution of $\overline{h}_f$ from Eq. (3.31), we express the evolution of the magnetic $\alpha_{\rm M}$, see Kleeorin and Ruzmaikin (1982) by

$$\frac{\partial\alpha_{\rm M}}{\partial t} = -2\eta_t k_f^2\left(\frac{\overline{\boldsymbol{u}'\times\boldsymbol{B}'}\cdot\overline{\boldsymbol{B}}}{B_{\rm eq}^2} + \frac{\alpha_{\rm M}}{{\rm Re}_{\rm M}}\right) - \boldsymbol{\nabla}\cdot\overline{\boldsymbol{\mathcal{F}}}_{\alpha_{\rm M}}, \tag{3.32}$$

where the mean flux of $\alpha_{\rm M}$ is related to the mean helicity flux of the fluctuating fields by

$$\overline{\boldsymbol{\mathcal{F}}}_{\alpha_{\rm M}} = \frac{\eta_t k_f^2}{B_{\rm eq}^2}\overline{\boldsymbol{\mathcal{F}}}_h^f, \tag{3.33}$$

where $B_{\rm eq}$ is the magnetic equipartition field strength, i.e. a magnetic field, whose energy is equal to kinetic energy. The expression (3.32) is also called the dynamical quenching formula and describes an important issue of the dynamo theory. For high magnetic Reynolds numbers $\mathrm{Re_M}$, the α-effect is *catastrophically* quenched (see e.g. Vainshtein and Cattaneo, 1992; Cattaneo and Hughes, 1996; Brandenburg and Dobler, 2001). This can be seen by setting the left-hand side of Eq. (3.32) to zero and using $\alpha_{\rm M} = \alpha - \alpha_K$

$$\alpha = \frac{\alpha_{\rm K} + \mathrm{Re_M}\left(\eta_{\rm t}\overline{\boldsymbol{J}}\cdot\overline{\boldsymbol{B}} - \frac{1}{2}\boldsymbol{\nabla}\cdot\overline{\boldsymbol{\mathcal{F}}}_h^f\right)/B_{\rm eq}^2}{1 + \mathrm{Re_M}\overline{\boldsymbol{B}}^2/B_{\rm eq}^2} \tag{3.34}$$

For high magnetic Reynolds numbers and vanishing flux, the second term balances with $\alpha_{\rm K}$ to a zero α. However, it is important that the mean magnetic helicity flux also enters into this equation. If $\boldsymbol{\mathcal{F}}_h^f$ is negative and large enough it can suppress the quenching (Blackman and Field, 2000). It has been seen in several numerical simulations of dynamos (Brandenburg and Subramanian, 2005; Mitra et al., 2011; Del Sordo et al., 2013) that if one allows for magnetic helicity fluxes, the catastrophic quenching is suppressed. The behavior is one of the motivations for using a combined model of a convection zone and a corona as in **Papers I** to **V**. An open boundary of a dynamo domain allows magnetic helicity fluxes to escape and alleviates the catastrophic quenching at high Reynolds numbers.

4. Solar Dynamo Models

Die Zukunft wird nicht gemeistert von denen,
die am Vergangenen kleben.

Willy Brandt

In this chapter I will briefly discuss a few of the most important models for the solar dynamo. More detailed discussions of solar dynamo models can be found in reviews by Ossendrijver (2003), Brandenburg and Subramanian (2005), Charbonneau (2010), and Brandenburg et al. (2012) as well as in Stix (2002) and in Charbonneau (2013).

4.1 The challenge

Modeling the solar dynamo is challenging. Not only does there exist a large range of scales, over which a solar dynamo mechanism should operate, there is also a large amount of observed features which a solar dynamo model should reproduce. Let us start with the scales set by the solar environment. The density scale height varies from about tenths of Mm deep in convection zone to 150 km at the surface. The temperature spans from the bottom to the surface the range from two million Kelvin to six thousand Kelvin. The fluid and magnetic Reynolds numbers inside the Sun are high enough to allow for hydromagnetic turbulence (Frisch, 1995). Even developing a hydrodynamical model without any magnetic fields would be challenging as such, see § 2.2. But solving the MHD equations with realistic parameters and resolving the small as well as the large scales in one simulation is at the moment impossible; or more precisely, the computing power is not sufficient to simulate a realistic model even if we run it as long as the age of the universe. Even if we assume the doubling of computing power every two years (Moore's law), it would take over 100 years to have computer powerful enough to solve the solar dynamo realistically.

We have constraints from observations of magnetic fields on the surface and in the solar atmosphere, but unfortunately no information about the magnetic field inside the convection zone. The main properties, a solar dynamo should reproduce, can be divided into global and local phenomena. The global are: an eleven years activity cycle as a result of a 22 years magnetic cycle,

where every eleven years the field reverses; equatorward migration of radial and azimuthal magnetic fields being antisymmetric with respect to the equator, as well as a polar migration near the poles, as shown in Fig. 1.6. Additionally, global phenomena include a cyclic behavior with secondary cycles as the Gleissberg cycle and grand minima as the Maunder Minimum. As local phenomena, a solar dynamo model should reproduce flux concentrations in the range from sunspots and their groups to pores and plage fields. The magnetic orientation of the sunspots should be such that the leading and the following spots have the same polarity configuration in one hemisphere, but the opposite one in the other hemisphere. This configuration should remain for eleven years and reverse once every cycle (Hale's law). Further there should be a certain tilt angle of the line between two spots of a pair and the horizontal (Joy's law). We can also include magnetic field configurations, which allow flares and coronal mass ejections to occur. Additionally, there are the ingredients, introduced in the previous Chapters, in particular the effects of turbulent convection (see § 2) causing the solar differential rotation with the tachocline and the NSSL (see § 1.1).

There are different approaches to deal with the constraints mentioned above. Most of the approaches simplify the physical properties of their systems. There are the mean-field models, where the small-scale turbulent quantities are expressed and parametrized by mean quantities, see § 4.2 and Krause and Rädler (1980). These models are often utilized in two dimensional simulations. A subclass of these models are the kinematic models, where the backreaction of the magnetic field on the flow is neglected or just included in a rudimentary form. One example are the Babcock–Leighton dynamo models, see § 4.2.1. In contrast to the mean-field models are the direct numerical simulations (DNS) of solar dynamos, see § 4.3. There the fluid and magnetic Reynolds numbers are chosen above the limit of numerical diffusion and stability of the numerical setup. These values are orders of magnitude smaller than the realistic solar ones. Here, two additional simplifications are used. Instead of simulating the full spherical shell of the solar convection zone, often Cartesian boxes are used to simulate a region of interest as a part of the convection zone, see § 4.3.1. Also instead of self-consistent convective motion, random forcing is applied to generate turbulent motions. Groups doing local as well as global simulations (§ 4.3.2) use approximations for the fluid dynamics as incompressible or anelastic flows.

4.2 Mean-field models

In the mean-field models, we use the mean-field equations for the velocity field, the magnetic field and the density, see Eqs. (2.21) and (3.16) and Krause

and Rädler (1980). Additionally the mean energy equation is solved using expressions for the convective flux similar to Eq. (2.27) or Eq. (2.30). The main difficulty of these models is to find good values and profiles for turbulent viscosity ν_t, turbulent diffusivity η_t as well as for α and Λ (see § 2.4). For this we can use mixing length theory, see § 2.2.3, or they can be determined from direct numerical simulations by using a technique like the test-field method (Schrinner et al., 2007).

One issue for mean-field models is the implementation of the magnetic backreaction on the flow. In many models the Lorentz force in the momentum equation is either ignored (kinematic) or the time evolution of the fluid is not even solved and instead the flow field prescribed and used in the mean induction equation (see e.g. Dikpati and Charbonneau, 1999; Ossendrijver, 2003). Other models use algebraic quenching formulae for α, as in Käpylä et al. (2006b)

$$\alpha = \frac{\alpha_0}{1+\overline{\boldsymbol{B}}^2/B_{\rm eq}^2}, \tag{4.1}$$

which is the same as neglecting the mean helicity flux and the mean current density ($\boldsymbol{\nabla}\cdot\overline{\boldsymbol{\mathcal{F}}}_h^f = \overline{\boldsymbol{J}} = 0$) in Eq. (3.34), or solve an explicit evolution equation for α as Eq. (3.32). In general, models where the meridional circulation is able to transport the flux and is dominant over the turbulent diffusion are often called *flux-transport dynamo models*, when the toroidal magnetic field is produced at the bottom of the convection zone and leads to equatorward migration of mean magnetic field at the surface (see e.g. Dikpati and Charbonneau, 1999). Most of the models solve the equations of the α-Ω-dynamo model, where the differential rotation obtained by helioseismology enters as an input parameter. Mean-field models were able to reproduce successfully many observed features, as in Rüdiger and Brandenburg (1995), Dikpati and Charbonneau (1999), Ossendrijver (2003), Käpylä et al. (2006b), and Kitchatinov and Olemskoy (2012).

Transition between the differential rotation in the convection zone to the rigid rotation in the core leads to a region of strong shear below the convection zone, the tachocline (Spiegel and Weiss, 1980). Strong shear results in a strong Ω-effect and can amplify the toroidal field to large values. However, how large these values are, is debated (Brandenburg, 2005). But, because of the quenching of α in dependence on the equipartition field strength $B_{\rm eq}$, see Eq. (4.1), having the α-effect localized in the same region is difficult. Parker (1993) proposed an interface dynamo, where α is strong above the tachocline to avoid the strong quenching effects, see for example the approaches by MacGregor and Charbonneau (1997). In other approaches, like those of Rüdiger and Brandenburg (1995) and Käpylä et al. (2006b), α was calculated more sophisticatedly. As an example we show in Fig. 4.1 a butterfly diagram from

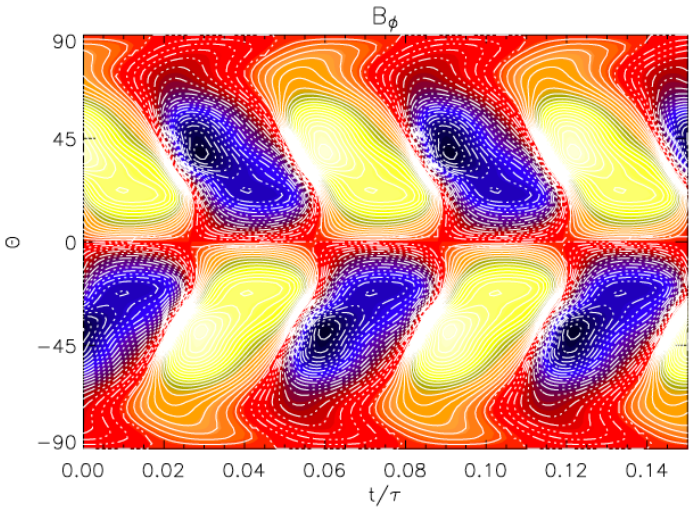

Figure 4.1: Butterfly diagram of mean azimuthal magnetic field $\overline{B}_{\rm phi}$ plotted over resistive time t/τ and latitude θ near the surface of the convection zone $r = 0.99\,R_\odot$ for a mean-field α-Ω dynamo model (from Käpylä et al., 2006b).

Käpylä et al. (2006b), where a meridional circulation of $u_{\rm m} = 10\,{\rm m\,s^{-1}}$ is used. Additionally the authors include the effect of the NSSL (Brandenburg, 2005) as well as turbulent pumping (see e.g. Ossendrijver et al., 2002; Käpylä et al., 2006a), where anisotropies in the α-tensor lead to advection of mean magnetic fields. The new approach of this work was that the transport coefficients were obtained from local three dimensional calculations of convection. As seen from Fig. 4.1, the mean-magnetic field migrates equatorwards at lower latitudes and polewards near the poles. Additionally the field is antisymmetric over the equator. This is precisely the behavior of the solar magnetic field. In these models, the mean-fields are defined by averaging in azimuthal direction and therefore are not capable of resolving the small-scales or describing flux concentrations as observed in sunspots. Describing these phenomena needs an additional model for forming flux concentrations, for which there have been different proposals (see e.g. Kitchatinov and Mazur, 2000; Brandenburg et al., 2011a; Stein and Nordlund, 2012).

4.2.1 Babcock–Leighton dynamo models

A different approach is to include the process of sunspot formation and their decay into a solar dynamo model. It is broadly believed that sunspots are formed by strong magnetic flux tubes emerging from the tachocline to the so-

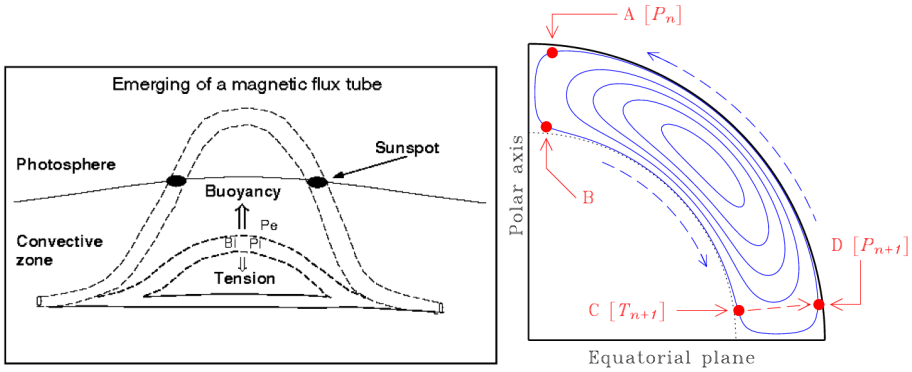

Figure 4.2: *Left panel:* A schematic sketch of an emerging magnetic flux tube. Due to magnetic buoyancy the flux tube rises from the bottom of the convection zone to the solar atmosphere. When it breaches through the photosphere it forms features like sunspots (After Parker, 1955, and Caligari et al., 1995). *Right panel:* Operation of a solar cycle model based on the Babcock–Leighton mechanism. The diagram is drawn in a meridional quadrant of the Sun, with streamlines of meridional circulation plotted in blue. Poloidal field having accumulated in the surface polar regions (A) at cycle n must first be advected down to the core–envelope interface (dotted line) before the production of the toroidal field for cycle $n+1$ can take place (B⇒C). Buoyant rise of flux ropes to the surface (C⇒D) is a process taking place on a much shorter timescale. From Charbonneau (2010).

lar surface and breaching as bipolar regions through the photosphere (see e.g. Ossendrijver, 2003; Charbonneau, 2010). I will first introduce the mechanism before discussing its results and criticism at the end of this section. It is known that strong shear in the tachocline can produce strong magnetic fields. If these fields get concentrated into flux tubes, they might rise due to the magnetic buoyancy effect, see § 3.1.3 for the description of the effect and an illustration in the left panel of Fig. 4.2. During its rise the tube might form a loop with an Ω shape, where the two *legs* breach through the solar surface and form the typical pattern of a bipolar region. This idea was already proposed by Parker (1955) and demonstrated in numerical models by Caligari et al. (1995). Numerical simulations of near surface loop emergence by Cheung et al. (2008) were able to reproduce observed features of sunspot emergence.

Babcock (1961) and Leighton (1964) introduced a new mechanism, which can be used for solar dynamo models. As described in § 1.4, sunspot pairs have a leading and a following spot (in respect with rotation) with opposite polarity. On average the leading spot emerges at lower latitudes than the following spot (Joy's law). Because of the differential rotation the spots will lose their

cohesiveness. Eventually the leading spot will decay by coalescing with another sunspot of opposite sign from the other hemisphere. The following spot will be advected by meridional circulation toward the poles, where it forms together with other decaying sunspots a polar field of the sign of the former following sunspot. Flux tubes rising to the surface will be deflected by the Coriolis force resulting in twisted tubes and the tilt angle of the sunspot pairs following Joy's law. This effect is actually an α-effect operating on larger scales as the turbulence, but in comparison to the large-scale magnetic field of Sun, these scales are still small. Therefore, the Babcock–Leighton effect is nothing else than a local α-effect represented in Eq. (3.16) operating on larger scales than the turbulence and being confined to the near surface region. For the Babcock–Leighton mechanism, we need a meridional circulation and a differential rotation as a input for the flow. This is a kinematic flux-transport dynamo model, where the magnetic backreaction on the flow is completely neglected. Because the problem is axisymmetric and one hemisphere is independent of the other, it can be calculated as a two dimensional model with toroidal and poloidal fields in one hemisphere. The two amplification mechanisms (Ω and Babcock–Leighton) are separated in location and are only connected by the meridional circulation. In the right panel of Fig. 4.2, the scheme of the Babcock–Leighton-Model is shown. Starting at point A, the poloidal magnetic field of cycle n is transported by the meridional circulation downwards to the tachocline (A$\Rightarrow$B). There the field is transformed into a strong toroidal field due to the differential rotation and is transported towards the equator by the meridional circulation (B$\Rightarrow$C). The strong toroidal field rises to the surface due to magnetic buoyancy and generates sunspots of cycle $n+1$ (C$\Rightarrow$D). Then the sunspots decay and form a new reverse polar field (D$\Rightarrow$A).

The success of these models emerges from the good agreement with observations. With Babcock–Leighton models many observed features can be reproduced (see e.g. Dikpati and Charbonneau, 1999, Charbonneau, 2010, and reference therein), including grand minima in the solar cycle (see e.g. Karak, 2010). But this model is also strongly criticized, because of its simplifications (see e.g. Brandenburg, 2005). First of all, the formation of sunspots via emerging flux tubes is not well verified. If a flux tube emerges via magnetic buoyancy, also its volume expands and the magnetic field decreases. Therefore the generated magnetic field at the tachocline has to be large (100 kilo-gauss, see Choudhuri and Gilman, 1987), maybe too large to be generated by a dynamo mechanism (see e.g. Guerrero and Käpylä, 2011). Whether a flux tube survives the journey to the surface through violent turbulent convection depends crucially on the amount of magnetic twist in the tube (see e.g. Fang et al., 2010). The advection of the following spot of a sunspot pair to the poles implies that the spots in the pair loose their cohesiveness. These are strong simplifications,

which are in contradiction with the effects of magnetic tension and pressure within the spots as well as the anchoring of the spots in the underlying azimuthal magnet field. One of the important assumptions of these models is the one-cell meridional circulation and Joy's law. The one-cell meridional circulation have been recently questioned by improved observations by Hathaway (2011) and simulations by Miesch et al. (2012). As one might think, Joy's law is an observationally determined law. But the tilde angle between the line between the two sunspots in a pair and the horizontal line is not always the same. It turn out, that detailed measurements show a large scatter range of the angle, which can be even negative at some occasions (Kosovichev and Stenflo, 2008; Stenflo and Kosovichev, 2012). Therefore, the generality of Joy's law is not always given. In all, the Babcock–Leighton dynamo model suffers from a strong lack of verifiable physical properties of the solar environment. With the use of fine-tuned parameters, this model is capable of modeling a lot of observed features without providing understanding of their real origin.

4.3 Direct numerical simulations

Instead of simplifying or parameterizing the MHD equations, one can also solve directly by using viscosities and diffusivities far above the solar values. The advantage of these models is that effects like turbulent heat transport or the α-effect, which arise from magnetohydrodynamical turbulence, do not have to be included artificially. The results of these simulations are in general more reliable than mean-field models, because no fine tuning of turbulent coefficients is possible. On the other hand analyzing and describing their results in terms of physical quantities might be more difficult.

4.3.1 Local simulations

Solar dynamo simulations of a small region of the Sun are used to study local phenomena or general properties of dynamos. Simulating only a part of the convection zone allows us to reach higher fluid and magnetic Reynolds numbers. In simulations of turbulent dynamo models it is common to use random forcing in the momentum equation to mimic turbulent convective motions, without actually solving the energy equation. In the work by e.g. Pouquet et al. (1976), Käpylä et al. (2006a) and Hubbard et al. (2009), local direct numerical simulation with forced turbulence are used to estimate transport coefficients as α, where the test field method (Schrinner et al., 2007) may be employed in determining the transport coefficients. For details I refer to Brandenburg et al. (2010) and references therein.

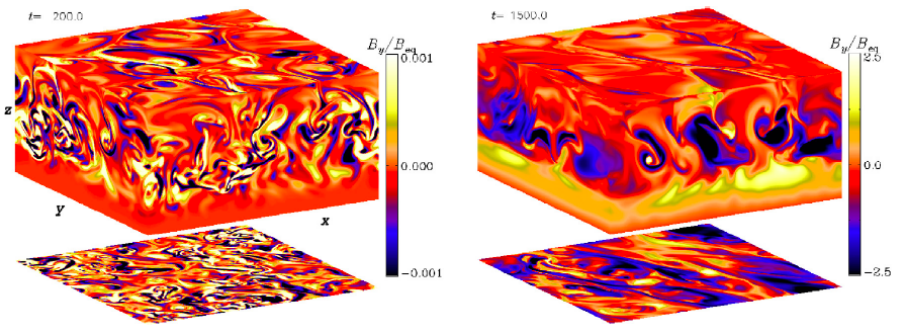

Figure 4.3: Large-scale magnetic field from a simulation of turbulent convection with shear in a Cartesian box. In the left panel the early phase is shown, where the magnetic field is weak and has the same as the convection or smaller one. In the right panel the saturated state is shown. The magnetic field is more than two times larger than $B_{\rm eq}$. The sides of the box show the periphery of the domain whereas the top and bottom slices show B_y at bottom and the top of the domain, respectively (taken from Käpylä et al., 2008).

Local convective simulations generating the turbulent motions self-consistently started with Meneguzzi and Pouquet (1989) and Nordlund et al. (1992), who showed that the turbulent pumping effects lead to a downdraft of magnetic fields. Later as shown by Käpylä et al. (2008), it was possible to generate for the first time large-scale magnetic fields generated by turbulent convection using shear. Recently, local simulations have been used to estimate the possibility of creating flux tubes with convection and shear (Guerrero and Käpylä, 2011). But the maximum magnetic field strength obtained by their simulations is $\sim 6\,B_{\rm eq}$. Some of the flux tubes are even able to rise up to the surface, but they always lose their initial coherence.

Assuming that the Babcock–Leighton mechanism is the right one to describe the large-scale fields and the sunspot emergence, the question remains, where the magnetic field of smaller or intermediate strength come from. One proposed mechanism is a small-scale dynamo operating in the surface layer of the Sun, driven by the small-scale turbulent motion of the granulation. These ideas are investigated in local dynamo simulations (see e.g. Cattaneo, 1999; Vögler and Schüssler, 2007). It is possible to excite a small-scale dynamo just by the turbulent motions without any rotation and shear, for details see the review by Stein (2012). Concerns, the magnetic Prandtl number ($\mathrm{Pr_M} = \mathrm{Re_M}/\mathrm{Re}$) is with $\mathrm{Pr_M} \ll 1$ too small for a small-scale dynamo to operate, was resolved by Brandenburg (2011). In **Paper I** we also use a local model of a solar dynamo driven by random forcing. In the following papers,

we expand the domain to global simulations.

4.3.2 Global simulations

Global simulations of solar dynamos are in most cases still utilizing a model describing only a part of the Sun. Describing the physics of the convection zone is sufficient. In some cases, polar regions are omitted to avoid the coordinate singularity at the axis, so instead of the whole sphere just a spherical wedge is used (see e.g. Käpylä et al., 2010; Mitra et al., 2010b, and **Papers II–VI**). In other models the whole convective spherical shell was modeled by using the anelastic approximation $\boldsymbol{\nabla} \cdot (\rho \boldsymbol{u}) = 0$, thus filtering out sound waves (see e.g. Brun et al., 2004).

The first global numerical simulations of solar dynamo models by Gilman and Miller (1981), Gilman (1983) and Glatzmaier (1985) were already able to produce remarkable results. The mean magnetic field showed an oscillating behavior, but it migrated polewards. Due to larger computing power in the last 30 years, more realistic global simulations were possible. Even though their luminosity and rotation rate are similar to those in the Sun, their fluid and magnetic Reynolds numbers are still several orders of magnitude lower than the solar ones. One way of dealing with this issue is to use large-eddy simulations (LES), where small-scale turbulence effect are added to the direct numerical simulations. These models were used to simulate successfully large-scale magnetic fields generated self-consistently by convection in spherical shells (see e.g. Brun et al., 2004; Brown et al., 2008). For rotation rates larger than solar, large-scale active so-called wreaths of non-oscillatory magnetic field were found (Brown et al., 2010). The azimuthal field concentrated at lower latitudes and is organized in loosely bundled flux tubes. More recently, using these models, also oscillating large-scale magnetic fields were found (Brown et al., 2011; Nelson et al., 2013, and references therein), but these oscillating patterns are far from solar-like regular patterns. The azimuthal magnetic field consist of strong wreath, which change their polarity irregularly and with no significant correlation in the two hemispheres. These wreaths migrate from time to time polewards but never equatorwards. For solar rotation rates, Brun et al. (2004) failed to produce large-scale magnetic fields. Using grid methods instead of spherical harmonics, Ghizaru et al. (2010) and Racine et al. (2011) were able to produce oscillatory large scale magnetic fields, but without any clear migration.

Approaches, where instead of a full sphere a spherical wedge is used, have been successful in generating large-scale migrating magnetic fields. With random forcing of helical transversal waves, Mitra et al. (2010b) could produce an oscillatory magnetic field with equatorward migration. In this case the migra-

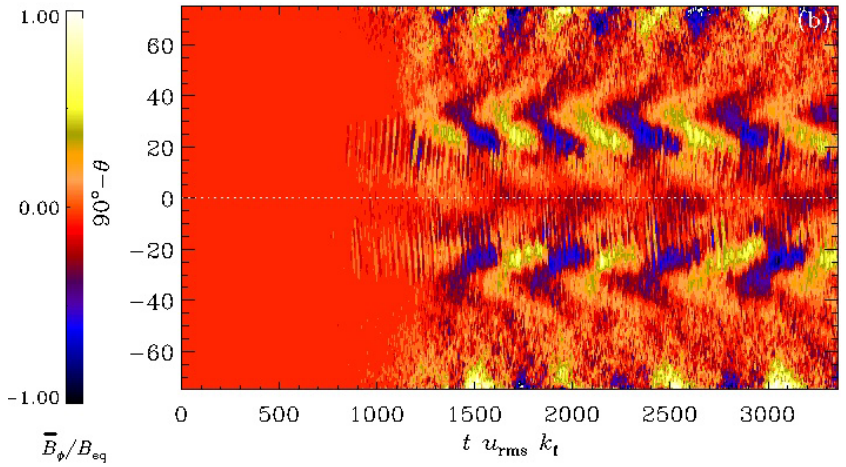

Figure 4.4: Butterfly diagram for the mean azimuthal magnetic field $\overline{B}_\phi$ near the surface of the convection $r = 0.98\,R_\odot$ as a function of latitude $90° - \theta$ for $\mathrm{Co} = 7.6$. The white dotted line denotes $90° - \theta = 0$ (taken from Käpylä et al., 2012, and **Paper VI**).

tion can be explained by a sign change of α across the equator. In this model no rotation is applied, but the sign of the kinetic helicity are reversed across the equator, which mimics the effect of the solar rotation. The same effect has been seen in the model of **Paper II**. Simulations of self-consistent convective dynamos in spherical wedges were at first unable to reproduce oscillatory magnetic fields (see e.g. Käpylä et al., 2010, and **Paper IV**). But recently, with the implementation of an LES approach for the turbulent heat conductivity $\chi_{\rm t}$ (Käpylä et al., 2011b) and a black body boundary condition for the temperature, Käpylä et al. (2012) were able to produce an equatorward migration of the large-scale magnetic field. In Fig. 4.4 the butterfly diagram of the mean azimuthal magnetic field is shown. There exists a clear equatorward migration of the field between latitudes of 40° and 60°, which has a cycle period of 33 years, clearly longer than the solar magnetic cycle. Near the pole, there exists a poleward migrating branch, which is similar to the observed pattern as seen in Fig. 1.6. **Paper VI** is a follow-up work of Käpylä et al. (2012), where we investigate mainly how the density stratification influences the equatorward migration of the mean field as shown in Fig. 4.4. The magnetic field is again generated by self-consistent convection in a rotating spherical wedge. The mean azimuthal magnetic field shows poleward migration for all runs in the beginning of the simulations, when the magnetic field is weak. For high enough stratification (density contrast above 25) this pattern is overcome by equatorward migration. For a slight increase of magnetic and fluid Reynolds

number the pattern does not change significantly. As in Käpylä et al. (2012), the Coriolis numbers in these runs are around slightly higher than that in the Sun. At the moment the work of Käpylä et al. (2012) and its followup work of **Paper VI** are the state of the art of equatorward migration of self-consistent convective dynamos. In **Paper V** we find a similar pattern, but the higher latitudes show strong equatorward migrations instead of poleward. Unfortunately the mechanism for the equatorward migration behavior is still unclear and need more investigation. In § 6, I will discuss the difference in the setup as well as the results in more detail.

An important result of the global convection simulations is that the magnetic field is distributed over the whole convection zone. Although Nelson et al. (2013) detect even flux tubes, there are no clear signs of their formation in the tachocline, from where they should rise and contribute to the solar cycle. In this sense, the direct numerical simulations of the global solar dynamo support the distributed dynamo model of Brandenburg (2005).

Let me also make a note about the differential rotation in solar dynamo models. The differential rotation in direct numerical simulations is normally not an input quantity as in the mean-field and flux-transport models: it emerges instead from the simulations. Kitchatinov and Rüdiger (2005), Miesch et al. (2006) and Brun et al. (2011) use only hydrodynamical models to be able to reproduce solar-like differential rotation. This can be misleading, because Maxwell stresses as well as suppression of turbulent heat fluxes due to magnetic fields (e.g. Käpylä et al., 2004) can influence the differential rotation. Solar dynamo models were able to generate an equator rotating faster than the poles for higher than solar rotation rates (e.g. Nelson et al., 2013, and **Paper VI**), but spoke-like rotation contours as in Fig. 1.2 or in mean-field hydrodynamical models by Brandenburg et al. (1992) and Kitchatinov and Rüdiger (2005) have only been achieved in hydro-LES by imposing a latitudinal entropy gradient at the bottom of the convection zone (Miesch et al., 2006) or with a stably stratified layer below the convection zone, which mimic the radiative interior (Brun et al., 2011). The only MHD DNS models of self-consistent convection reproducing spoke-like rotation are those with a coronal envelope of **Paper V**. I will present and discuss its results in § 6 in more detail.

5. Models of Solar Eruptions

Explosions are not comfortable.

Yevgeny Zamyatin

In this chapter, I want to give a short overview about the different models of solar eruptions. First I present some observational constrains of solar eruptions and then the models of these eruptions. More detailed information can be found in the reviews by Chen (2011) and by Shibata and Magara (2011), whereas observations of coronal mass ejections (CMEs) are summarized by Webb and Howard (2012). Solar eruptions can be categorizes into two main groups of phenomena. One are the solar flares, which are impulsive emissions of radiation accompanied by a sudden increase of brightness and particle showers. The other one are coronal mass ejections (CMEs), where plasma of the corona gets ejected out into the interplanetary space. Often and in particular for strong events, these two phenomena are connected (see e.g. Harrison, 1995). The energy released in such events have been stored before inside the magnetic field.

5.1 Observational constrains

On the first day of September 1859, Carrington (1859) and Hodgson (1859) observed the first flare in the continuum light on the photosphere. In the left panel of Fig. 5.1, a sketch of the sunspot region is shown, from which this flare emerged. The flare and the associated CME led to a strong geomagnetic storm, which is know as the Carrington event. It was the largest ever recorded solar storm, which resulted in aurorae in the Caribbean and telegraph failures in the US and Europe. More detailed observation of flares and CMEs are possible since space telescopes are monitoring the Sun. Flares are hard to observe from the ground, because either they are emitted only in this part of the spectrum, which is absorbed by the Earth's atmosphere, or the coronal emissions are much weaker than the photospheric ones. After the first mission, of the NASA space station Skylab, the Sun was monitored permanently by the SOlar and Heliospheric Observatory (SOHO: Domingo et al., 1995) built by ESA and NASA. With the instruments on SOHO, the photosphere, the chromosphere and the solar corona can be observed simultaneously 24 hours a day. Additionally there were two white light coronagraphs (LASCO) on board, which

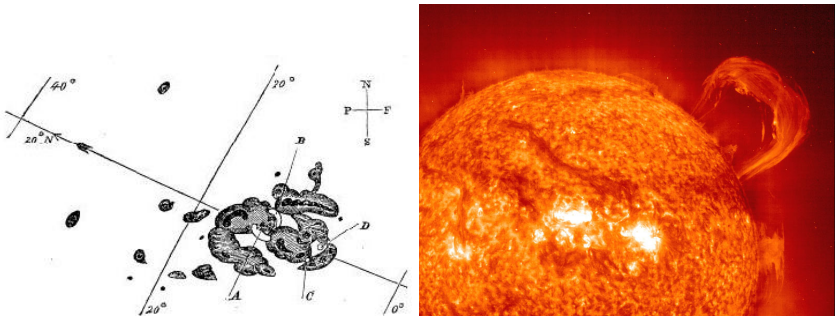

Figure 5.1: *Left panel:* Sketch from the first observed and noted sunspot formation, which lead to a solar flare. The British astronomer Richard Carrington had done this drawing of the Sun at the 1st of September 1859, after he had observed a solar flare for the first time. The white regions among the black and gray sunspots represent the Doppler ribbons (A and B) of the white flare which emerge suddenly amid the sunspots (Carrington, 1859). *Right panel:* Solar prominence observed with EIT on SOHO in the He II/Si XI 304 Å line band. Image courtesy of NASA/ESA.

are able to observe the shapes of CMEs as shown in Fig. 5.2. Nowadays, the Dynamic Solar Observatory (SDO: Pesnell et al., 2012) gives us remarkable pictures and data of solar flares and coronal mass ejections. With the twin spacecrafts Solar TErrestrial RElations Observatory (STEREO: Kaiser et al., 2008) CMEs can be observed three-dimensionally, which gives important insights of the structure and evolution of CMEs.

Flares have a power law energy distribution, which range from weak nanoflares, releasing energies of about 10^{19} J, to white flares, releasing energies of about 10^{24} J. Nanoflares are believed to contribute to the heating process in the solar corona (e.g. Bingert and Peter, 2011, 2013). White flares are strong flares and can cause major impacts on the Earth. Because of the observation of even stronger flares on other solar-type stars, Maehara et al. (2012) suggested that superflares, which are hundred times more powerful than white light flares, are also able to occur on the Sun. Typically the flare is first visible as two ribbons in Hα emitted from the chromosphere, as see in left panel of Fig. 5.1. Later, strong X-ray and UV emissions follow from X-loops in the corona.

Coronal mass ejections (CMEs) can be divided into two main categories. There are jet-like ejections, the narrow CMEs and there are the cone-like ejections, the normal CMEs. In the following I will focus on the normal type of CMEs. Normal CMEs are basically prominences, which are ejected into the interplanetary space (House et al., 1981). In the right panel of Fig. 5.1, an example of a prominence observed with EIT on SOHO, is shown. Hot plasma can

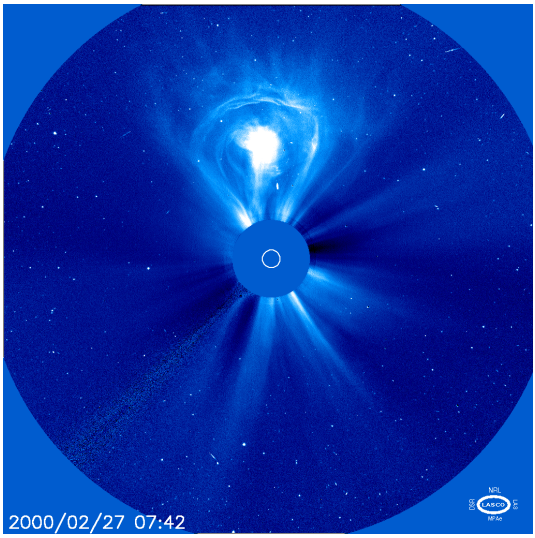

Figure 5.2: This SOHO LASCO C1 image shows a very large coronal mass ejection (CME) blasting off into space on 27 February 2000. It presents the standard shape of a CME: a large bulbous front with a second, more compact, inner core of hot plasma. This material erupts away from the Sun at speeds of one to two million kilometers per hour. Image credit ESA and NASA.

only flow along the magnetic field lines for example of a coronal loop and can be trapped there. If field lines reconnect underneath this prominence and release sufficient magnetic energy to push the prominence out, a CME happens. The hot and dense prominence will show up as a bright bubble in projected white light image, as in Fig. 5.2. In front of this emerging bubble the coronal plasma will pile up and form a bright arc. The bright bubble, the cavity in between and the bright arc form the characteristic three-part structure of CMEs (see e.g. Illing and Hundhausen, 1985; Low, 1996). Ahead of the arc, the CME causes shocks, which can accelerate particles to high velocities. These particles can then penetrate the Earth's atmosphere. The plasma, which is carried out with the CME is often called magnetic cloud (Rust, 1994). This plasma has a typical mass of 10^{11} to 10^{13} kg (see e.g. Hudson et al., 1996) and can reach a velocity of 1000 km/s. Coronal mass ejections are believed to carry a large amount of magnetic helicity out of the Sun, (e.g. Low, 1994, 2001; Plunkett et al., 2000; Régnier et al., 2002; Thompson et al., 2012). Magnetic clouds can form bipolar magnetic field, just due to their rotation and inclination (see e.g. Li et al., 2011, where they use in-situ measurements of two satellites). More measurements of current helicity, which can serve as a proxy for magnetic helicity, and magnetic twist could be important for dynamo theory. Blackman

and Brandenburg (2003) suggested CMEs to be a major contributor to magnetic helicity transport out of the Sun and so to prevent catastrophic quenching of the α-effect, see § 3.3.1.

5.2 Models and simulations

For powering CMEs and flares, one needs a large amount of energy (10^{25} J). In the solar atmosphere only the magnetic field can supply this amount of energy. As calculated in Stix (2002), a volume of $10^{23}\,\mathrm{m}^3$, with a field strength of a hundred gauss have a magnetic energy of around 4×10^{24} J, which is of the same order as the flare energies of 10^{25} J. The thermal and kinetic energy are much lower, and not sufficient to store this amount of energy. As a basic step, modeling flares and CMEs starts by modeling the storage of energy in the magnetic field. Observations suggest strong shearing motions localized near strong magnetic field gradients in active regions before a flare or CME erupts. Sturrock (1980) and Antiochos et al. (1999) use shearing motions to model magnetic storage in the corona. Also Warnecke (2009) found indications that granulation motion is capable of twisting and shearing the magnetic field to store sufficient energy for a flare or CME.

For studying the mechanism of eruptive events, it is often sufficient to use two dimensional models. For example Forbes and Priest (1995) and Priest and Forbes (2000) are able to reproduce the spread of Hα ribbons and X-loop structures in the after-flare phase by using a two dimensional force-free reconnection model. Simplified flux rope models can be used to generate a current sheet and trigger the ejection of flux ropes.

In three dimensions, there are two different types of models commonly used. The first one is the break-out model (see e.g. Antiochos et al., 1999). There, a multi-flux system of coronal fields is used to form complex magnetic topologies in the corona. To trigger the eruption, they use an observed photospheric magnetogram and impose velocities similar to the observed ones. The shearing motions lead to reconnection of the coronal field, which then causes the eruption. Here, the coronal field topology is crucial for eruptions to happen, and the storage of energy is comparable to the one needed to release CMEs. The second type of model are the three-dimensional flux rope-models. There, a twisted flux rope (configuration see Titov and Démoulin, 1999) is placed into a simulation model, where to bottom represents the photosphere. Shearing the footpoints of this rope breaks its stability and causes a rise and twist of the rope. This have been studied intensively by Török et al. (2004) and Török and Kliem (2005), where they were able to reproduce a rising and twisting prominence similar as in observed ones on the Sun as shown in Fig. 5.3. In their simulation they solved the ideal MHD equations, where no reconnection can

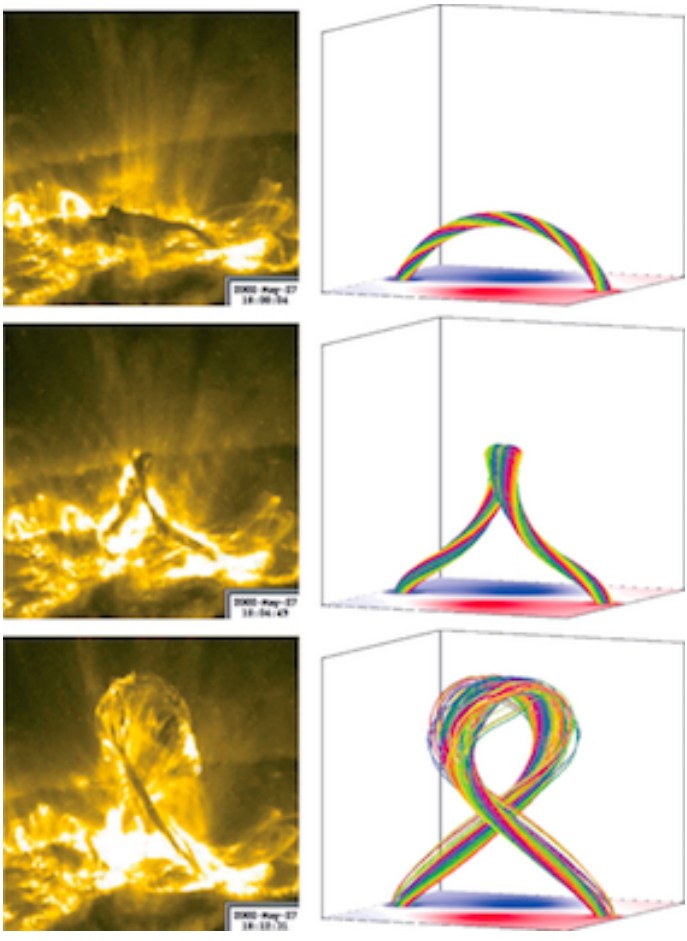

Figure 5.3: Comparison of observations and simulations, time is evolving from top to bottom: *Left panel*: TRACE 195 Å images of the confined filament eruption on 27th May 2002. *Right panel*: Colored magnetic field lines outlining the core of the kink-unstable flux rope with starting points lie in the bottom plane. The magnetogram of the vertical magnetic field is shown color coded at the bottom of the box (taken from Török and Kliem, 2005).

happen, this prohibited the flux rope from ejecting. A slightly different approach has been conducted by Fan and Gibson (2004, 2007), where a twisted flux rope emerges into a prescribed coronal field configuration. It becomes unstable and ejected depending crucial on the amount of twist. With this model they were able to reproduce X-ray observation of intense current layers of inverse-S-shapes on the northern hemisphere. Similar simulation have been also performed by Roussev et al. (2003) to find suitable trigger mechanism.

For other models using the flux emerging and shearing motions to trigger an erupting flux rope see e.g. Amari et al. (2000). Similar flux-rope models are used to simulate the formations of CME shocks (see e.g. Pomoell et al., 2008). These shocks are of particular interest, because they can accelerate particles to high speeds penetrating the Earth's atmosphere and lead to high doses of radiation.

At the moment, in all models of erupting events, the initial condition are prescribed. The magnetic field at the bottom of the domain is either taken from two-dimensional observations of the photospheric magnetic fields or set by hand. The overall magnetic field is the extrapolated from the bottom field or also completely set by hand as by including a flux rope configuration. Twisted magnetic field has to be included artificially or by implying strong shearing motions at the footpoints. Observing horizontal velocity field is only possible with a low accuracy and low resolution, and they are not even sufficient to actually trigger the ejections (see e.g. Baumann et al., 2012). That the magnetic field configuration and the velocity field are connected to magneto–convection and a dynamo process below the surface, is often neglected. In § 6 I will therefore describe a different approach, where we combine the dynamo process below the surface to trigger coronal ejections, see also **Paper I** - **IV**.

6. A Combined Two-Layer Model

Das Studium und allgemein das Streben
nach Wahrheit und Schönheit ist ein Gebiet,
auf dem wir das ganze Leben lang
Kinder bleiben dürfen.

Albert Einstein

6.1 Motivation

The main purpose of this thesis is to develop a two-layer model combining the solar convection zone and the solar corona. There are basically two motivations for the combined two-layer model. One path originates from modeling coronal mass ejections and flux emergence. As described in § 1.5, coronal mass ejections and solar flares are contributing to the space weather, which has a strong impact on the life on Earth. Despite this importance, a reliable prediction of space weather events and in particular solar storms is currently not possible. After the detection of solar eruptions on the solar surface using space telescopes, it takes about one to five days for them to reach the Earth. This time interval is currently the maximum advance warning time we have. Predictions about the strength and velocity of the ejection can be only made during this interval. There have recently been major advances in simulating and observing coronal mass ejections and solar flares, see § 5. However, the mechanism leading to eruptions is not yet fully understood. Whether an active region is likely to erupt, can often only be answered using statistical arguments rather than physical understanding (see e.g. Schwenn, 2006). It is generally agreed that the solar magnetic field not only supplies the energy source, but it also triggers the eruptive events. On the Sun, however, the magnetic field is only observable in the photosphere and above; information about magnetic fields in the interior of the Sun is not accessible. This is one of the reasons, why most of the models of solar eruptions use photospheric magnetic fields as lower boundary condition, see § 5. The surface magnetic field is the only observable field, which is useful to include in an eruptive event model. One might believe that this is the most realistic boundary condition, but this is actually misleading. If

twisted magnetic fields and other complex topologies are projected onto a two-dimensional plane at the solar surface, the regaining magnetic field information from this projection will be insufficient and possibly wrong. But these complex topologies and twisted fields might be one of the important ingredients missing in the eruption models. To generate twisted magnetic fields in these models, either strong shearing motions are applied at the bottom of their domain, representing the photosphere or twisted magnetic fields are just imposed in the domain as initial conditions. The fact that the magnetic field structures and the photospheric motions are coupled together in terms of magneto-convection or dynamo action is often neglected. The combined two-layer model developed in this thesis connects the fluid motions below the surface of the Sun with the fluid on and above the surface directly, as well as the magnetic field below and above the surface. In eruptive models, the twist of the magnetic field plays an important role and can also be found in observed coronal mass ejections (see e.g. Thompson et al., 2012). Instead of imposing twisted fields or generating them by at least partially artificial photospheric motions, another possibility is that these twisted fields are generated by dynamo action below the surface. Differential rotation and convection is capable of producing helical magnetic fields, which contain a large amount of twist. Our combined two-layer model allows twisted magnetic fields, which have been generated below the surface, to emerge and to contribute to CMEs.

The other motivation starts from dynamo theory. As described in §§ 3.2 and 4, magnetic helicity and magnetic helicity fluxes are important quantities in dynamo theory and solar dynamo models. Dynamo action can be catastrophically quenched for high magnetic Reynolds numbers (see e.g. Brandenburg and Subramanian, 2005, and § 3.3.1). The only loophole is via magnetic helicity fluxes, which are capable of preventing catastrophic quenching of the α-effect (Blackman and Field, 2000; Brandenburg et al., 2009). From this point of view, an appropriate boundary condition for the magnetic field is crucial for the performance of the dynamo. Numerical simulations have shown that a dynamo can be more efficient with open (vertical field) boundaries than with closed (perfect conductor) ones (Brandenburg and Sandin, 2004). In the Sun, the convection zone has no closed boundaries at the surface. Magnetic fields can emerge through the surface and can be eventually ejected. We know that the Sun has a powerful dynamo operating inside the convection zone. If the dynamo theory of quenching the α-effect (see § 3.3.1) is reliable, the Sun has to transport large amounts of magnetic helicity out of the convection zone. Possible candidates for the transport are the solar wind and coronal mass ejections (Blackman and Brandenburg, 2003). Coronal mass ejections are a good candidate, because they are believed to carry magnetic helicity outwards (see e.g. Thompson et al., 2012).

Observations of magnetic helicity on the solar surface are difficult to perform. Magnetic helicity is not a gauge-invariant quantity and is therefore impossible to be determined unambiguously, but there are mechanisms to determine the relative helicity or proxies for the magnetic helicity such as the current helicity (Pariat et al., 2005; Thalmann et al., 2011; Valori et al., 2012). But even the gauge invariant current helicity can only partly be observed and measured, because the horizontal components of the current density are not accessible.

The combined two-layer model can be used to create a realistic boundary condition for the solar dynamo, similar to the solar photosphere. We can determine if such a boundary condition supports a dynamo below the surface and can be even more efficient than without giving the possibility of ejections of magnetic helicity. We can investigate the interplay between the solar convection zone and the solar corona in terms of dynamo-driven ejections as well as magnetic helicity fluxes with this model.

6.2 Model and setup

The model consists of two layers, where the lower one represents the solar convection zone and the upper one the solar corona. In the lower layer we use turbulent motions to amplify a weak Gaussian-distributed seed magnetic field. There are no imposed or initial magnetic fields in the upper layer. Magnetic fields are only able to emerge from the lower layer into the upper layer in order to have magnetic field in the upper layer. One of the important features of the combined two-layer model is that there are no numerical boundaries between the two layers. The different dynamics of the two layers are controlled in the used equations by a choosing suitable profile function multiplying terms on the right hand side of the MHD equations, see § 3. This allows a flux of magnetic helicity and magnetic fields between the two layers. For the numerical computations, we use the PENCIL CODE with sixth-order centered finite differences in space and a third-order accurate Runge–Kutta scheme in time. For the extension of the PENCIL CODE to spherical coordinates see Mitra et al. (2009).

6.2.1 Step by step

The combined two-layer model is simple at the starting point and has been improved step by step. In every step, we include more realistic physical features leading to new useful insights and results. Using a step-by-step method allows us to adjust the model, where improvements are important and needed. It also allow us to compare the results of every step with the former ones.

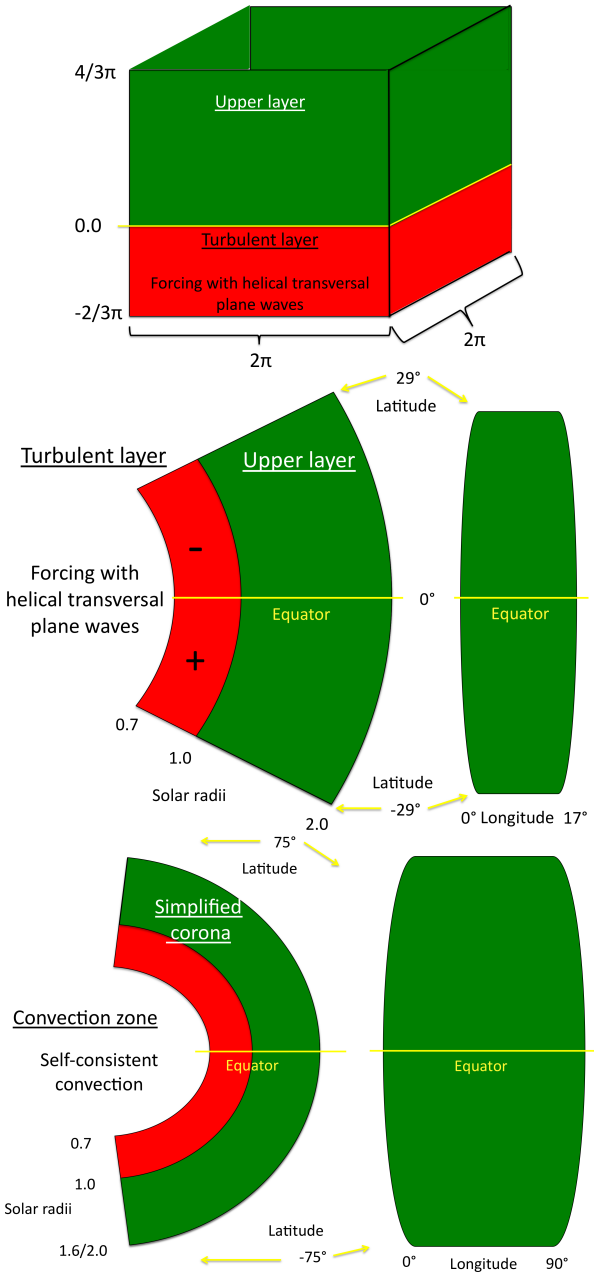

Figure 6.1: Schematic sketch of the model setup of **Paper I** (top), **Paper II** (middle) and **Papers IV** and **V** (bottom).

6.2.2 A forced turbulent dynamo in a Cartesian box

As a first step we use a model in a Cartesian box, see top panel of Fig. 6.1. This model is used in **Papers I** and **III**. The lower layer, which is about one third of the total domain, mimics the convection zone and the upper layer represents the solar corona. In the lower layer, we impose a forcing function in the momentum equation which injects random helical transverse waves in the domain. Profile functions arrange for a smooth transition from the forced momentum equation in the lower layer to a non-forced one in the upper layer. The forcing is used to mimic convective turbulent motions and its helical part represents the influence of rotation and stratification on these motions. We neglect gravity and solve the continuity equation only in the lower layer supporting the turbulent motions. We omit the energy equation and apply instead a constant temperature in the whole domain. This leads to so-called force-free model in the coronal layer, which has been used to model properties of the solar corona as well as plasmoid ejections, which fits well with observations of coronal fields (see e.g. Mikic et al., 1988; Ortolani and Schnack, 1993; Warnecke, 2009). It implies that processes like magnetic buoyancy are not captured. The boundary conditions are periodic in the x and y directions. In the z direction, we use a stress-free boundary condition for the velocity field. For the magnetic field we employ a perfect conductor at the bottom boundary and a vertical field condition ($B_x = B_y = 0$) on the upper boundary. The vertical field condition is chosen, because in the solar corona the solar wind pushes the field lines radially at a distance of around $r \approx 2 \ldots 2.5 R_\odot$ (see e.g. Levine et al., 1982; Schrijver and De Rosa, 2003).

6.2.3 A forced turbulent dynamo in a spherical domain

As a second step, we transform the setup from Cartesian to spherical coordinates. We now model a major part of the Sun, as shown in the middle panel of Fig. 6.1 using a spherical wedge, which extends from the bottom of the convection zone at $r = 0.7 R_\odot$ to the upper solar corona at $r = 1.6 \ldots 2 R_\odot$. In the latitudinal (θ) direction we omit the poles and limit ourselves to latitudes of ± 0.5 radians (corresponding to $\pm 29^\circ$). The wedge has a 17° extent in the azimuthal (ϕ) direction for simplicity. This model is used in **Papers II** and **III**. Besides the use of spherical coordinates, there are two main improvements added to the model. As the first one, we include gravity, which is much weaker than in the Sun, and solve the continuity equation in the whole domain. This leads to a radial density stratification covering in most of the simulations, around one or two orders of magnitude, while in the Sun, the density contrast is around 14 orders of magnitude. Secondly, we apply a latitudinally dependent forcing function. The kinetic helicity density $\boldsymbol{u} \cdot \boldsymbol{\omega}$ imposed in terms of

the helical forcing, is largely negative in the northern hemisphere and positive in the southern hemisphere. This mimics the different sign of the kinetic helicity in both hemispheres due to solar rotation, which is omitted in this model. As in the Cartesian model, we omit the energy equation and use a constant temperature. The boundary conditions are periodic in the ϕ-direction while in the radial direction they are similar to those of the z-direction in the Cartesian model. On the θ-boundaries, we employ stress-free velocity and perfect conductor boundary conditions for the magnetic field. We prevent a flux of mass at the outer radial boundary of the full domain, because an open boundary allows a Parker wind to develop. A Parker wind for this low gravitation is too strong and would push all the magnetic field out of the domain in a short time.

6.2.4 A convective dynamo in a spherical domain

As a third step we use self-consistent convection to generate a large-scale magnetic field. This model is used in **Paper IV**, where we combine a setup used by Käpylä et al. (2010, 2011b) for the convection zone with the isothermal coronal model of **Paper II**. We extend the domain to latitudes of ± 1.3 radians (corresponding to $\pm 75^\circ$) and to longitudes of $\pi/2$ radians (90°), see lower panel of Fig. 6.1. As one of the improvements, we solve the energy equation in terms of the entropy, see Eq. (3.9) and use a cooling function to keep the temperature at the surface of the convection zone and in the corona constant. We impose a with radius decreasing profile for the heat conductivity and an initial temperature profile of a polytropic atmosphere with an index of $m = 1$ to generate an convectively unstable stratification in the convection zone. Additionally, we switch to a rotating frame, by adding the Coriolis force in the momentum equation, but we neglect the centrifugal force (see discussion in Dobler et al., 2006). This leads to the generation of differential rotation and helical motions inside the convection zone. The density contrast is now around four in the convection zone and forty in the whole domain, i.e. higher than in **Paper II**, but still not much closer to the solar density stratification. Due to the low density in the corona, the Coriolis force is there unrealistically strong compared to the Lorentz force[1]. This leads to strong velocity gradients and possible artefacts such as the magneto-rotational instability. That is why we employ a damping term in the momentum equation to reduce the mean velocities in the corona, see details in Section 2.2 of **Paper IV**, but actually the damping violates Galilean invariance. The boundary conditions are very similar to those of the model of **Paper II**. However, for the temperature, we use a constant heat flux at the bottom and constant temperature at the top boundary.

[1]In Eq. (2.12), the Coriolis force would enter on the rhs as $-\boldsymbol{\Omega}_0 \times \boldsymbol{u}$, the Lorentz force as $\frac{1}{\rho}\boldsymbol{J} \times \boldsymbol{B}$.

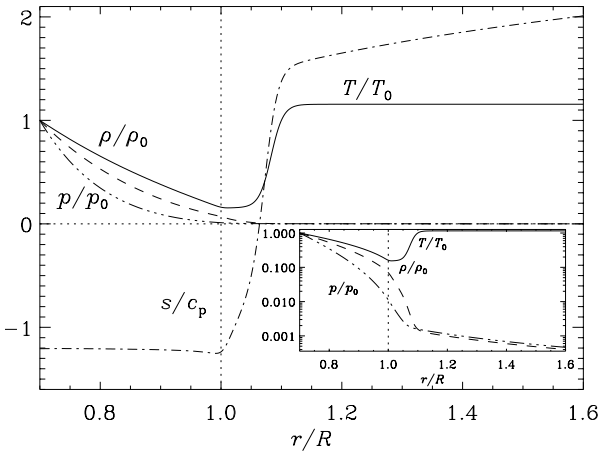

Figure 6.2: Mean radial profiles of stratification for one representing run of **Paper V** in the equilibrated state. The normalized density ρ/ρ_0 (dashed lines), pressure p/p_0 (dash-triple-dotted), and temperature T/T_0 (solid) are plotted together with the specific entropy s/c_P (dash-dotted) over the radius. The inset shows the same profiles in logarithmic representation to emphasize the steep decrease of the pressure and density in the lower coronal layer. The index 0 represents the value at the bottom of the convection zone.

At the latitudinal boundaries the entropy and the density have zero gradients to avoid heat fluxes in and out of the domain.

6.2.5 A convective dynamo in a spherical domain with a hot corona

In a forth step, performed in **Paper V**, we improve our model in two aspects. We use a more advanced convection zone model similar to Käpylä et al. (2011a, 2012) (also employed in **Paper VI**), where the decrease of the heat conductivity with radius is stronger in the convection zone and a turbulent heat conductivity χ_t is introduced. The latter resembles the unresolved convective heat flux, see § 2.2.4 and is in this sense an LES feature. This leads to a much higher convective flux than in **Paper IV**. The energy equation then reads (compare with Eq. (3.9) and Equation (4) in **Paper V**)

$$T\frac{\mathrm{D}s}{\mathrm{D}t} = \frac{1}{\rho}\boldsymbol{\nabla}\cdot(K\boldsymbol{\nabla}T + \chi_t\rho T\boldsymbol{\nabla}s) + 2\nu\mathsf{S}^2 + \frac{\mu_0\eta}{\rho}\boldsymbol{J}^2 - \Gamma_{\rm cool}(r). \tag{6.1}$$

There, $\Gamma_{\rm cool}(r)$ is a radially dependent cooling function, which is also improved compared with the one in **Paper IV**. We impose a cooling profile which causes a higher temperature in the corona than at the bottom of the convection zone.

In Fig. 6.2, an overview of the mean radial profiles of density, pressure and temperature is plotted for the model used in **Paper V**. Using this type of temperature profile allow us to achieve much higher density contrasts than in the models of **Papers II** and **IV**. The density contrast in the convection zone is now around fifteen, whereas in the whole domain it is about two thousand. We apply the same boundary conditions as in **Paper IV**. It turns out that the velocity damping used in the model of **Paper IV** could be better realized by a viscosity profile than an actually damping term in the momentum equation. The viscosity increases to an about twenty times higher value in the corona than in the convection zone. This is sufficient to damp high velocities in the corona, at least in the first stage, when the magnetic field is still weak. Also, because of the stronger stratification the Coriolis forces are not that strong as in **Paper IV**.

More detailed descriptions of the model setups can be found from the model sections of **Papers I, II, IV** and **V**. To summarize, the convection zone of our two-layer model has been evolved from a simple local isothermal layer, where random helical forcing generated a magnetic field to a global layer with self-consistent convection, self-generated differential rotation and a magnetic field generated by the turbulent convective motions. Likewise, the coronal layer develops from an isothermal, zero-gravity force-free model to a realistic corona, where the temperature is high and the density low.

6.3 Main results of Paper I to V

In the following I present the main results of **Papers I–V** as well some unpublished additional results. The order follows rather the result topics than the publishing chronology.

6.3.1 Magnetic field generation

In all papers a large-scale magnetic field is generated by turbulent motions in the lower layer representing the convection zone. In **Paper I** the saturated magnetic field is bipolar, where its alignment direction is a random choice of the system. The vertical component of the field varies sinusoidally in one of horizontal directions and is essentially constant in the other. The field pattern is stationary, but can move slowly in one of the directions, see Figs. 7 and 9 of **Paper I**. In the model of **Paper II** the saturated magnetic field shows an equatorward migration due to an α-effect, which changes sign across the equator, similar to Mitra et al. (2010b). In Fig. 6.3, we show the equatorward migration of the radial magnetic field at the surface of the lower layer. Two polarities of opposite sign are generated at the poles and move toward the equator,

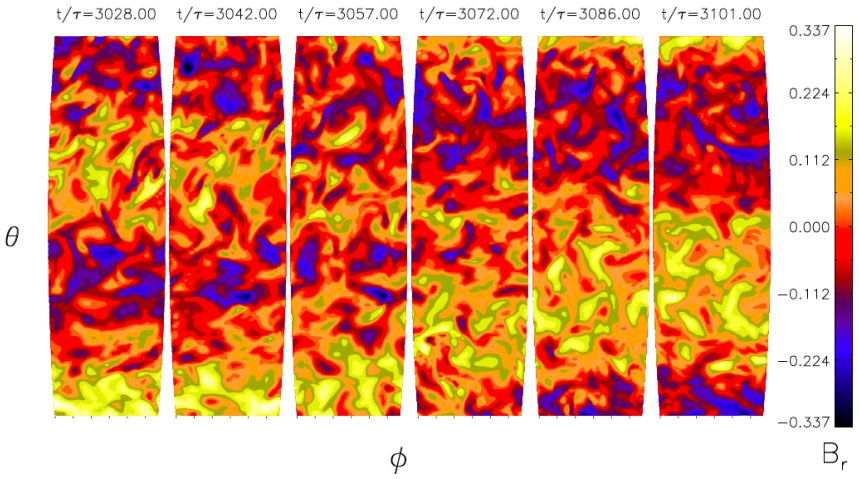

Figure 6.3: Equatorward migration, as seen in visualizations of the normalized radial magnetic field $B_r/B_{\rm eq}$ at the surface ($r = R_\odot$) over a horizontal extent of $\Delta\theta = 58^\circ$ and $\Delta\phi = 17^\circ$ for six different time snapshots. $\tau = 1/u_{\rm rms}k_{\rm f}$ indicates the turnover time of the turbulent motions (taken from **Paper II**).

where they annihilate. At the same time the polarities in each hemisphere have changed and new magnetic fields move equatorward, see Fig. 5 in **Paper II**.

The model used in **Paper IV** shows no clear sign of equatorward migration (Figs. 10 and 11 of **Paper IV**). The mean (azimuthal averaged) magnetic field seems to be stationary and forms "wreaths" of strong fields, similar as in Brun et al. (2004), Brown et al. (2008) and Nelson et al. (2013). The field shows no sign of polarity change, but some changes in strength. They are in phase with velocity changes, similar as in **Paper II**; the field is strong, when the velocity is weak, and vice versa, see Fig. 5 of **Paper II** as well as Fig. 9 of **Paper IV**. In the model used in **Paper V**, the magnetic field is clearly oscillatory and shows indications of equatorward migration of the mean magnetic field. In Fig. 6.4, the butterfly diagram of the mean radial field is shown close to the surface of the convection zone ($r = 0.97R_\odot$). During the first hundred turnover times the magnetic field is weak and a poleward migration is visible. But at later times the equatorward migration is strong and penetrates again down to the equator. After around $t/\tau = 1500$ the dynamo seems to change its mode and the equatorward migration vanishes or becomes less clear, but at $t/\tau = 2300$ it reoccurs and penetrates to the equator. The magnetic cycle period is around $t/\tau = 150$ turn over times. Assuming a typical turnover time for convective motion in bulk of the solar convection zone of a month, this cycle would cor-

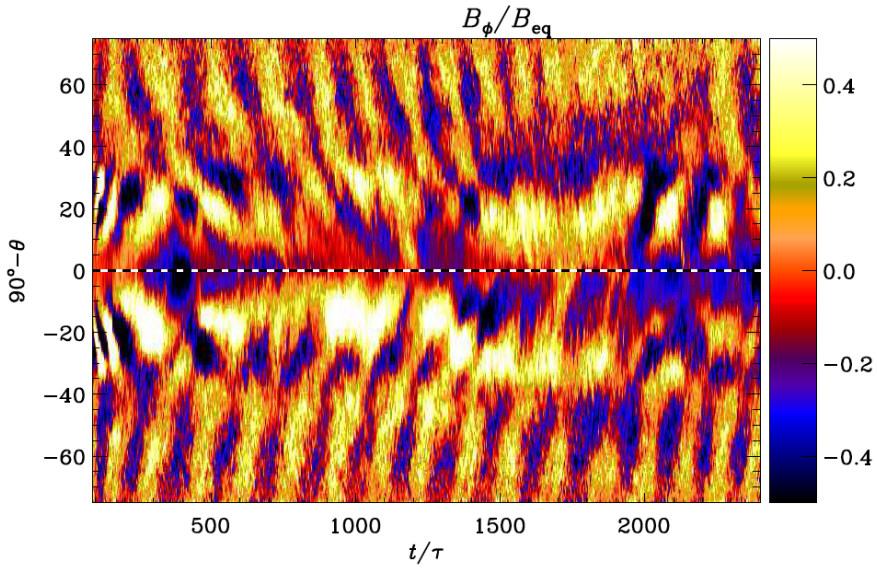

Figure 6.4: Time evolution of the mean radial magnetic field $\overline{B}_r$ in the convection zone at $r = 0.97\,R_\odot$. The dashed horizontal lines show the location of the equator at $\theta = \pi/2$. The magnetic field is normalized by its equipartition value $B_{\rm eq}$. Overbars indicate azimuthal averages (taken from **Paper V**).

respond to around 12 years, which is very close to the 22 years of the solar magnetic cycle. Besides the work by Käpylä et al. (2012) and **Papers V** and **VI**, equatorward migration was not previously reproduced in direct numerical simulations, see § 4. Brown et al. (2011) and Nelson et al. (2013) were able to produce an oscillatory magnetic field with highly irregular cycles and poleward migration. In the work by Racine et al. (2011), the authors found regular oscillatory mean magnetic fields, but no clear equatorward migration. One reason for the success of Käpylä et al. (2012) might be the use of a new developed thermal boundary condition at the surface of the convection zone following a black-body boundary condition, which lets the temperature vary in time and space. This not only allows us to measure the irradiance variation due to the magnetic cycle as done in **Paper VI**, it is less restrictive than forcing the temperature or the entropy gradient to be a constant at the boundary as e.g. in Brun et al. (2004, 2011) and Miesch et al. (2006). In the model of **Paper V**, the coronal layer serves as an even less restrictive boundary condition. The cause of the equatorward migration can be only clearly revealed, if one determines the transport coefficients. Racine et al. (2011) used a rudimentary way to calculate the α-tensor while neglecting the turbulent diffusivity tensor,

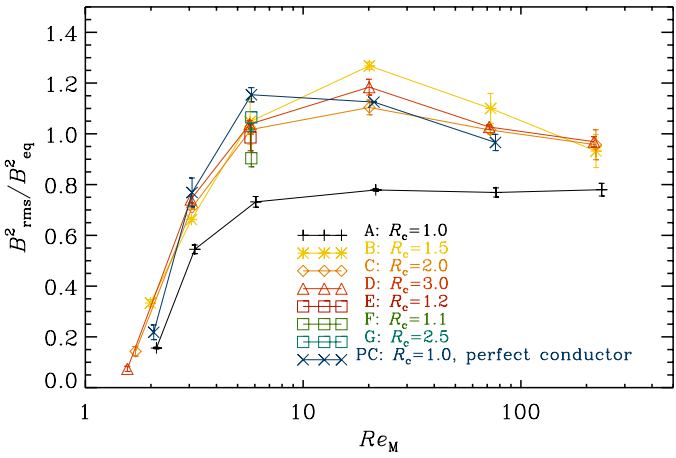

Figure 6.5: Dependence of magnetic field energy normalized by the equipartition value $B^2_{\rm rms}/B^2_{\rm eq}$ with coronal radial extent $\rm R_C$ and magnetic Reynolds number $\rm Re_M$. The solid black line indicates the dynamo region without any corona, the other colors have coronal radial extents of $1.1\,R_\odot$, $1.2\,R_\odot$, $1.5\,R_\odot$, $2.0\,R_\odot$, $2.5\,R_\odot$, and $3.0\,R_\odot$. The blue line represents simulations with a perfect conductor boundary condition at top boundary in radial direction ($r = \rm R_C$) (taken from Warnecke et al. 2013b, in preparation).

which limits their results fundamentally. A more accurate and reliable way to determine the transport coefficients including the turbulent diffusivity tensor is the test-field method, developed by Schrinner et al. (2007), which is at the moment not implemented in spherical coordinates.

The magnetic field pattern in Fig. 12 of **Paper V** (compare also with the other panels of Fig. 12 and 13 of **Paper V**) is different from that in Fig. 1.6 of the Sun and Fig. 4.4 of Käpylä et al. (2012) and **Paper VI**. In **Paper V** the equatorward migration exists to high latitudes and is there also more stable than at lower latitudes. In the Sun and in the work by Käpylä et al. (2012) as well as in **Paper VI**, there exists a polar branch, where the field migrates towards the while, and the equatorward migration is stronger at low latitudes. However, the parameters in both of the simulations show also some difference. For example, the runs of **Paper VI**, which produce equatorward migration have a stronger stratification, i.e. the density contrast in the convection zone is 14 in **Paper V** while being ≥ 25 in **Paper VI**.

The model of **Paper II** is well suited for testing, whether a coronal layer supports a dynamo in the lower layer. As shown in Fig. 6.5, the magnetic field strength in terms of $B^2_{\rm rms}/B^2_{\rm eq}$ is significantly higher for models with a corona than for models without. This is a remarkable result, taking into account that in

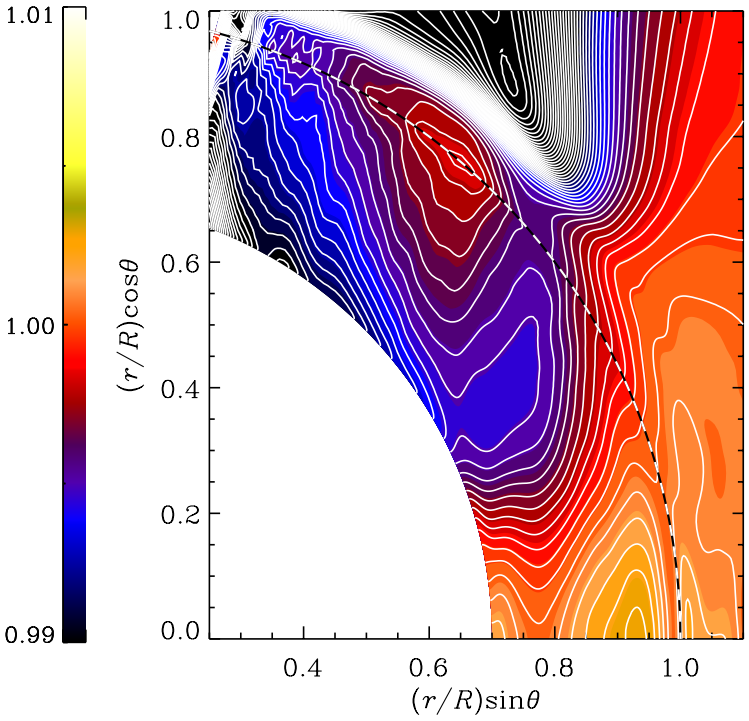

Figure 6.6: Differential rotation in the convection zone in the northern hemisphere. The mean rotation profile $\overline{\Omega}(r,\theta)/\Omega_0$ is shown color coded and with white contours. The white-black dashed line indicates the surface ($r = R_\odot$). Overbars indicate azimuthal averages (taken from **Paper V**).

the simulations without a corona, a vertical field condition is applied at the upper boundary. A combined two-layer model is capable of supporting dynamo action in addition to the helicity fluxes allowed by the vertical field condition. The vertical field condition might be too restrictive as it forces the magnetic field into a certain configuration, which has a lower dynamo saturation value, see also § 6.4.

6.3.2 Differential rotation

Differential rotation plays a role only in **Papers IV** and **V**, because in the other ones no rotation is included. In the model of **Paper IV**, the stratification is weak and the convective flux is not as strong as the radiative flux. This causes that the Taylor–Proudman balance is not broken and the rotation profile is cylindrical in the convection zone as well as in the corona, see Fig. 6 of **Pa-**

per IV. The model of **Paper V** is more suitable for investigating the differential rotation. We found the new and interesting result of a solar-like differential rotation profile. As described in § 2.4 and § 4.3.2, direct numerical simulations of global convective dynamos in spherical shells were not able to reproduce a solar-like differential rotation pattern. In pure hydrodynamic simulations this can be accomplished only by imposing a latitudinal entropy gradient at the bottom of the convection zone (Miesch et al., 2006) or by including a stably stratified layer below the convection zone (Brun et al., 2011). As shown in Fig. 6.6, the equator rotates in our model faster than the poles, which has also been achieved in other DNS and LES models (e.g. Käpylä et al., 2011b, 2012; Nelson et al., 2013, and **Paper VI**). The important features are the roughly radial contour lines of constant rotation in the convection zone. This is generated for the first time self-consistently in a direct magnetohydrodynamical numerical simulation. We find out that the Taylor–Proudman balance is broken by the baroclinic term in the mean azimuthal vorticity equation, see Eq. (2.37) and Fig. 5 of **Paper V**. This is related to a 8% higher temperature at higher latitudes than at the equator. It is still puzzling, that we do not see any similar spoke-like differential profiles in the runs without any corona of **Paper VI**. One of the reasons might be, that the transition region containing large temperature and density gradients provides an isolation between the convection zone and the corona. However, a realistic description of the upper thermal boundary as an open boundary might be crucial also in this sense. The results of Brun et al. (2011) show, that a more realistic treatment of the lower thermal and velocity boundary can also lead to a realistic differential rotation profile including the generation of a tachocline. See the details of this discussion in Section 3.1 and 3.2 of **Paper V**.

Additionally, the differential rotation profiles obtained in the model of **Paper V** show a near-surface-shear layer (NSSL), at low latitudes. This is a promising result, because we know from mean-field simulations, that the NSSL plays an important part for the solar dynamo, generating a solar-like oscillation pattern and migration direction of the mean magnetic field, (see Käpylä et al., 2008, and § 4). In the LES model of Brun et al. (2011), the differential rotation is similar to the rotation profile obtained by helioseismology (see e.g. Thompson et al., 2003), but no NSSL was found by the authors, also because the near-surface stratification was not included in these models. This leads to the conclusion, that a corona supports the generation of an NSSL, due to less restrictive boundary also for the velocity field.

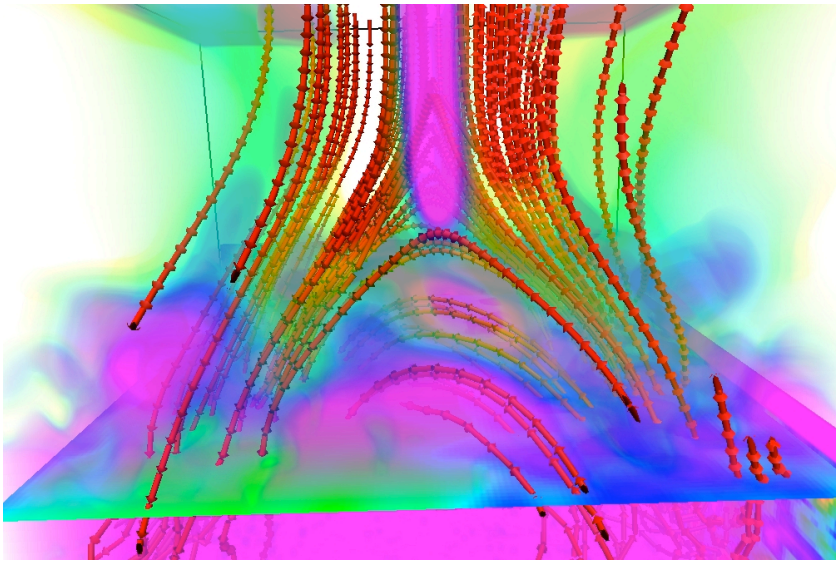

Figure 6.7: Magnetic field structure in the upper layer of the domain. Field lines are shown in red and the modulus of the current density is shown in pink with semi-transparent opacity. Note the formation of a vertical current sheet above the arcade (taken from **Paper I**).

6.3.3 Coronal field structure

The model of **Paper I** shows a significant magnetic structure in the coronal layer. Confined by the bipolar field and the vertical field boundary condition, an arcade of magnetic field lines is formed. In Fig. 6.7 we show a three dimensional visualization of this structure. Magnetic field lines form closed loops between opposite polarities on the surface as well as open field lines which connect to the upper boundary. At the interface between them an inverted Y-point is formed. Such a point is basically the lower end of an extended X-point. As plotted in Fig. 6.7, the location of the Y-point coincides with the formation of a current sheet. In a more realistic simulation, this current sheet would correspond to a region of strong Ohmic heating and energy dissipation. This energy could be released as a flare. In the model of **Paper II**, the magnetic field in the corona forms a structure similar to magnetic clouds, which are ejected recurrently. A deeper discussion on this will follow in § 6.3.4. Besides the coronal ejection, the coronal magnetic fields influence the rotation in the models of **Papers IV** and **V**. As shown in Fig. 2 of **Paper V**, the rms velocity averaged over the whole domain decreases due to the growing magnetic field. After the coronal magnetic field reaches a certain strength, the rotation

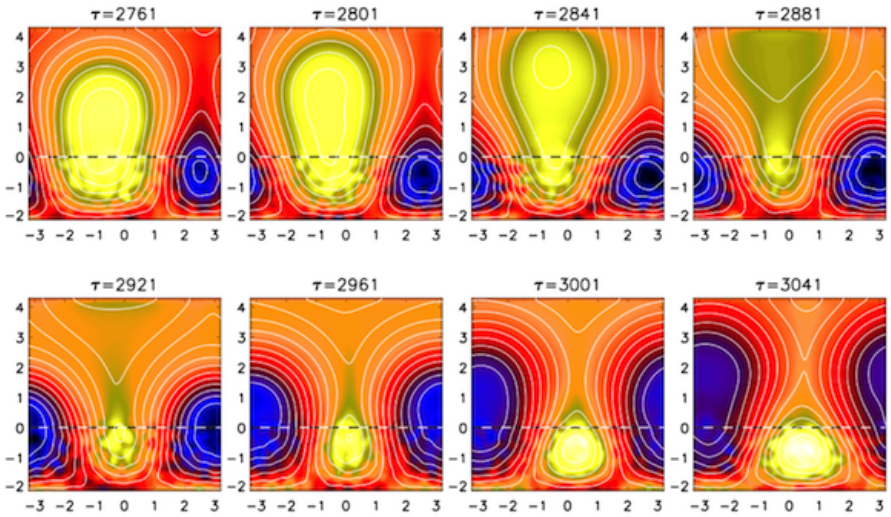

Figure 6.8: Time series of the formation of a plasmoid ejection. Projections of field lines of $\langle \boldsymbol{B} \rangle_x$ in the yz plane are shown together with a color-scale representation of $\langle B_x \rangle_x$; blue stands for negative and yellow for positive values. The dotted horizontal lines show the location of the surface at $z = 0$. τ indicates here the time normalized to the turnover time. The angle brackets represent averages in the direction of the subscript (taken from **Paper I**).

in the corona is quenched essentially to the same level as the turbulent motion inside the convection zone. This is an important numerical result. Until now, the rotation of the solar corona is not clearly determined by observations, see Section 2.2 in **Paper IV**.

6.3.4 Coronal ejections

In **Papers I–IV**, the detection of coronal ejections can be reported. However, in the model of **Paper V**, we see indication of ejections (not yet published), but in **Paper V** we focus on the physical properties of the convection zone. Using the model of **Paper I**, we produce ejections of magnetic field structures and current helicity density $\boldsymbol{J} \cdot \boldsymbol{B}$. Looking at lines of the magnetic field averaged in the x direction, we find plasmoids recurrently getting ejected from the coronal layer out of the domain. In Fig. 6.8, a positive B_x concentration is lifted up and emerges through the top boundary. Between the third and fourth panels in the second row of Fig. 6.8, a reconnection event happens, similar to what is shown in Fig. 6.7. After the positive flux concentration has been erupted, a new negative flux concentration has emerged and will be erupted shortly after

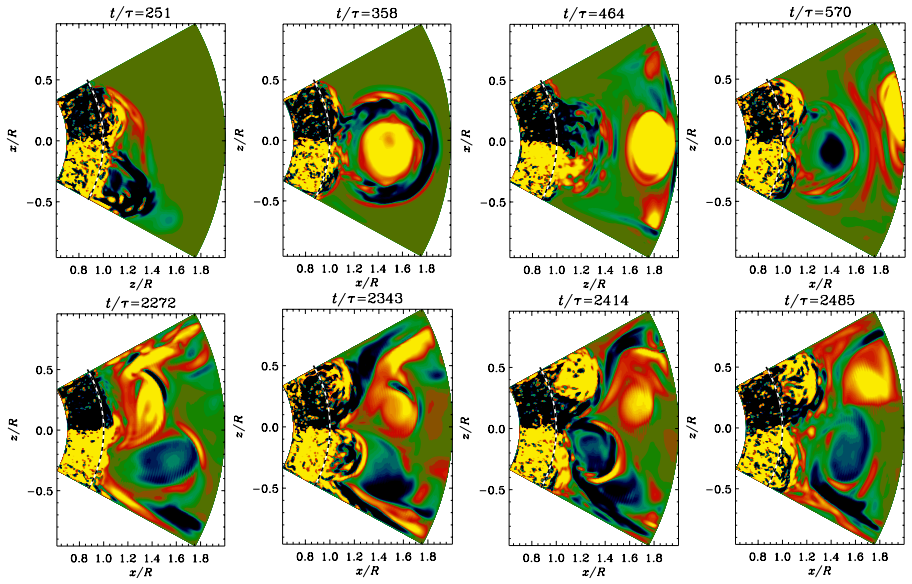

Figure 6.9: Time series of coronal ejections in a spherical wedge. The normalized current helicity, $\mu_0 R\overline{\boldsymbol{J}\cdot\boldsymbol{B}}/\langle\overline{\boldsymbol{B}^2}\rangle_t$, is shown in a color-scale representation for different times; dark/blue stands for negative and light/yellow for positive values. The dashed lines show the location of the surface at $r^2 = x^2 + z^2 = R^2 = R_\odot^2$. Overbars indicate azimuthal averages (taken from **Paper III**).

that. Looking at a time-height diagram of current helicity, as in Fig. 3 of **Paper III**, one notices that the ejections happen regularly and carry a substantial amount of current helicity out of the domain. Here it is notable that magnetic buoyancy is not the dominant force, at least in our simulations. Therefore, the emergence and ejection of magnetic field structures must be due to the Lorentz force that is basically due to the twists of the fields. Twisted magnetic fields tend to untwist, because of the magnetic tension as part of the Lorentz force, see Eq. (3.14). The most important way to untwist in this setup is to emerge to the coronal layer or out of the domain through the top boundary. The model we used in **Paper II** is able to produce coronal ejections of similar shape as observed in coronal mass ejections. In Fig. 6.9, we show a time series of coronal ejections by plotting the normalized current helicity $\mu_0 R_\odot\overline{\boldsymbol{J}\cdot\boldsymbol{B}}/\langle\overline{\boldsymbol{B}^2}\rangle_t$ for different times. In the upper row a strong ejection has emerged close to the equator and is pushed out of the domain. The ejection consists of a bubble-like structure in the center and a bow in the front, which is very similar to the three-part structure in observed coronal mass ejection on the Sun (see e.g Illing and Hundhausen, 1985; Low, 1996, and § 5). The bow seems to have always the opposite sign of current helicity than the bubble, which can be re-

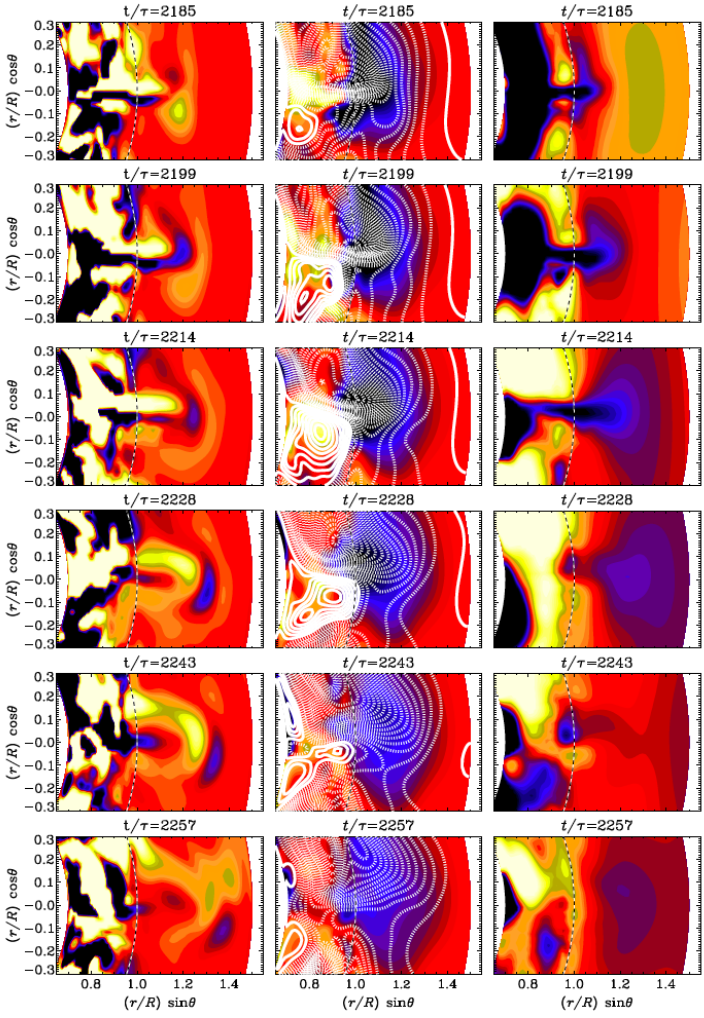

Figure 6.10: Time series of a coronal ejection zoomed into the region of the ejection near the equator ($\theta = \pi/2$), taken from Run A5 of **Paper IV**, where turbulence is driven by convection. The dashed curved vertical lines show the location of the surface $r = R = R_\odot$. *Left column*: normalized current helicity, $\mu_0 R\overline{\boldsymbol{J}}\cdot\overline{\boldsymbol{B}}/\langle\overline{\boldsymbol{B}}^2\rangle_t$. *Middle column*: magnetic field, field lines of $\overline{\boldsymbol{B}}$ projected into the r,θ plane, where solid lines represent clockwise magnetic field lines and the dashed ones counter-clockwise are shown together with a color-scale representation of $\overline{B}_\phi$. *Right column:* density fluctuations $\Delta\overline{\rho}(t) = \overline{\rho}(t) - \langle\overline{\rho}\rangle_t$. For all plots, the color-scale represents negative as dark blue and positive as light yellow (taken from **Paper IV**.)

lated to a bipolar magnetic structure. Such bipolar magnetic structures have been observed in magnetic clouds (see e.g. Li et al., 2011). The occurrence of ejections is not always close to the equator. However, their emergence seems often to coincide with the annihilation of the magnetic field polarities at the equator, as described in § 6.3.1. Also in our model, magnetic buoyancy is not dominant, because the field generated by a forced turbulent dynamo is not concentrated enough to couple efficiently to the pressure distribution as our simulations show. Therefore the emergence and ejection of the magnetic field can be explained by the untwisting of helical structures. Looking here also at the time-height current helicity diagram, one finds recurrences, similar to those in the Cartesian model of **Paper I**. The pattern of recurrence depends on the fluid and magnetic Reynolds numbers (Re, $\mathrm{Re_M}$); see Fig. 12 of **Paper II** for lower Re and $\mathrm{Re_M}$ and Fig. 6 of **Paper III** for higher Re and $\mathrm{Re_M}$.

In the model of **Paper IV**, ejections are not that easy to detect as in the previous models. The magnetic field is weaker and less helical. Additionally, the ejections are smaller and hence more difficult to find in a larger domain. We have performed many more runs than those mentioned in **Paper IV**, but only in a few of them, we could detect ejections. These isolated structures can be found best by plotting the current helicity density. In Fig. 6.10 we show the time series of the current helicity density, the magnetic field and the density disturbance of such an isolated structure. In the current helicity density, we found a bipolar structure similar to those in **Paper II**, but much smaller and less pronounced. This is correlated with strong radial magnetic field concentrations near the surface. The density disturbance indicates the emergence of a magnetic flux tube, whose density is lowered due to magnetic pressure. Because of the low stratification inside our model, the tube stays less dense than its surroundings and does not carry mass into the corona. Unfortunately, the resolution of this isolated structure is not that high, because it is a global simulations. A detailed analysis of this ejection shows a clear bipolar structure in the current helicity represented by two current sheets and a strong radial magnetic field, see Fig. 16 of **Paper IV**. The recurrence of the events is not as regular as in **Papers I** and **II**, but we can detect several events happening during the simulated time.

6.3.5 Magnetic helicity and current helicity

Already in the model of **Paper I**, we found a different sign of current helicity in the coronal layer than in the dynamo layer, see Fig. 3 of **Paper III**. The current helicity is positive in the lower layer, where the dynamo is operating and negative in the upper layer, representing the corona. In the spherical model of **Paper II**, the reversal of sign is even more pronounced. In Fig. 6.9, the current

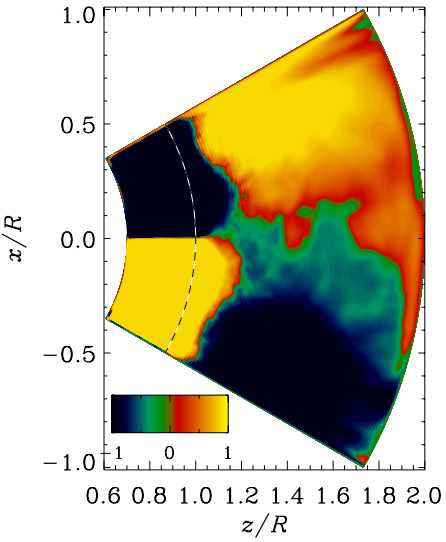

Figure 6.11: Time averaged current helicity $\mu_0 R_\odot \langle \overline{\boldsymbol{J}\cdot\boldsymbol{B}} \rangle_t / \langle \overline{\boldsymbol{B}^2} \rangle_t$. Dark/blue corresponds to negative values, while light/yellow corresponds to positive values, as in Fig. 6.9. The dashed line shows the location of the surface at $r^2 = x^2 + z^2 = R^2 = R_\odot^2$ (taken from one of the runs of **Paper III**).

helicity in the convection zone has a negative sign in the northern hemisphere and a positive sign in the southern hemisphere. This is a result of the sign of the helical forcing applied in this part of the domain. In the corona, we notice that (in particular in the second row of Fig. 6.9) the current helicity carried by the ejections has opposite signs as in the corresponding part in the convection zone of each hemisphere: they are positive (yellow) in the northern hemisphere and negative (blue) in the southern hemisphere. This can be seen even more clearly in a time-averaged plot, as shown in Fig. 6.11. There we have averaged over nearly 4000 turnover times, and see that the sign of current helicity changes in the outer atmosphere. This behavior has been confirmed by *Ulysses* spacecraft observations of the magnetic helicity (Brandenburg et al., 2011b). This satellite measures the magnetic field far from the ecliptic which allows us to compute the magnetic helicity using the Taylor hypothesis, see Matthaeus et al. (1982) and Brandenburg et al. (2011b) for details. In the latter paper, it was found that the magnetic helicity in the solar wind changes its sign at a certain distance from the Sun, similar to the results found in our simulations. In **Paper III**, we use a simple analytical model to explain this sign reversal. The current helicity is related to the magnetic helicity of the fluctuating field, see Eq. (3.28). Therefore, we can use Eq. (3.31) with Eq. (3.17), neglecting

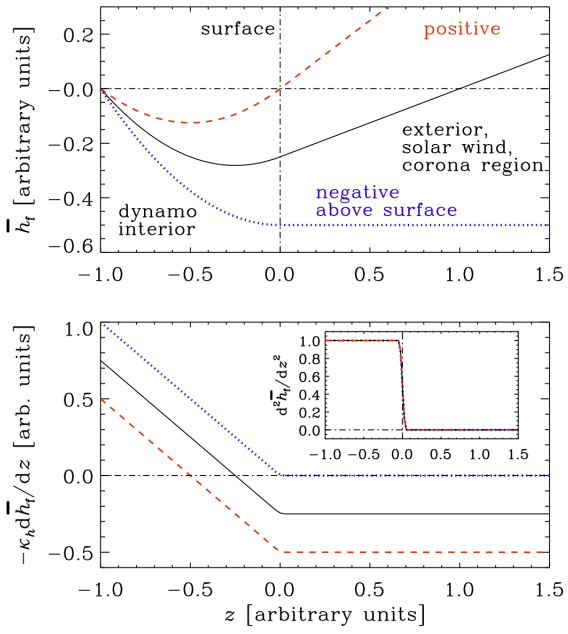

Figure 6.12: Sketch showing possible solutions of Eq. (6.3) for the mean helicity density of the fluctuating fields $\overline{h}_f(z)$ with $S = \mathrm{const} = -1$ in $z < 0$ and $S = 0$ in $z > 0$ (upper panel). The red (dashed) and black (solid) lines show solutions for which the magnetic helicity flux ($-\kappa_h \mathrm{d}\overline{h}_f/\mathrm{d}z$, see lower panel) is negative in the exterior. This corresponds to the case observed in the Sun. The blue (dotted) lines show the case, where the magnetic helicity flux is zero above the surface and therefore does not reverse the sign of $\overline{h}_f(z)$ in the exterior (taken from **Paper III**).

the molecular diffusivity η and assuming a steady state, to derive the equation

$$\boldsymbol{\nabla} \cdot \overline{\boldsymbol{\mathcal{F}}}_h^f = -2\alpha \overline{\boldsymbol{B}}^2 + 2\eta_\mathrm{t} \mu_0 \overline{\boldsymbol{J}} \cdot \overline{\boldsymbol{B}}. \tag{6.2}$$

With a Fickian diffusion approach, $\overline{\boldsymbol{\mathcal{F}}}_h^f = -\kappa_h \boldsymbol{\nabla} \overline{h}_f$, we can construct a one dimensional model of the helicity distribution

$$-\kappa_h \frac{\mathrm{d}^2 \overline{h}_f}{\mathrm{d}z^2} = S(z), \tag{6.3}$$

with the source term $S(z) \equiv -2\alpha \overline{\boldsymbol{B}}^2 + 2\eta_\mathrm{t} \mu_0 \overline{\boldsymbol{J}} \cdot \overline{\boldsymbol{B}}$. Here κ_h is the magnetic helicity diffusion coefficient (assumed constant), which is expected to be around $0.3\,\eta_\mathrm{t}$ (Hubbard and Brandenburg, 2010; Mitra et al., 2010a, and **Paper II**). In Fig. 6.12, we plot three different solutions for $\overline{h}_f$, where the source term is $S(z) = -1$ in the interior and zero outside (using arbitrary units). Depending

on the slope, which depends on κ and the boundary conditions, and the size of the domain, the helicity changes sign at different locations in the outer part. This is why in some dynamo models, we can observe a sign change, but not in all of them. In the model of **Papers IV** and **V** no clear indication of helicity sign reversal has been found. This could be related to the lower amount of magnetic helicity produce by less helical (as convective instead of forced) motions.

6.4 Discussion and conclusions

The results of **Papers I–V** show that we were able to reproduce important features of the Sun's magnetic field as well as its differential rotation with a simplified two-layer model. Combining the convection zone, where a dynamo is operating, with an overlying corona gives useful and remarkable insights about dynamo theory, the mechanism of coronal mass ejections and the magnetic helicity distribution in the Sun. We found that the dynamo is stronger in the present of the corona and shows equatorward migration. The coronal layer does not only influence the convection zone as it represents a more realistic boundary condition for the magnetic field, it also seems to promote the generation of spoke-like differential rotation. We are able to generate coronal ejections and flux emergence just by the untwisting of helical fields. We additionally show that even with kinetic helicity which is less for the convective dynamo than for a force turbulent one, coronal ejections occur. The shape of these ejections is similar to those observed in real coronal mass ejections. Most of these results have been found for the first time and suggest that they are only reproducible using a combined two-layer model.

One issue with using direct numerical simulations to model astrophysical bodies is the question, whether these models are realistic enough; and if they are not, why we should bother using them. Currently, direct numerical simulations are unable to reach realistic values of the magnetic diffusivity and fluid viscosity. Therefore, every direct simulation of a solar dynamo model is per se unrealistic. But, we can still learn a lot from these simulations. In particular, we can run them for a series of different values of magnetic and fluid Reynolds numbers and try to extrapolate the results to solar values. On the other hand, our scope is not to reproduce every little detail of the Sun with our model; we are more interested in specific models, and investigate their outcome. If we understand the results of these simplified and concededly unrealistic simulations in a proper way, it will yield great contributions to the understanding of the Sun's dynamics.

Beside the Reynolds numbers, what about the other quantities, are they consistent with solar values? The density contrast is order of magnitudes lower

than in the considered region of the Sun, which includes the entire convection zone and the corona to a large extent. The solar density changes over fourteen orders of magnitude, which is currently impossible to model in direct numerical simulations. Using tools such as non-equidistant grids might extend the contrast, but not to solar values. After all, we have improved the density contrast in our models from unity to over two thousand. Applying non-solar-like values for the density stratification in our models influences the results. In the model of **Papers I** and **II**, the density is either constant or does not play an important role in producing ejections of current helicity density. But in the models of **Papers IV** and **V**, the low stratification has a strong influence on the results. For example in **Paper IV**, the ejected flux tube shows a lower density than the surrounding plasma because of the low stratification. We expect that with a higher stratification this tube would have a higher density than the surrounding plasma in the corona, similar to observed CMEs. Also, in **Paper VI** the equatorward migration pattern depends crucial on the strength of the stratification. The luminosity, we choose in the models of **Papers IV** and **V** is much higher than the solar one. Using this, we try to compensate for the low Reynolds number regime, which make convection harder to excite. A similar argument we employ for the use of rotation rates higher than the Sun. Although the Sun might have slower convective motions than expected (Hanasoge et al., 2012), which would increase the solar Coriolis number, the Coriolis numbers we use in our models are only slightly higher than those in the Sun, although the rotation rate is three times higher. With lower magnetic Reynolds numbers and a solar-like rotation rates it is in general more difficult to excite a solar dynamo, therefore, we increase the rotation rate to compensate for the too low magnetic Reynolds number. Additionally, higher rotation rate might be not applicable to the Sun, but to other stars, where the magnetic fields are also observable.

In our combined two-layer model, we use strong simplifications to implement the combination of a convection zone and a corona in a single model. We found that there exists a dynamo solution which shows equatorward migration even in the low Reynolds number regime. The fact that a coronal layer has a strong influence on the properties inside the convection zone, may have been overestimated by the lack of realistic stratification and Reynolds numbers, but it should be taken into account in future simulations of stellar dynamo models. Helical magnetic fields can emerge, build up structures similar to CMEs, and get eventually ejected. The untwisting of magnetic fields as an alternative way to the emergence of structures should be studied further and can in the Sun also have significant importance.

Researchers, who model coronal mass ejections might criticize the lack of coronal properties in our model. The value of the plasma-β, which determines,

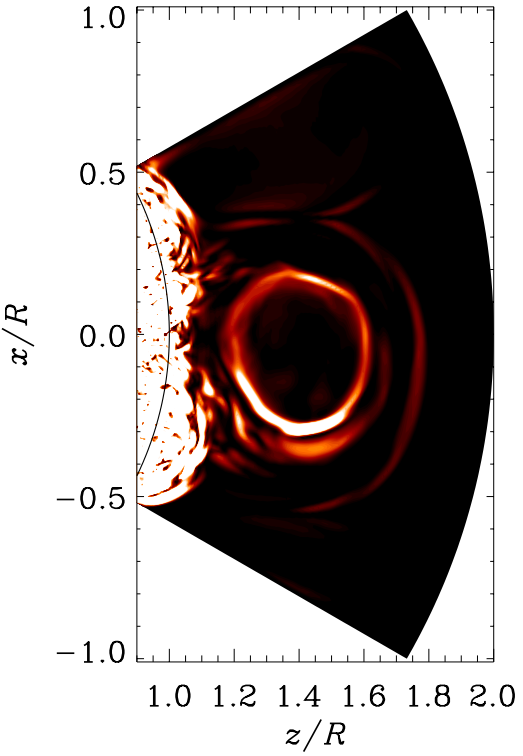

Figure 6.13: Coronal ejection plotted in terms of the Ohmic heating $\mu_0 \eta \bar{\boldsymbol{J}}^2$ of the model of **Papers II** and **III**. This ejection is the same as in the second panel of Fig. 6.9. Bright colors correspond to large values and dark to small ones. The solid black line show the location of the surface at $r^2 = x^2 + z^2 = R^2 = R_\odot^2$. Overbars indicate azimuthal averages.

whether the magnetic field follows the plasma, is not very low in our corona. In the models of **Papers II** and **IV** our corona is isothermal and has therefore a high value of plasma-β. This is a valid criticism, but not for our scope, which is to describe the magnetic properties and the magnetic structures emerging into the corona. Because the plasma-β is low in the solar corona, the magnetic structures are the important features. We do not claim to describe the fluid and plasma properties of these ejections realistically. We are interested to study the emergence of ejections of magnetic field and current helicity. In future models similar to those in **Paper V**, we will see, if a lower plasma-β changes the main magnetic properties of the ejections. Additionally, we also do not claim to describe the coronal ejections realistically, as we are more interested in the mechanism of the emergence and its connection with dynamo action.

In **Papers II** and **III**, we compare plots of current helicity density and white light images of observed CMEs and conclude that the shape of our ejections are similar to them. White light emission and current helicity are not the same quantities and comparing these two can be misleading. However, in this work, as mentioned before, we are mostly interested in CMEs as magnetic phenomena. The current helicity concentrations are emerging from the surface of our convection zone, carrying some mass with it. In a realistic simulation with high enough density stratification, the shape of the current helicity ejections would directly correspond to density enhancement and therefore emissivity. In Fig. 6.13, we plot Ohmic heating for one of the prominent ejections of the model of **Paper II**. The revealed shape shows clear similarities with the observed one of real coronal mass ejections. We claim, that the Ohmic heating can be related to the emissivity of the CMEs shown in Figs. 1.8 and 5.2.

For another aspect it is shown that a coronal layer as an upper boundary condition is important for the dynamo. Comparing Fig. 4.4 with Fig. 6.4, the evolution of the mean magnetic field shows a different behavior in cases with and without a coronal layer. Beside the different patterns of the equatorward migration in the saturated stage, the excitation times are significantly different. In the simulation without a coronal layer (Fig. 4.4), the mean magnetic field is visible after around $t/\tau = 1000$, whereas in the case with a coronal layer (Fig. 6.4), it is already visible in the very beginning of the simulation. The input parameters of the simulations are not that different leading to a similar estimation for the turnover time τ (see **Papers V** and **VI**). Additionally, the simulation without a corona have been started from a equilibrated hydrodynamical run, where the convective motions has reached a saturated state. In the model with a corona the simulations have been started from the hydrostatic reference solution without any convective motions. This fact together with the similarity of the input parameters suggest that the coronal layer has a strong influence on the excitation of the large-scale dynamo. To express it in a different way: the radial field boundary condition at the surface of the convection zone is very restrictive and can change the dynamo evolution in the convection zone significantly. However, to have clear evidence for this, we have to perform more simulations both with and without a coronal later, whereas the other parameters are held exactly the same.

Overall, this two-layer model is an excellent model to study the corona-dynamo interaction as well as the ejection of magnetic helicity and mass from the convection zone through the corona into the interstellar space.

7. Possible Future Developments

My goal is simple.
It is a complete understanding of the universe,
why it is as it is and why it exists at all.

Stephen Hawkins

This combined two-layer model as described in § 6 is a rich model, which can be used in many ways for many different purposes. Let me outline here a few possibilities.

7.1 Solar dynamo and helicity fluxes

Measuring and modeling magnetic helicity fluxes is an important element in understanding the solar dynamo. The combined two-layer model provides a straightforward approach to quantify how much magnetic helicity flux is needed for the solar dynamo. It would be important to determine its influence on the equatorward migration of the mean magnetic field found in the model of Käpylä et al. (2012). This would involve a study of magnetic helicity fluxes and mean magnetic fields generated by a convective dynamo using mono- and bi-layer models. In this context, investigating also the differential rotation in these simulations would be beneficial. However, a general understanding of the dynamo and convection mechanism generating equatorward migration and spoke-like differential rotation will only be possible by calculating the transport coefficients of the mean-flow and mean magnetic field by using approaches like the test-field method (Schrinner et al., 2007). Although rudimentary approaches have already been used (Racine et al., 2011), but their outcome is limited by neglecting the turbulent diffusivity tensor. The obtained transport coefficients can then be used in mean-field models of the solar dynamo. The predictive power of those models and their Reynolds number dependence will first be compared with DNS and those models will then be applied to magnetic Reynolds numbers closer to those of the Sun.

7.2 Convection driven coronal mass ejections

In the work of **Papers I, II** and **IV**, we could show that a dynamo below the surface can drive coronal ejections, which have a similar shape as observed

CMEs and magnetic clouds. But these models have been performed using strong simplifications, in particular in describing the coronal layer. The coronal temperature, for example, is set to the value of the surface by applying a prescribed cooling function. This led to a much higher plasma-β in our modeled corona, than in the solar one. It would be a good project to develop a realistic coronal stratification in a bi-layer model of dynamo-driven coronal mass ejection. This includes a realistic treatment of density and temperature profiles, a self-consistent coronal heating mechanism, background coronal field structures as well as solar wind interactions. Step by step, one can include more improvements in describing the coronal layer, starting with steeper temperature and density profiles. One step would be including a realistic treatment of heat conductivity similar as in the work by Bingert and Peter (2011), where it leads to self-consistently generated coronal heating due to field line braiding at the footpoints. Already these improvements will give important insights about comparing self-consistent granulation motions with granulation velocity drivers as used by Bingert and Peter (2011). Additionally, one can investigate in what extend the coronal heating is affected by ejections. As a third step one can impose coronal background fields and investigate, how the ejection are influenced or even triggered by this field as shown by, e.g. Fan and Gibson (2004). Due to numerical reasons, in the models of **Papers I, II** and **IV**, we apply closed radial boundaries, i.e. no mass flux can leave the domain. Therefore a Parker solution of the solar wind is prohibited. To study the interaction of the solar wind and coronal ejections would be a useful extension on the model. A Cartesian bi-layer will give useful insights about driven coronal mass ejections. However, this model can be extended to a global spherical model to study the coronal mass ejections as well as their interplay with the global coronal field. There, the Parker wind has a solution and can be generated self-consistently.

7.3 Space weather forecasting

A CME takes about one to five days to reach the Earth, see § 1.5 and § 5. This time interval defines the maximum advance warning time for magnetic storm events to happen. The prediction time could be extended using more realistic models and new methods. The idea is to use the data assimilation technique to forecast space weather. This is similar to weather forecast on Earth where measurements of certain quantities at stations around the world are included into the model. Each time new data are read in, the parameters of the model will be adjusted. By running an ensemble of models with different parameters, one is able to give probabilities of the resulting outcomes. Recently, there were attempts to use these methods for the forecast of the solar activity cycle (see, e.g., Dikpati and Anderson, 2012). It would be very interesting to apply the

data assimilation and forecast techniques to my dynamo-driven coronal ejection model to develop a solar space weather forecast. This will involve the improvement of the ejection model, including solar wind fluctuations as well as low plasma β effects. Additionally, time should be spend on collecting observational data of ejections and preparing them to be accessible for the model. Pinning down the crucial parameters of the ejection model with observed data will be a first step. In a second step the actual forecasting can be done.

Sammanfattning

Observationer visar att koronamassutkastningar är förknippade med vridna magnetfältskonfigurationer. Koronamassutkastningar brukar vanligtvis modelleras genom att man skjuvar och vrider fotpunkterna för en viss distribution av magnetiskt flöde vid solytan och sedan låter den tidsutvecklas på ytan. Ythastigheterna och de magnetiska fältmönstren borde naturligtvis i första hand erhållas från realistiska simuleringar av solens konvektionszon där fältet genereras genom dynamoverkan. Därför behövs en enhetlig hantering av konvektionszonen och koronamassutkastningar. Numeriska simuleringar av turbulenta dynamos visar att förstärkningen av magnetfält kan dämpas genom s.k. "catastrophic quenching" vid magnetiska Reynoldstal som är typiska för solens inre. Ett starkt flöde av magnetisk helicitet från dynamoområdet can mildra denna dämpning. I denna mening är ett realistiskt (magnetiskt) randvillkor en viktig ingrediens för en framgångsrik soldynamomodell.

Med hjälp av den tvålagermodell som utvecklas i avhandlingen kombinerar vi en dynamoaktiv område med ett magnetiskt “passivt” men effektivt ledande övre lager som modellerar solens korona. I fyra steg förbättras denna uppställning från en tvingad turbulent till en konvektivt driven dynamo och från en isoterm till en polytropt stratifierad korona. Simuleringarna uppvisar magnetiska fält som uppstår vid dynamo områdes yta och sedan kastas in i domänens korona. Deras morfologi låter oss associera sådana händelser med koronamassutkastningar. Den magnetiska heliciteten visar sig ändra tecken i koronan och är förenlig med nyligen utförda helicitetsmätningar i solvinden. Vår konvektionsdrivna dynamomodell med en yttre korona har en sol-liknande differentiell rotation med radiella (eker-lika) konturer av konstant rotationshastighet, samt en sol-lik meridionell cirkulation och ett ytnära skjuvningslager. Den eker-lika rotationsprofilen härrör från en longitudinell entropigradient som bryter Taylor-Proudmanbalansen genom den barokliniska termen. Vi observerar genomsnittliga magnetiska fält som migrerar mot ekvatorn både i modeller med och utan koronalagret. Ett anmärkningsvärt resultat är att dynamoverkan gynnas avsevärt av närvaron av en korona som är starkare och mer realistisk.

Tvålagermodellen representerar en ny ansats för att på ett självkonsistent sätt beskriva hur koronamassutkastningarna skapas. Dessutom har den en stor betydelse för soldynamomodeller eftersom den återger många magnetiska företeelser som observerats i solen.

Zusammenfassung

Beobachtungen zeigen, dass koronale Massenauswürfe mit verdrillten magnetische Flußkonfigurationen verbunden sind. Üblicherweise werden koronale Massenauswürfe mit Hilfe von Scherung und Verdrillung von Fußpunkten einer vorgebenen magnetischen Flußverteilung und deren Entwicklung an der Oberfläche modelliert. Letztlich sollten jedoch die Oberflächengeschwindigkeiten und die Magnetfeldstrukturen aus realitischen Sonnenkonvektionssimulationen entnommen werden, in denen das Feld von einem Dynamoprozess erzeugt wird. Deshalb bedarf es einer vereinheitlichten Behandlung der Konvektionszone der Sonne and koronaler Massenauswürfe. Numerische Simulationen turbulenter Dynamos zeigen, dass die Verstärkung von Magnetfeldern für sonnentypische magnetische Reynoldszahlen drastisch unterdrückt wird. Ein starker magnetischer Helizitätsfluß, der das Dynamogebiet verlässt, kann diese Unterdrückung abmildern. In diesem Sinne is eine realistische (magnetische) Randbedingung ein sehr wichtiger Bestandteil eines erfolgreichen Modells für den Sonnendynamo.

Das in dieser Doktorarbeit entwickelte zweischichtige Modell, verbindet eine dynamoaktive Schicht mit einer darüber liegenden Schicht, die zwar dynamoinaktiv, aber stark leitfähig ist, sie imitiert die Korona der Sonne. In vier Schritten vervollkommnen wir den Simulationsaufbau von einem erzwungen turbulenten zu einem von Konvektion getriebenen Dynamo und von einer isothermen zu einer polytrop geschichteten Korona. Die Simulationen bringen Magnetfelder hervor, die aus dem Dynamogebiet aufsteigen und aus dem koronalen Teil des Simulationsgebiets ausgestoßen werden. Wegen deren morphologischer Form interpretieren wir diese Ereignisse als koronale Massenauswürfe. Im Ergebnis zeigt sich, dass die magnetische Helizität ihr Vorzeichen in der Korona ändert und daher mit kürzlich gemessenen Helizitätswerten aus dem Sonnenwind übereinstimmt. Unser von Konvektion getriebenes Dynamomodel mit koronaler Hülle besitzt eine sonnenähliche differentielle Rotation mit radialen (speichenähnlichen) Isolinien konstanter Winkelgeschwindigkeit sowie eine sonnenähnliche meridionale Zirkulation und einer oberflächennahen Scherschicht. Das speichenähnliche Profil der Rotation lässt sich auf den latitudinalen Entropiegradienten zurückführen, der mit Hilfe der Baroklinität das Taylor–Proudman–Gleichgewicht verletzt. Sowohl in Modellen mit als auch ohne koronaler Schicht finden wir ein mittleres Magnetfeld, das zum Äquator wandert. Ein beachtenswertes Ergebnis ist, dass der Dynamoprozess

durch das Vorhandensein der Korona erheblich begünstig und somit stärker und realistischer wird.

Das zweischichtige Modell stellt einen neuen Ansatz dar, die Erzeugung koronaler Massenauswürfe in einer selbstkonsistenten Weise zu beschreiben. Auf der anderen Seite hat es wichtige Konsequenzen für Sonnendynamomodelle, da es viele magnetische Phänomene, die auf der Sonne beobachtet werden, wiedergibt.

Acknowledgments

The first thanks is dedicated to my supervisor **Axel Brandenburg**, the most efficient person I have ever met. I learned from him the broadness and deepness of astrophysics, and that only deepness will give you broadness. He encouraged me to fulfill my own ideas, which then often resulted in collaborations and publications. I am very thankful for his intensive support and supervision to help me to become a good scientist, including BBQs and nitrogen ice cream. I also would like to give a big thanks to my close collaborators **Petri J. Käpylä** and **Maarit J. Mantere**. I enjoyed the visits to Helsinki, the long (not entirely) scientific discussions via Skype and the Sauna parties. I want to thank **Dhrubaditya Mitra** for his collaboration and supervision during my time in Nordita. I like his way of tackling scientific problems and his ability to explain them in such a way that his own daughter could understand it. I would like to give a thanks to **Matthias Rheinhardt**, whose knowledge in mean-field dynamos and numerics is as enormous as in human history. I enjoyed long and interesting discussions about German politics and non-equidistant grids. A big thanks is also deserved by my second supervisor **Göran Scharmer**. He not only supported me and my PhD project by, for example, forwarding every new article about CMEs, but he also made it possible for me to go to La Palma and observe sunspots with the SST. I think he is one of the great solar physicists of our time, and I thank him for being part of my supervision. I would also like to thank my mentor **Claes-Ingvar Björnsson** in taking care for me having a smooth sailing, and **Garrelt Mellema** of being a mindful director for graduate studies.

I am grateful to all the people in the **Astrophysics Group** and **Nordita** in general for establishing a productive and supportive scientific environment. This includes persons such as **Hans**, who helps with computer problems, Swedish translations and all the little things no one thinks about. I would like to thank the **Astronomy Department** especially **Göran Östlin** and **Sandra** for creating such a nice and warm atmosphere for my PhD studies.

A special thanks goes to my three *Roomies*, **Koen**, **Simon** and **Fabio**, who unfortunately left me alone this March. I was very happy to be able to share my office and trips through North America, South America, Asia and Europe with you guys. And remember: *the wine is too pink*! At this point, I would also acknowledge all the nice conferences (Krakow, Nice, Naxos, Ventura, Teistungen, Rhodes, Mendoza and Beijing), including travel grants supported by the International Astronomy Union as well as the C F Liljevalchs Foundation, the K&A Wallenberg Foundation, and the High Performance Computing-

EUROPA2 Project.

There have been many people in and around Nordita and the Department of Astronomy, whose presence I enjoyed very much. They are (without any preferential order): **Oliver, Sarah, Gianni, Illa, Cecilia, Gustavo, Piyali, Hiva, Saghar, Vasco, Jaime, Hannes, Andreas, Florent, Emanuel, Thørger, Lucia, Genoeva, Katia, Fernanda, Alessandro, Francesco, Gautam, Mikael** and **Laia**. Others have already left, but are still important friends, like **Javier&Claire, Martina, Nuria&Antonio** and **Angela&Arjan**. Thanks to **Sidney, Leili** and **Elliot Maxwell**, as my family in Stockholm.

A grateful thanks deserves my Family in Germany, my parents **Reinhard und Gabi** with their unconditional support and love, as well as **Lars und Steffi** and my grandparents **Hannelore und Gerd** and **Anni und Lothar** for they unappeasable interest in my life and my work.

At last, but most important, I wish thank to **Atefeh**. Your love, your kindness and your naturalness have made my last two and a half years the best of my life. Doset Daram, Atijunam!

At the end, I would also like to thank all my friends in Stockholm, in Germany and all around the World. *Tack! Danke! Thank you!*

Publications not included in the Thesis

Conference proceedings

I **Warnecke, J.**, & Brandenburg, A.: 2011, "Recurrent flux emergence from dynamo-generated fields", in *Astrophysical Dynamics: from Stars to Galaxies*, ed. N. Brummell, A. S. Brun, M. S. Miesch, & Y. Ponty, Proc. IAU Symp., **Vol. 271**, pp. 407-408

II **Warnecke, J.**, & Brandenburg, A.: 2011, "Dynamo generated field emergence through recurrent plasmoid ejections", in *Physics of Sun and Star Spots*, ed. D. P. Choudhary & K. G. Strassmeier, Proc. IAU Symp., **Vol. 273**, pp. 256-260

III **Warnecke, J.**, Brandenburg, A., & Mitra, D.: 2011, "Plasmoid ejections driven by dynamo action underneath a spherical surface", in *Advances in Plasma Astrophysics*, ed. A. Bonanno, E. de Gouveia dal Pino, & A. Kosovichev, Proc. IAU Symp., **Vol. 274**, pp. 306-309

IV **Warnecke, J.**, Käpylä, P. J., Mantere, M. J., & Brandenburg, A.: 2012, "Coronal ejections from convective spherical shell dynamos", in *Comparative Magnetic Minima: Characterizing quiet times in the Sun and stars*, ed. C. H. Mandrini & D. F. Webb, Proc. IAU Symp., **Vol. 286**, pp. 154-158

V **Warnecke, J.**, Käpylä, P. J., P. J., Mantere, M. J., & Brandenburg, A.: 2012, "Solar-like differential rotation and equatorward migration in a convective dynamo with a coronal envelope", in *Solar and astrophysical dynamos and magnetic activity*, ed. A. Kosovichev, Proc. IAU Symp., **Vol. 294**, in press

Bibliography

C. E. Alissandrakis. On the computation of constant alpha force-free magnetic field. *Astron. Astrophys.*, 100:197–200, 1981. 30

T. Amari, J.F. Luciani, Z. Mikić, and J. Linker. A twisted flux rope model for coronal mass ejections and two-ribbon flares. *Astrophys. J. Lett.*, 529:L49–L52, 2000. 54

S. K. Antiochos, C. R. DeVore, and J. A. Klimchuk. A Model for Solar Coronal Mass Ejections. *Astrophys. J.*, 510:485–493, 1999. 52

M. J. Aschwanden, A. Winebarger, D. Tsiklauri, and H. Peter. The coronal heating paradox. *Astrophys. J.*, 659:1673–1681, 2007. 7

H.W. Babcock. The topology of the sun's magnetic field and the 22-year cycle. *Astrophys. J.*, 133:572–589, 1961. 41

S. L. Baliunas, R. A. Donahue, W. H. Soon, J. H. Horne, J. Frazer, L. Woodard-Eklund, M. Bradford, L. M. Rao, O. C. Wilson, Q. Zhang, W. Bennett, J. Briggs, S. M. Carroll, D. K. Duncan, D. Figueroa, H. H. Lanning, T. Misch, J. Mueller, R. W. Noyes, D. Poppe, A. C. Porter, C. R. Robinson, J. Russell, J. C. Shelton, T. Soyumer, A. H. Vaughan, and J. H. Whitney. Chromospheric variations in main-sequence stars. *Astrophys. J.*, 438:269–287, 1995. 2

G. Baumann, K. Galsgaard, and Å. Nordlund. 3D Solar Null Point Reconnection MHD Simulations. *Solar Phys.*, page 291, 2012. 54

S. Bingert and H. Peter. Intermittent heating in the solar corona employing a 3D MHD model. *Astron. Astrophys.*, 530:A112, 2011. 7, 13, 30, 50, 80

S. Bingert and H. Peter. Nanoflare statistics in an active region 3D MHD coronal model. *Astron. Astrophys.*, 550:A30, 2013. 50

E. G. Blackman and A. Brandenburg. Doubly Helical Coronal Ejections from Dynamos and Their Role in Sustaining the Solar Cycle. *Astrophys. J. Lett.*, 584:L99–L102, 2003. 51, 56

E. G. Blackman and G. B. Field. Constraints on the Magnitude of α in Dynamo Theory. *Astrophys. J.*, 534:984–988, 2000. 36, 56

A. Brandenburg. The Case for a Distributed Solar Dynamo Shaped by Near-Surface Shear. *Astrophys. J.*, 625:539–547, 2005. 39, 40, 42, 47

A. Brandenburg. Nonlinear Small-scale Dynamos at Low Magnetic Prandtl Numbers. *Astrophys. J.*, 741:92, 2011. 44

A. Brandenburg and W. Dobler. Large scale dynamos with helicity loss through boundaries. *Astron. Astrophys.*, 369:329–338, 2001. 36

A. Brandenburg and C. Sandin. Catastrophic alpha quenching alleviated by helicity flux and shear. *Astron. Astrophys.*, 427:13–21, 2004. 56

A. Brandenburg and K. Subramanian. Astrophysical magnetic fieds and nonlinear dynamo theory. *Physics Reports*, 417:1–209, 2005. 31, 32, 35, 36, 37, 56

A. Brandenburg, D. Moss, and I. Tuominen. Stratification and thermodynamics in mean-field dynamos. *Astron. Astrophys.*, 265:328–344, 1992. 24, 47

A. Brandenburg, S. H. Saar, and C. R. Turpin. Time Evolution of the Magnetic Activity Cycle Period. *Astrophys. J. Lett.*, 498:L51, 1998. 2

A. Brandenburg, S. Candelaresi, and P. Chatterjee. Small-scale magnetic helicity losses from a mean-field dynamo. *Month. Not. Roy. Astron. Soc.*, 398:1414–1422, 2009. 56

A. Brandenburg, P. Chatterjee, F. Del Sordo, A. Hubbard, P. J. Käpylä, and M. Rheinhardt. Turbulent transport in hydromagnetic flows. *Physica Scripta Volume T*, 142: 014028, 2010. 43

A. Brandenburg, K. Kemel, N. Kleeorin, D. Mitra, and I. Rogachevskii. Detection of Negative Effective Magnetic Pressure Instability in Turbulence Simulations. *Astrophys. J. Lett.*, 740:L50, 2011a. 40

A. Brandenburg, K. Subramanian, A. Balogh, and M. L. Goldstein. Scale Dependence of Magnetic Helicity in the Solar Wind. *Astrophys. J.*, 734:9, 2011b. 73

A. Brandenburg, D. Sokoloff, and K. Subramanian. Current Status of Turbulent Dynamo Theory. From Large-Scale to Small-Scale Dynamos. *Spa. Sci. Rev.*, 169: 123–157, 2012. 37

B. P. Brown, M. K. Browning, A. S. Brun, M. S. Miesch, and J. Toomre. Rapidly Rotating Suns and Active Nests of Convection. *Astrophys. J.*, 689:1354–1372, 2008. 45, 63

B. P. Brown, M. K. Browning, A. S. Brun, M. S. Miesch, and J. Toomre. Persistent Magnetic Wreaths in a Rapidly Rotating Sun. *Astrophys. J.*, 711:424–438, 2010. 45

B. P. Brown, M. S. Miesch, M. K. Browning, A. S. Brun, and J. Toomre. Magnetic Cycles in a Convective Dynamo Simulation of a Young Solar-type Star. *Astrophys. J.*, 731:69, 2011. 45, 64

A. S. Brun, M. S. Miesch, and J. Toomre. Global-Scale Turbulent Convection and Magnetic Dynamo Action in the Solar Envelope. *Astrophys. J.*, 614:1073–1098, 2004. 45, 63, 64

A. S. Brun, M. S. Miesch, and J. Toomre. Modeling the Dynamical Coupling of Solar Convection with the Radiative Interior. *Astrophys. J.*, 742:79, 2011. 47, 64, 67

P. Caligari, F. Moreno-Insertis, and M. Schussler. Emerging flux tubes in the solar convection zone. 1: Asymmetry, tilt, and emergence latitude. *Astrophys. J.*, 441: 886–902, 1995. 41

R. C. Carrington. Description of a Singular Appearance seen in the Sun on September 1, 1859. *Month. Not. Roy. Astron. Soc.*, 20:13–15, 1859. 49, 50

F. Cattaneo. On the origin of magnetic fields in the quiet photosphere. *Astrophys. J. Lett.*, 515:L39–L42, 1999. 44

F. Cattaneo and D. W. Hughes. Nonlinear saturation of the turbulent α effect. *Phys. Rev. Lett. E*, 54:4532, 1996. 36

P. Charbonneau. Dynamo Models of the Solar Cycle. *Living Reviews in Solar Physics*, 7:3, 2010. 31, 37, 41, 42

P. Charbonneau. *Solar and Stellar Dynamos*. Springer-Verlag Berlin Heidelberg, 2013. 37

P. F. Chen. Coronal Mass Ejections: Models and Their Observational Basis. *Living Reviews in Solar Physics*, 8:1, 2011. 49

M. C. M. Cheung, M. Schüssler, T. D. Tarbell, and A. M. Title. Solar Surface Emerging Flux Regions: A Comparative Study of Radiative MHD Modeling and Hinode SOT Observations. *Astrophys. J.*, 687:1373–1387, 2008. 41

A. R. Choudhuri. *The Physics of Fluids and Plasmas : An Introduction for Astrophysicists*. Cambridge University Press, 1998. 15

A. R. Choudhuri and P. A. Gilman. The influence of the Coriolis force on flux tubes rising through the solar convection zone. *Astrophys. J.*, 316:788–800, 1987. 42

E. W. Cliver, V. Boriakoff, and K. H. Bounar. The 22-year cycle of geomagnetic and solar wind activity. *J. Geophys. Res.*, 101:27091–27110, 1996. 10

F. Del Sordo, G. Guerrero, and A. Brandenburg. Turbulent dynamos with advective magnetic helicity flux. *Month. Not. Roy. Astron. Soc.*, 429:1686–1694, 2013. 36

E. Devlen, A. Brandenburg, and D. Mitra. A mean field dynamo from negative eddy diffusivity. *ArXiv:1212.2626*, 2012. 33

R. H. Dicke. Is there a chronometer hidden deep in the sun. *Nature*, 276:676–680, 1978. 9

M. Dikpati and J. L. Anderson. Evaluating Potential for Data Assimilation in a Flux-transport Dynamo Model by Assessing Sensitivity and Response to Meridional Flow Variation. *Astrophys. J.*, 756:20, 2012. 80

M. Dikpati and P. Charbonneau. A Babcock-Leighton Flux Transport Dynamo with Solar-like Differential Rotation. *Astrophys. J.*, 518:508–520, 1999. 39, 42

W. Dobler, M. Stix, and A. Brandenburg. Magnetic Field Generation in Fully Convective Rotating Spheres. *Astrophys. J.*, 638:336–347, 2006. 60

V. Domingo, B. Fleck, and A. I. Poland. The SOHO Mission: an Overview. *Solar Phys.*, 162:1–37, 1995. 49

Y. Fan and S. E. Gibson. Numerical Simulations of Three-dimensional Coronal Magnetic Fields Resulting from the Emergence of Twisted Magnetic Flux Tubes. *Astrophys. J.*, 609:1123–1133, 2004. 53, 80

Y. Fan and S. E. Gibson. Onset of Coronal Mass Ejections Due to Loss of Confinement of Coronal Flux Ropes. *Astrophys. J.*, 668:1232–1245, 2007. 53

F. Fang, W. Manchester, W. P. Abbett, and B. van der Holst. Simulation of Flux Emergence from the Convection Zone to the Corona. *Astrophys. J.*, 714:1649–1657, 2010. 42

J. Feynman and A. Ruzmaikin. The Sun's Strange Behavior: Maunder Minimum or Gleissberg Cycle? *Solar Phys.*, 272:351–363, 2011. 8

T. G. Forbes and E. R. Priest. Photospheric Magnetic Field Evolution and Eruptive Flares. *Astrophys. J.*, 446:377, 1995. 52

U. Frisch. *Turbulence. The legacy of A. N. Kolmogorov.* Cambridge University Press, 1995. 18, 19, 37

G. A. Gary. Linear force-free magnetic fields for solar extrapolation and interpretation. *Astrophys. J. Suppl.*, 69:323–348, 1989. 30

M. Ghizaru, P. Charbonneau, and P. K. Smolarkiewicz. Magnetic Cycles in Global Large-eddy Simulations of Solar Convection. *Astrophys. J. Lett.*, 715:L133–L137, 2010. 45

P. A. Gilman. Dynamically consistent nonlinear dynamos driven by convection in a rotating spherical shell. II - Dynamos with cycles and strong feedbacks. *Astrophys. J. Suppl.*, 53:243–268, 1983. 45

P. A. Gilman and J. Miller. Dynamically consistent nonlinear dynamos driven by convection in a rotating spherical shell. *Astrophys. J. Suppl.*, 46:211–238, 1981. 45

G. A. Glatzmaier. Numerical simulations of stellar convective dynamos. II - Field propagation in the convection zone. *Astrophys. J.*, 291:300–307, 1985. 45

W. Gleissberg. The recent maximum of the 80-year sunspot cycle. *Kleinheubacher Berichte*, 19:661–664, 1976. 8

B. Gudiksen and Å. Nordlund. An ab initio approach to the solar coronal heating problem. *Astrophys. J.*, 618:1020–1030, 2005a. 7, 13, 30

B. Gudiksen and Å. Nordlund. An ab initio approach to solar coronal loops. *Astrophys. J.*, 618:1031–1038, 2005b. 30

G. Guerrero and P. J. Käpylä. Dynamo action and magnetic buoyancy in convection simulations with vertical shear. *Astron. Astrophys.*, 533:A40, 2011. 42, 44

G. E. Hale. On the Probable Existence of a Magnetic Field in Sun-Spots. *Astrophys. J.*, 28:315, 1908. 8

G. E. Hale, F. Ellerman, S. B. Nicholson, and A. H. Joy. The Magnetic Polarity of Sun-Spots. *Astrophys. J.*, 49:153, 1919. 8, 9

S. M. Hanasoge, T. L. Duvall, and K. R. Sreenivasan. Anomalously weak solar convection. *Proceedings of the National Academy of Science*, 109:11928–11932, 2012. 76

R.A. Harrison. The nature of solar flares associated with coronal mass ejection. *Astron. Astrophys.*, 304:585, 1995. 49

J. W. Harvey, F. Hill, R. P. Hubbard, J. R. Kennedy, J. W. Leibacher, J. A. Pintar, P. A. Gilman, R. W. Noyes, A. M. Title, J. Toomre, R. K. Ulrich, A. Bhatnagar, J. A. Kennewell, W. Marquette, J. Patron, O. Saa, and E. Yasukawa. The Global Oscillation Network Group (GONG) Project. *Science*, 272:1284–1286, 1996. 3

D. H. Hathaway. The Sun's Shallow Meridional Circulation. *arXiv:1103.1561*, 2011. 4, 43

R. Hodgson. On a curious Appearance seen in the Sun. *Month. Not. Roy. Astron. Soc.*, 20:15–16, 1859. 49

L.L. House, W.J. Wagner, E. Hildner, C. Sawyer, and H.U. Schmidt. Studies of the corona with the solar maximum mission coronagraph/polarimeter. *Astrophys. J. Lett.*, 244:L117–L121, 1981. 50

A. Hubbard and A. Brandenburg. Magnetic helicity fluxes in an $\alpha 2$ dynamo embedded in a halo. *Geophysical and Astrophysical Fluid Dynamics*, 104:577–590, 2010. 74

A. Hubbard, F. Del Sordo, P. J. Käpylä, and A. Brandenburg. The α effect with imposed and dynamo-generated magnetic fields. *Month. Not. Roy. Astron. Soc.*, 398:1891–1899, 2009. 43

H.S. Hudson, L.W. Acton, and S.L. Freeland. A long-duration solar flare with mass ejection and global consequences. *Astrophys. J.*, 470:629, 1996. 51

R.M.E. Illing and A.J. Hundhausen. Observation of a coronal transient from 1.2 to 6 solar radii. *J. Geophys. Res.*, 90:275–282, 1985. 51, 70

H. Jeffrey. The stability of a layer of fluid heated below. *Phil. Mag.*, 2:833–844, 1926. 15

M. L. Kaiser, T. A. Kucera, J. M. Davila, O. C. St. Cyr, M. Guhathakurta, and E. Christian. The STEREO Mission: An Introduction. *Spa. Sci. Rev.*, 136:5–16, 2008. 50

P. J. Käpylä, M. J. Korpi, and I. Tuominen. Local models of stellar convection:. Reynolds stresses and turbulent heat transport. *Astron. Astrophys.*, 422:793–816, 2004. 47

P. J. Käpylä, M. J. Korpi, M. Ossendrijver, and M. Stix. Magnetoconvection and dynamo coefficients. III. α-effect and magnetic pumping in the rapid rotation regime. *Astron. Astrophys.*, 455:401–412, 2006a. 40, 43

P. J. Käpylä, M. J. Korpi, and I. Tuominen. Solar dynamo models with α-effect and turbulent pumping from local 3D convection calculations. *Astron. Nachr.*, 327:884, 2006b. 39, 40

P. J. Käpylä, M. J. Korpi, and A. Brandenburg. Large-scale dynamos in turbulent convection with shear. *Astron. Astrophys.*, 491:353–362, 2008. 44, 67

P. J. Käpylä, M. J. Korpi, A. Brandenburg, D. Mitra, and R. Tavakol. Convective dynamos in spherical wedge geometry. *Astron. Nachr.*, 331:73, 2010. 22, 45, 46, 60

P. J. Käpylä, M. J. Mantere, and A. Brandenburg. Effects of stratification in spherical shell convection. *Astron. Nachr.*, 332:883, 2011a. 61

P. J. Käpylä, M. J. Mantere, G. Guerrero, A. Brandenburg, and P. Chatterjee. Reynolds stress and heat flux in spherical shell convection. *Astron. Astrophys.*, 531:A162, 2011b. 46, 60, 67

P. J. Käpylä, M. J. Mantere, and A. Brandenburg. Cyclic Magnetic Activity due to Turbulent Convection in Spherical Wedge Geometry. *Astrophys. J. Lett.*, 755:L22, 2012. 46, 47, 61, 64, 65, 67, 79

B. B. Karak. Importance of Meridional Circulation in Flux Transport Dynamo: The Possibility of a Maunder-like Grand Minimum. *Astrophys. J.*, 724:1021–1029, 2010. 42

R. Kippenhahn. Differential Rotation in Stars with Convective Envelopes. *Astrophys. J.*, 137:664, 1963. 23

R. Kippenhahn and A. Weigert. *Stellar Structure and Evolution*. 1990. 23

L. L. Kitchatinov and M. V. Mazur. Stability and equilibrium of emerged magnetic flux. *Solar Phys.*, 191:325–340, 2000. 40

L. L. Kitchatinov and S. V. Olemskoy. Solar Dynamo Model with Diamagnetic Pumping and Nonlocal α-Effect. *Solar Phys.*, 276:3–17, 2012. 39

L. L. Kitchatinov and G. Rüdiger. Differential rotation in solar-type stars: revisiting the Taylor-number puzzle. *Astron. Astrophys.*, 299:446, 1995. 24

L. L. Kitchatinov and G. Rüdiger. Differential rotation and meridional flow in the solar convection zone and beneath. *Astron. Nachr.*, 326:379–385, 2005. 24, 47

N. I. Kleeorin and A. A. Ruzmaikin. Dynamics of the average turbulent helicity in a magnetic field. *Magnetohydrodynamics*, 18:116, 1982. 35

H. Köhler. Differential Rotation Caused by Anisotropic Turbulent Viscosity. *Solar Phys.*, 13:3–18, 1970. 24

A. G. Kosovichev and J. O. Stenflo. Tilt of emerging bipolar magnetic regions on the Sun. *Astrophys. J. Lett.*, 688:L115–L118, 2008. 43

F. Krause and K.-H. Rädler. *Mean-field Magnetohydrodynamics and Dynamo Theory*. Pergamon Press, Oxford, 1980. 32, 38

M. Küker and M. Stix. Differential rotation of the present and the pre-main-sequence Sun. *Astron. Astrophys.*, 366:668–675, 2001. 24

P. Lantos. Radiation doses received on-board aeroplanes during large solar flares. *Hvar Observatory Bulletin*, 27:171–178, 2003. 11

R.B. Leighton. Transport of magnetic fields on the sun. *Astrophys. J.*, 140:1547–1562, 1964. 41

R. H. Levine, M. Schulz, and E. N. Frazier. Simulation of the magnetic structure of the inner heliosphere by means of a non-spherical source surface. *Solar Phys.*, 77: 363–392, 1982. 59

Y. Li, J. G. Luhmann, B. J. Lynch, and E. K. J. Kilpua. Cyclic Reversal of Magnetic Cloud Poloidal Field. *Solar Phys.*, 270:331–346, 2011. 51, 72

J. H. Lienhard. *Synopsis of lift, drag, and vortex frequency data for rigid circular cylinders.* Washington State University, 1966. 18

B. C. Low. Coronal mass ejections and magnetic helicity. In J. J. Hunt, editor, *Solar Dynamic Phenomena and Solar Wind Consequences, the Third SOHO Workshop*, volume 373 of *ESA Special Publication*, page 123, 1994. 51

B. C. Low. Solar activity and the corona. *Solar Phys.*, 167:217–265, 1996. 51, 70

B. C. Low. Coronal mass ejections, flares, and prominences. In S. R. Habbal, R. Esser, J. V. Hollweg, and P. H. Isenberg, editors, *Solar Wind 9*, page 109. AIP CP471, 1999. 10

B. C. Low. Coronal mass ejections, magnetic flux ropes, and solar magnetism. *J. Geophys. Res.*, 106:25141–25164, 2001. 51

F.-J. Lübken, U. Berger, and G. Baumgarten. Stratospheric and solar cycle effects on long-term variability of mesospheric ice clouds. *J. Geophys. Res.*, 114:A11, 2009. 10

K.B. MacGregor and P. Charbonneau. Solar interface dynamos. i. linear, kinematic models in cartesian geometry. *Astrophys. J.*, 486:484–501, 1997. 39

H. Maehara, T. Shibayama, S. Notsu, Y. Notsu, T. Nagao, S. Kusaba, S. Honda, D. Nogami, and K. Shibata. Superflares on solar-type stars. *Nature*, 485:478–481, 2012. 50

W. H. Matthaeus, M. L. Goldstein, and C. Smith. Evaluation of magnetic helicity in homogeneous turbulence. *Phys. Rev. Lett.*, 48:1256–1259, 1982. 73

J. C. Maxwell. A dynamical theory of the electromagnetic field. *Royal Society Transactions*, 155:459–512, 1865. 27

M. Meneguzzi and A. Pouquet. Turbulent dynamos driven by convection. *Journal of Fluid Mechanics*, 205:297–318, 1989. 44

M. S. Miesch, A. S. Brun, and J. Toomre. Solar Differential Rotation Influenced by Latitudinal Entropy Variations in the Tachocline. *Astrophys. J.*, 641:618–625, 2006. 47, 64, 67

M. S. Miesch, N. A. Featherstone, M. Rempel, and R. Trampedach. On the Amplitude of Convective Velocities in the Deep Solar Interior. *Astrophys. J.*, 757:128, 2012. 43

Z. Mikic, D. C. Barnes, and D. D. Schnack. Dynamical evolution of a solar coronal magnetic field arcade. *Astrophys. J.*, 328:830–847, 1988. 59

D. Mitra, R. Tavakol, A. Brandenburg, and D. Moss. Turbulent Dynamos in Spherical Shell Segments of Varying Geometrical Extent. *Astrophys. J.*, 697:923–933, 2009. 57

D. Mitra, S. Candelaresi, P. Chatterjee, R. Tavakol, and A. Brandenburg. Equatorial magnetic helicity flux in simulations with different gauges. *Astron. Nachr.*, 331: 130, 2010a. 74

D. Mitra, R. Tavakol, P. J. Käpylä, and A. Brandenburg. Oscillatory Migrating Magnetic Fields in Helical Turbulence in Spherical Domains. *Astrophys. J. Lett.*, 719: L1–L4, 2010b. 45, 62

D. Mitra, D. Moss, R. Tavakol, and A. Brandenburg. Alleviating α quenching by solar wind and meridional flows. *Astron. Astrophys.*, 526:A138, 2011. 36

Y. Nakagawa and M. A. Raadu. On Practical Representation of Magnetic Field. *Solar Phys.*, 25:127–135, 1972. 30

N. J. Nelson, B. P. Brown, A. S. Brun, M. S. Miesch, and J. Toomre. Magnetic Wreaths and Cycles in Convective Dynamos. *Astrophys. J.*, 762:73, 2013. 45, 47, 63, 64, 67

Å. Nordlund, A. Brandenburg, R. L. Jennings, M. Rieutord, J. Ruokolainen, R. F. Stein, and I. Tuominen. Dynamo action in stratified convection with overshoot. *Astrophys. J.*, 392:647–652, 1992. 44

R. W. Noyes, L. W. Hartmann, S. L. Baliunas, D. K. Duncan, and A. H. Vaughan. Rotation, convection, and magnetic activity in lower main-sequence stars. *Astrophys. J.*, 279:763–777, 1984. 2

S. Ortolani and D. D. Schnack. *Magnetohydrodynamics of Plasma Relaxation*. World Scientific, 1993. 59

M. Ossendrijver. The solar dynamo. *Astron. Astrophys. Rev*, 11:287–367, 2003. 31, 37, 39, 41

M. Ossendrijver, M. Stix, A. Brandenburg, and G. Rüdiger. Magnetoconvection and dynamo coefficients. II. Field-direction dependent pumping of magnetic field. *Astron. Astrophys.*, 394:735–745, 2002. 40

E. Pariat, P. Démoulin, and M. A. Berger. Photospheric flux density of magnetic helicity. *Astron. Astrophys.*, 439:1191–1203, 2005. 57

E. N. Parker. Hydromagnetic Dynamo Models. *Astrophys. J.*, 122:293, 1955. 41

E.N. Parker. A solar dynamo surface wave at the interface between convection and nonuniform rotation. *Astrophys. J.*, 408:707–719, 1993. 39

W. D. Pesnell, B. J. Thompson, and P. C. Chamberlin. The Solar Dynamics Observatory (SDO). *Solar Phys.*, 275:3–15, 2012. 50

S. P. Plunkett, A. Vourlidas, S. Šimberová, M. Karlický, P. Kotrč, P. Heinzel, Y. A. Kupryakov, W. P. Guo, and S. T. Wu. Simultaneous SOHO and Ground-Based Observations of a Large Eruptive Prominence and Coronal Mass Ejection. *Solar Phys.*, 194:371–391, 2000. 51

J. Pomoell, R. Vainio, and R. Kissmann. MHD Modeling of Coronal Large-Amplitude Waves Related to CME Lift-off. *Solar Phys.*, 253:249–261, 2008. 54

A. Pouquet, U. Frisch, and J. Leorat. Strong MHD helical turbulence and the nonlinear dynamo effect. *Journal of Fluid Mechanics*, 77:321–354, 1976. 33, 34, 43

L. Prandtl. Aufgaben der Strömungsforschung. *Naturwissenschaften*, 14:335–338, 1926. 20

E. R. Priest and T. Forbes. *Magnetic reconnection: MHD theory and applications*. Cambridge University Press, 2000. 52

É. Racine, P. Charbonneau, M. Ghizaru, A. Bouchat, and P. K. Smolarkiewicz. On the Mode of Dynamo Action in a Global Large-eddy Simulation of Solar Convection. *Astrophys. J.*, 735:46, 2011. 45, 64, 79

S. Régnier, T. Amari, and E. Kersalé. 3D Coronal magnetic field from vector magnetograms: non-constant-alpha force-free configuration of the active region NOAA 8151. *Astron. Astrophys.*, 392:1119–1127, 2002. 51

R. Rosner and N. O. Weiss. The Origin of the Solar Cycle. In K. L. Harvey, editor, *The Solar Cycle*, volume 27 of *Astronomical Society of the Pacific Conference Series*, page 511, 1992. 9

I. I. Roussev, T. G. Forbes, T. I. Gombosi, I. V. Sokolov, D. L. DeZeeuw, and J. Birn. A Three-dimensional Flux Rope Model for Coronal Mass Ejections Based on a Loss of Equilibrium. *Astrophys. J. Lett.*, 588:L45–L48, 2003. 53

G. Rüdiger. *Differential Rotation and Stellar Convection. Sun and Solar-type Stars*. Akademie Verlag, Berlin, 1989. 19, 21, 24, 25

G. Rüdiger and A. Brandenburg. A solar dynamo in the overshoot layer: cycle period and butterfly diagram. *Astron. Astrophys.*, 296:557–566, 1995. 39

D. M. Rust. Spawning and shedding helical magnetic fields in the solar atmosphere. *Geophys. Res. Lett.*, 21:241–244, 1994. 51

S. H. Saar and A. Brandenburg. Time Evolution of the Magnetic Activity Cycle Period. II. Results for an Expanded Stellar Sample. *Astrophys. J.*, 524:295–310, 1999. 2

T. Sakurai. Calculation of force-free magnetic field with non-constant α. *Solar Phys.*, 69:343–359, 1981. 30

O. I. Savun and A. I. Sladkova. Calculation of the radiation doses absorbed from the solar flare of August 4, 1972 in a near-earth orbit. *Cosmic Research*, 14:422–426, 1976. 10

H. U. Schmidt. On the Observable Effects of Magnetic Energy Storage and Release Connected With Solar Flares. *NASA Special Publication*, 50:107, 1964. 29

J. Schou, H. M. Antia, S. Basu, R. S. Bogart, R. I. Bush, S. M. Chitre, J. Christensen-Dalsgaard, M. P. di Mauro, W. A. Dziembowski, A. Eff-Darwich, D. O. Gough, D. A. Haber, J. T. Hoeksema, R. Howe, S. G. Korzennik, A. G. Kosovichev, R. M. Larsen, F. P. Pijpers, P. H. Scherrer, T. Sekii, T. D. Tarbell, A. M. Title, M. J. Thompson, and J. Toomre. Helioseismic Studies of Differential Rotation in the Solar Envelope by the Solar Oscillations Investigation Using the Michelson Doppler Imager. *Astrophys. J.*, 505:390–417, 1998. 3

C. J. Schrijver and M. L. De Rosa. Photospheric and heliospheric magnetic fields. *Solar Phys.*, 212:165–200, 2003. 59

M. Schrinner, K.-H. Rädler, D. Schmitt, M. Rheinhardt, and U. R. Christensen. Mean-field concept and direct numerical simulations of rotating magnetoconvection and the geodynamo. *Geophys. Astrophys. Fluid Dyn.*, 101:81–116, 2007. 39, 43, 65, 79

M. Schwabe. Sonnenbeobachtungen im Jahre 1843. Von Herrn Hofrath Schwabe in Dessau. *Astron. Nachr.*, 21:233, 1844. 7

R. Schwenn. Space Weather: The Solar Perspective. *Living Reviews in Solar Physics*, 3:2, 2006. 12, 55

M. Semel and J. Rayrole. Étude Critique d'un Champ Current-Free dans l'Atmosphère Solaire. In K. O. Kiepenheuer, editor, *Structure and Development of Solar Active Regions*, volume 35 of *IAU Symposium*, page 134, 1968. 29

K. Shibata and T. Magara. Solar Flares: Magnetohydrodynamic Processes. *Living Reviews in Solar Physics*, 8:6, 2011. 49

E. A. Spiegel and N. O. Weiss. Magnetic activity and variations in solar luminosity. *Nature*, 287:616, 1980. 3, 39

H. C. Spruit. A model of the solar convection zone. *Solar Phys.*, 34:277–290, 1974. 20, 21

M. Steenbeck, F. Krause, and K.-H. Rädler. Berechnung der mittleren Lorentz-Feldstärke für ein elektrisch leitendes Medium in turbulenter, durch Coriolis-Kräfte beeinflußter Bewegung. *Zeitschrift Naturforschung Teil A*, 21:369, 1966. 33

R. F. Stein. Solar Surface Magneto-Convection. *Living Reviews in Solar Physics*, 9: 4, 2012. 44

R. F. Stein and Å. Nordlund. On the Formation of Active Regions. *Astrophys. J. Lett.*, 753:L13, 2012. 40

J. O. Stenflo and A. G. Kosovichev. Bipolar magnetic regions on the Sun: global analysis of the SOHO/MDI data set. *Astrophys. J.*, 745:129, 2012. 43

D. L. Stephens, Jr., L. W. Townsend, and J. L. Hoff. Interplanetary crew dose estimates for worst case solar particle events based on historical data for the Carrington flare of 1859. *Acta Astronautica*, 56:969–974, 2005. 11

M. Stix. *The sun: an introduction*. Springer, Berlin, 2002. 1, 15, 20, 22, 29, 37, 52

P. A. Sturrock. *Solar Flares*. Colorado Associated University Press, Boulder, 1980. 52

H. Svensmark and E. Friis-Christensen. Variation of cosmic ray flux and global cloud coverage-a missing link in solar-climate relationships. *Journal of Atmospheric and Solar-Terrestrial Physics*, 59:1225–1232, 1997. 10

J. K. Thalmann, B. Inhester, and T. Wiegelmann. Estimating the Relative Helicity of Coronal Magnetic Fields. *Solar Phys.*, 272:243–255, 2011. 57

M. J. Thompson, J. Toomre, E. R. Anderson, H. M. Antia, G. Berthomieu, D. Burtonclay, S. M. Chitre, J. Christensen-Dalsgaard, T. Corbard, M. De Rosa, C. R. Genovese, D. O. Gough, D. A. Haber, J. W. Harvey, F. Hill, R. Howe, S. G. Korzennik, A. G. Kosovichev, J. W. Leibacher, F. P. Pijpers, J. Provost, E. J. Rhodes, Jr., J. Schou, T. Sekii, P. B. Stark, and P. R. Wilson. Differential Rotation and Dynamics of the Solar Interior. *Science*, 272:1300–1305, 1996. 3

M. J. Thompson, J. Christensen-Dalsgaard, M. S. Miesch, and J. Toomre. The Internal Rotation of the Sun. *Ann. Rev. Astron. Astrophys.*, 41:599–643, 2003. 3, 67

W. T. Thompson, B. Kliem, and T. Török. 3D Reconstruction of a Rotating Erupting Prominence. *Solar Phys.*, 276:241–259, 2012. 51, 56

V. S. Titov and P. Démoulin. Basic topology of twisted magnetic configurations in solar flares. *Astron. Astrophys.*, 351:707–720, 1999. 52

T. Török and B. Kliem. Confined and Ejective Eruptions of Kink-unstable Flux Ropes. *Astrophys. J. Lett.*, 630:L97–L100, 2005. 52, 53

T. Török, B. Kliem, and V. S. Titov. Ideal kink instability of a magnetic loop equilibrium. *Astron. Astrophys.*, 413:L27–L30, 2004. 52

I. Tuominen and G. Rüdiger. Solar differential rotation as a multiparameter turbulence problem. *Astron. Astrophys.*, 217:217–228, 1989. 23, 24

J. Tuominen. On Stellar Envelopes. *Annals of the New York Academy of Sciences*, 41: 61–76, 1941. 4

S. I. Vainshtein and F. Cattaneo. Nonlinear restrictions on dynamo action. *Astrophys. J.*, 393:165–171, 1992. 36

S. I. Vainshtein and Y. B. Zel'dovich. Reviews of Topical Problems: Origin of Magnetic Fields in Astrophysics (Turbulent "Dynamo" Mechanisms). *Soviet Physics Uspekhi*, 15:159–172, 1972. 31

G. Valori, P. Démoulin, and E. Pariat. Comparing Values of the Relative Magnetic Helicity in Finite Volumes. *Solar Phys.*, 278:347–366, 2012. 57

E. Vitense. Die Wasserstoffkonvektionszone der Sonne. *Zeitschr. f. Astrophys.*, 32: 135, 1953. 20, 21

A. Vögler and M. Schüssler. A solar surface dynamo. *Astron. Astrophys.*, 465:L43–L46, 2007. 44

Y.-M. Wang and N. R. Sheeley, Jr. On the Topological Evolution of the Coronal Magnetic Field During the Solar Cycle. *Astrophys. J.*, 599:1404–1417, 2003. 9

J. Warnecke. Einfluss photosphärischer Bewegungen auf die Struktur der solaren Korona. *Master Thesis*, 2009. 52, 59

D. F. Webb and T. A. Howard. Coronal Mass Ejections: Observations. *Living Reviews in Solar Physics*, 9:3, 2012. 49

T. Wiegelmann. Optimization code with weighting function for the reconstruction of coronal magnetic fields. *Solar Phys.*, 219:87–108, 2004. 30

T. Wiegelmann. Nonlinear force-free modeling of the solar coronal magnetic field. *J. Geophys. Res.*, 113:A12, 2008. 30

R. C. Willson and H. S. Hudson. Solar luminosity variations in solar cycle 21. *Nature*, 332:810–812, 1988. 9

L. Woltjer. A Theorem on Force-Free Magnetic Fields. *Proceedings of the National Academy of Sciences of the United States of America*, 44:489–491, 1958. 30